INTERNATIONAL SCIENCE CONFERENCE

अंतर्राष्ट्रीय विज्ञान सम्मेलन

विज्ञान शिक्षा अभ्यास

SCIENCE EDUCATION PRACTICE

दिल्ली, भारत 2023 / Delhi, India 2023

International Science Conference

SCIENCE EDUCATION PRACTICE

Part 2

April 8, 2023. Delhi, India

Proceedings of the International Science Conference **“SCIENCE. EDUCATION. PRACTICE”** (April 8, 2023). Part 2. Delhi. India.

ISBN 978-5-905695-89-6

Science Conference Proceedings combine materials of the conference – research papers and thesis reports of scientific workers. They examine technical, juridical and sociological aspects of research issues. Some articles deal with theoretical and methodological approaches and principles of research questions of personality professionalization.

Authors are responsible for the accuracy of cited publications, facts, figures, quotations, statistics, proper names and other information.

ISBN 978-5-905695-89-6

CONTENTS

CHEMICAL SCIENCES

TECHNICAL SCIENCES

DOI 10.34660/INF.2023.76.88.051

CIRCADIAN RHYTHM OF TOTAL PERIPHERAL VASCULAR RESISTANCE IN THE PHASE OF ANURIA IN INFANTS

Muhitdinova Hura Nuritdinovna
Doctor of Medical Sciences, Full Professor
Center for the Development of Professional Qualifications of Medical Workers

Alimov Davron Anvarovich
Doctor of Medical Sciences, Full Professor, Deputy Scientific Director
Republican Scientific Center for Emergency Medical Care

Babajanova Zumrat Omarovna
Candidate of Medical Sciences, Head of Department
Republican Scientific Center for Emergency Medical Care

Abstract. *Based on the study of the data of hourly monitoring of total peripheral vascular resistance (TPVR) in 33 children with ARF, the revealed increase in TPVR by more than two times with a hyperdynamic type of hemodynamics remained increased during intensive care, hemodialysis in all patients. A significant direct correlation of TPVR and DBP was observed only in patients of the 1st group. The most prolonged inversion of the circadian rhythm of the TPVR was detected in the 2nd group (16 days out of 30), somewhat less long in the children of the 3rd group (12).*

Keywords: *circadian rhythm, total peripheral vascular resistance, anuria, children.*

Relevance. Interorgan structural and functional connections between the kidneys and other systems, such as the cardiovascular system, are more pronounced in childhood due to limited reserve capabilities, which is especially pronounced in pathological conditions. At present, it is not enough to study individual parameters of kidney function in patients with uronephrological pathology. It is advisable to use an integrated approach with the use of methods to create an idea about the work of the heart in these patients, deviations of its parameters from the norm, and most importantly, to identify the presence of combined defects in the kidneys and heart, which is not a rare occurrence. Total vascular resistance is the sum specific resistance, which the blood has overcome, having reached a given section

of the cardiovascular system. In places of branching and bending of the arteries and arterioles, the laminar nature of the blood flow is disturbed and becomes turbulent (vortex). The eddies that form perpendicular to the blood flow significantly increase the internal friction of the blood, and much more pressure is required to move it. In the capillaries, the nature of the blood flow becomes chain-like, since their diameter is equal to or even somewhat smaller than the diameter of erythrocytes. Erythrocytes move one after another one by one in a chain, deforming in accordance with the size of the capillary. The TPVR parameter has a rhythm. As noted in the literature, TPVR in the daytime was found to be lower compared to morning values, and the capillaries were maximally dilated at 18:00. In the work of the authors, lower values of TPVR were recorded during the year at 2-4 pm compared to the morning ones, which coincides with the above-mentioned literature data [1-4]. Due to the lack of data on changes in TPVR during the period of anuria in children under 3 years, we tried by prolonged monitoring to identify the features of changes in the indicator in acute renal failure.

Goal of the work. To study and evaluate changes in the circadian rhythm of the total peripheral vascular resistance in the phase of anuria in infants.

Material and research methods. The data of hourly monitoring of total peripheral vascular resistance (TPVR) in 33 children with ARF admitted to the ICU of RSCEMC with anuria from 1 to 5 days at the age of 10 months to 3 years 4 months from the ICU of regional children's hospitals and branches of RSCEMC was studied. Prior to admission to the clinic, all patients received anti-inflammatory therapy aimed at the treatment of ARI-2, pneumonia 25, glomerulonephritis - 4, AII-3 patients. According to the indications, due to severe progressive respiratory failure, patients were provided with invasive mechanical respiratory support from the first day. All patients underwent hemodialysis, 4 patients underwent hemodialysis in combination with plasmapheresis under the control of hemodynamics, acid-base status (ABS), respiratory system, maintenance, antibacterial, anti-inflammatory, syndromic corrective intensive therapy according to the recommendations in the literature. A favorable outcome with the restoration of full functional activity of the kidneys and discharge from the hospital was observed in 23 children (groups 1 and 2), an unfavorable outcome in 10 children (group 3). The first group consisted of patients who received intensive care in the ICU for up to 10 days (10), the second - children (13) with a favorable outcome after intensive care for 11-90 days.

As shown in Table 1, the duration of intensive care in children of groups 2 and 3 significantly exceeded the duration of treatment in the ICU in group 1 by 20 or more days ($p<0.05$, respectively). In group 2, the duration of mechanical respiratory support (MRS) was 18.6 ± 8 days, in group 3, a longer MRS did not improve the outcome of the disease. The following formula for calculating TPVR

was used: TPVR=SBP*5/MOV*10, dyn.s.cm^{-5}m, where SBP is systolic blood pressure, MVB is the minute volume of blood circulation.

Table 1.

Characteristics of patients

Groups	Age, month.	Start of IVL, days	Duration of MCI, days	In ICU, days
1	29±2,8	0	0	7,8±1,5
2	19±7,7	4,3±3,5	18,6±7,6	27,8±4,3*
3	30,5±6,5	5,5±0,5	25,5±6,7	30,7±6,8*

* - the difference is significant relative to the indicator in group 1.

Results and its discussion.

As shown in Tables 2 and 3, upon admission, all children showed a significant increase in TPVR (more than 2 times), which, against the background of intensive care, hemodialysis, remained steadily elevated without significant changes in the mesor and TPVR on average over the period of observation of the circadian rhythm.

Table 2.

Dynamics of the mesor of the circadian rhythm TPVR

Days	1 group	2 group	3 group
1	2128±193	2606±697	2663±479
2	2246±119	2027±162	1944±134
3	2613±171	2284±204	2072±148
4	2617±203	2190±128	1921±87
5	2751±122	2190±145	1945±129
6	2557±174	2223±152	1843±202
7	2485±176	2507±116	1784±161
8	2350±136	2189±187	1867±163
9	2495±406	2481±234	2148±145
10	2293±262	2272±185	2179±182
11		2083±167	2150±172
12		2082±160	1944±135
13		2066±133	1987±165
14		2485±274	2050±189
15		2220±261	1904±135
16		2145±164	1691±173
17		2278±142	1860±248
18		2389±141	1924±213
19		2309±167	2010±205

20		2163±201	1715±140
21		2249±194	1893±218
22		2237±151	1921±200
23		2449±233	1766±183
24		1903±274	1900±323
25		1771±200	1863±143
26		1951±179	2122±188
27		2381±398	2248±216
28		2228±304	2108±252
29		1569±172	2105±192
30		1703±306	1940±217

Table 3.

Average circadian rhythm of OPSS in the phase of anuria of acute renal failure dyn.s.cm^{-5}m

Hours	1 group	2 group	3 group
8	2406±217	2451±264	2068±214
9	2426±163	2383±300	1995±229
10	2444±232	2261±310	1962±233
11	2352±206	2226±369	1949±283
12	2510±306	2243±286	1974±306
13	2554±215	2108±176	2031±228
14	2583±236	2134±225	2142±276
15	2406±231	2108±259	2083±314
16	2416±298	2113±239	1986±189
17	2446±337	2161±255	2029±261
18	2374±243	2248±252	1947±188
19	2446±220	2209±268	1974±213
20	2359±223	2257±267	1950±217
21	2365±271	2233±329	1983±185
22	2630±429	2212±293	2012±206
23	2588±266	2122±209	2019±250
24	2720±233	2118±199	1900±182
1	2600±221	2155±273	1947±237
2	2467±153	2142±211	1916±185
3	2446±170	2141±246	1941±207
4	2406±175	2107±262	1971±216
5	2419±238	2126±241	1886±179
6	2299±282	2098±301	1913±176
7	2345±316	2148±307	1907±203

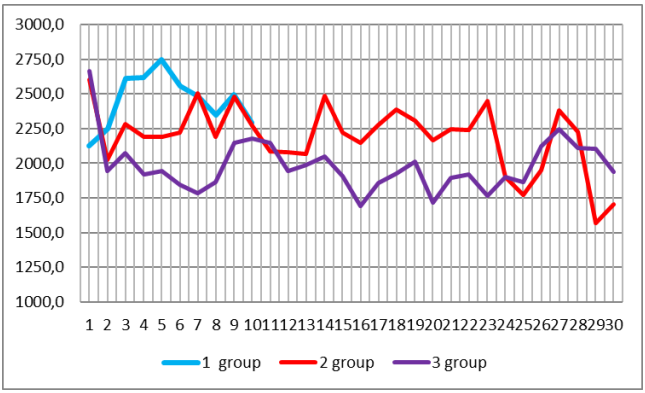

Figure 1. *Dynamics of the mesor of the circadian rhythm of TPVR in acute renal failure up to 3 years, dyn.s.cm^{-5}m*

Attention was drawn to the trend of a relatively higher average daily level of TPVR in groups 1 and 2 relative to changes in the indicator in group 3 (Fig. 1), although in general the mesor of the circadian rhythm of peripheral resistance in the most severe patients was significantly increased (Fig. 2). The changes were of an oscillatory nature with an amplitude of fluctuations in group 1 of 200-600 dyn.s.cm^{-5}m (Fig. 3). The most pronounced fluctuations in the amplitude of the circadian rhythm of the TPVR were observed in group 2 on days 1, 14.27.

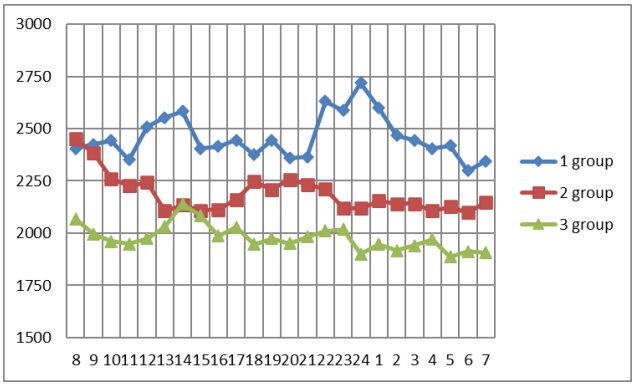

Figure 2. *Circadian rhythm of TPVR up to 3 years, dyn.s.cm^{-5}m*

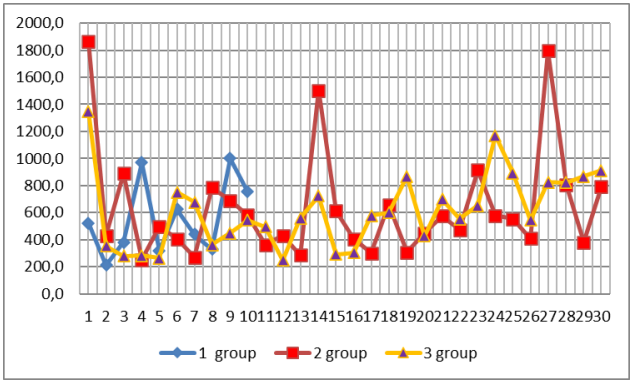

Figure 3. *Amplitude of diurnal changes of TPVR, dyn.s.cm*$^{-5}$*m*

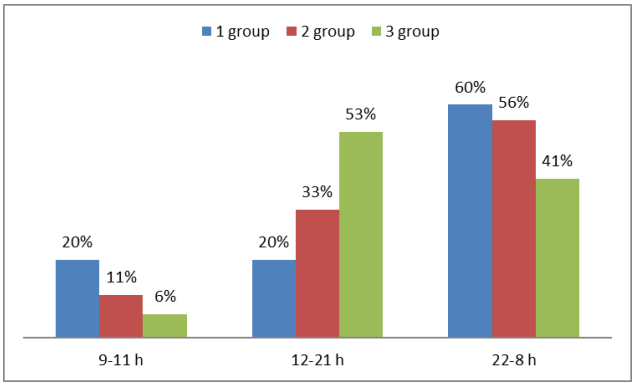

Figure 4. *Duration of acrophase shift in % relative to the duration of intensive care in the ICU*

The longest inversion of the circadian rhythm was found in the 2nd group (16 days), somewhat shorter (12) in the children of the 3rd group. Although, in percentage terms, the longest shift in the peak of the acrophase of the circadian rhythm of the TPVR was observed in group 1, which suggests a more active participation of the circadian rhythm of the TPVR in the process of adaptation in conditions of acute renal failure in children of the 1st group (Fig. 4). The latter can be explained by a relatively less pronounced radical external influence, such as prosthetic external respiration in groups 2 and 3 due to more pronounced disorders, progression of acute respiratory failure.

The tendency to increase TPVR at night characterizes an increase in the load on the heart muscle, which, in conditions of secondary myocarditis, the adverse

effect of general intoxication on the myocardium, further increases the risk of developing acute heart failure. In this regard, it may be necessary to enhance the vasodilatory effect of drug correction in the dark.

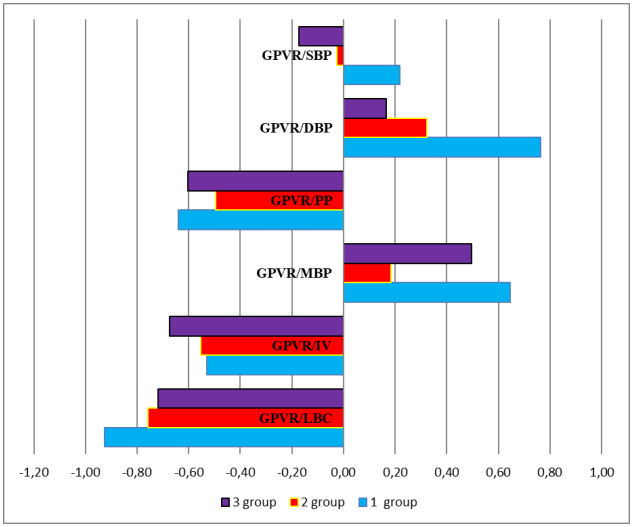

Figure 5. *Correlations of TPVR with hemodynamic parameters*

The found strong inverse correlation of changes in TPVR and IOC characterizes the hyperdynamic type of hemodynamics in all patients. So, in the 1st group, the correlation between TPVR and the MVB was (-0.93), in the 2nd - (-0.76), in the 3rd group - (-0.72). A less pronounced negative correlation of TPVR and SV of the same direction corresponded to the hyperdynamic nature of the restructuring of the function of the cardiovascular system, indicating participation in the compensatory mechanism and an increase in stroke volume. An increase in TPVR corresponded to a decrease in PAP, confirmed by a negative correlation in group 1 (-0.64), in group 2 - (-0.49), in group 3 (-0.6). Reliably significant direct correlation of TPVR and DBP was observed only in patients of group 1 (0.76). The decrease in the correlation between TPVR and DBP was facilitated not only by a more severe general condition, but also by the need to use medications during mechanical ventilation that have a vasodilating effect (hypnotics, relaxants).

Conclusion. Initially increased TPVR by more than two times with the hyperdynamic type of hemodynamics remained elevated during intensive care, hemodialysis in all patients. Reliably significant direct correlation of TPVR and DBP was observed only in patients of group 1. out of 30), somewhat less long in children of the 3rd group (12).

References

1. *https://docs.yandex.ru/docs/view?tm=1679486556&tld=ru&lang=ru&name=farmakfit.pdf&text=%D0%*
2. *https://www.rmj.ru/articles/urologiya/OSTRAYa_POChEChNAYa_NEDOSTATOChNOSTY_1/*
3. *https://cyberleninka.ru/article/n/dinamika-obschego-perifericheskogo-soprotivleniya-sosudov-v-techenie-goda-u-zhenschi-1*
4. *https://cyberleninka.ru/article/n/sostoyanie-serdechno-sosudistoy-sistemy-pri-uronefrologicheskih-zabolevaniyah-u-detey*

DOI 10.34660/INF.2023.21.20.052

CIRCADIAN RHYTHM OF CARDIAC OUTPUT DURING ANURIA IN ACUTE RENAL FAILURE IN INFANTS

Muhitdinova Hura Nuritdinovna
Doctor of Medical Sciences, Full Professor
Center for the Development of Professional Qualifications of Medical Workers

Tulaganov Davron Bahtiyarovich
Doctor of Medical Sciences, Full Professor, Director
Republican Scientific Center for Emergency Medical Care

Turgunova Dilorom Pulatovna
Assistant of Department
Center for the Development of Professional Qualifications of Medical Workers

Keywords: *circadian rhythm of minute volume of blood circulation, anuria, renal failure, infants.*

Relevance. The most common causes of prerenal acute renal failure (ARF) in children are dehydration against the background of acute gastroenteritis, accompanied by loss of fluid through the gastrointestinal tract (vomiting, diarrhea), exogenous (poisoning) and endogenous (sepsis) intoxications, and the so-called "losses in the third space" (with burns, nephrotic syndrome, liver disease). Causes of renal acute renal failure in children include diseases of the renal parenchyma (glomerulonephritis, autoimmune and vascular damage to the renal tissue), exposure to drugs (antibiotics and others) and nephrotoxins. Serious consequences of oliguria / anuria are pulmonary edema and brain, hypervolemia (volume overload), hyperkalemia, acidosis, drug toxicity. The goal of intensive therapy for acute renal failure is the prevention of these potentially fatal complications and renal ischemia: hemodynamic optimization, maintenance of mean blood pressure at the level of 80-100 mm Hg, active treatment of hypoxia, provision of zero or even negative balance to prevent pulmonary edema in anuria, monitoring of electrolyte composition blood, acid-base balance (ABB). The authors consider it unacceptable to add potassium to infusion solutions and the use of drugs that can increase potassium levels (angiotensin-converting enzyme inhibitors (ACE inhibitors)). The

inadmissibility of the use of nephrotoxic drugs (aminoglycosides, non-steroidal anti-inflammatory drugs (NSAIDs), ACE inhibitors), control of doses of drugs that depend on renal excretion (digoxin, antibiotics: vancomycin and amikacin). Osmodiuretics (mannitol, 10-20-40% glucose solution, 7.5-10% sodium chloride solution), afferent arteriole dilators (dopamine at doses of 1-2 mcg / kg / min, eufillin 8-10 mg / kg per day), and then loop diuretics (furosemide), application which should be administered as a bolus of 3 mg/kg followed by a metered infusion at a rate of 0.5 mg/kg/h. The absence of a pronounced diuretic effect from the therapy, a decrease in the glomerular filtration rate, as well as an increase in creatinine or urea during the day by more than 1.5 times are indications for renal replacement therapy. Early initiation of extracorporeal detoxification helps prevent the development of multiple organ failure. Dialysis is characterized by a negative nitrogen balance; therefore, patients on hemodialysis require an increased protein content in food (1.5 mg / kg / day). Renal replacement therapy (RRT) is a complex of heterogeneous in structure and the fundamental principles of the procedures carried out to maintain the life of a patient with lost functions of their own kidneys. Methods of renal replacement therapy (MRRT) are divided into extracorporeal - hemodialysis (HD), hemofiltration (HF), hemodiafiltration (HDF), peritoneal dialysis (PD) and kidney transplantation. A perfusionist who provides hemodialysis in a child first of all faces the problem of hemohydrobalance disturbance and its correction. Numerous studies have confirmed the concept that antihypertensive therapy slows down the rate of progression of CKD [1-4]. However, there is not enough data on changes in the MBVduring anuria in young children, which served as the basis for this study.

Goal of the work. To study the features of the circadian rhythm of the minute volume of blood in children with acute renal failure in the period of anuria at an early age.

Material and research methods. The data of hourly monitoring of the minute volume of blood (MBV) in 33 children with acute renal failure admitted to the ICU of RSCEMC with anuria from 1 to 5 days at the age of 10 months to 3 years 4 months from the ICU of regional children's hospitals and branches of RSCEMC was studied. Prior to admission to the clinic, all patients received anti-inflammatory therapy aimed at the treatment of ARI-2, pneumonia 25, glomerulonephritis - 4, AII-3 patients. According to the indications, due to severe progressive respiratory failure, patients were provided with invasive mechanical respiratory support from the first day. All patients underwent hemodialysis, 4 patients underwent hemodialysis in combination with plasmapheresis under the control of hemodynamics, acid-base status (ABS), respiratory system, maintenance, antibacterial, anti-inflammatory, syndromic corrective intensive therapy according to the recommendations in the literature. A favorable outcome with the restoration of full functional activity of the kidneys and discharge from the hospital was observed in 23

children (groups 1 and 2), an unfavorable outcome in 10 children (group 3). The first group consisted of patients who received intensive care in the ICU for up to 10 days (10), the second - children (13) with a favorable outcome after intensive care for 11-65 days.

As shown in Table 1, the duration of intensive care in children of groups 2 and 3 significantly exceeded the duration of treatment in the ICU in group 1 by 20 or more days ($p<0.05$, respectively). In group 2, the duration of mechanical respiratory support (MRS) was 18.6 ± 8 days, in group 3, a longer MRS, unfortunately, did not improve the outcome of the disease.

Table 1.

Characteristics of patients

Groups	Age, month.	Start of IVL, days	Duration of MCI, days	In ICU, days
1	29±2,8	0	0	7,8±1,5
2	19±7,7	4,3±3,5	18,6±7,6	27,8±4,3*
3	30,5±6,5	5,5±0,5	25,5±6,7	30,7±6,8*

* - the difference is significant relative to the indicator in group 1.

Results and discussion. In groups 1 and 2, the indicators of the mesor of the circadian rhythm of the MBVdid not differ significantly from the age norm, only in the 3rd group, from the first day, a statistically unreliable, but clinically significant trend was revealed to increase the mesor of the circadian rhythm of the MBV by 200-600 ml relative to the indicator in groups 1 and 2 (Table 2).

Table 2.

Dynamics of the mesor of the circadian rhythm MBV (l/min)

Days	1 group	2 group	3 group
1	2,8±0,3	2,4±0,5	3,0±1,3
2	2,7±0,1	3,1±0,2	3,9±2,7
3	2,3±0,1	2,8±0,2	3,5±2,7
4	2,5±0,2	2,9±0,1	4,0±2,8
5	2,4±0,1	3,0±0,2	4,0±2,9
6	2,5±0,2	2,9±0,2	4,8±2,9
7	2,5±0,2	2,7±0,1	4,4±2,8
8	2,7±0,2	2,9±0,2	4,0±2,9
9	2,5±0,3	2,8±0,2	4,1±2,7
10	2,8±0,3	2,8±0,2	3,7±2,4
11		3,0±0,2	3,6±2,5
12		3,1±0,2	4,4±2,9
13		3,0±0,1	3,6±2,4

14		2,6±0,2	3,7±2,5
15		2,7±0,2	3,4±2,7
16		2,9±0,2	4,2±2,9
17		2,6±0,2	4,2±2,6
18		2,6±0,1	3,9±2,7
19		2,7±0,2	3,7±2,0
20		2,8±0,3	4,4±2,8
21		2,8±0,2	4,1±2,3
22		2,8±0,2	4,4±2,2
23		2,7±0,2	4,1±2,5
24		3,3±0,5	4,3±2,4
25		3,7±0,3	4,1±2,4
26		3,1±0,2	3,4±2,3
27		3,2±0,2	3,6±2,4
28		2,6±0,3	4,0±2,6
29		3,0±0,5	3,8±2,5
30		3,6±0,8	4,4±2,7

Table 3.

Average values of the MBV in the circadian rhythm (l / min)

Hours	**1 group**	**2 group**	**3 group**
8	2,6±0,2	2,6±0,2	3,1±0,3
9	2,6±0,2	2,7±0,3	3,2±0,4
10	2,5±0,2	2,9±0,3	3,2±0,3
11	2,6±0,3	2,9±0,4	3,3±0,4
12	2,5±0,2	2,9±0,4	3,3±0,4*
13	2,5±0,2	3,0±0,2	3,2±0,3*
14	2,5±0,2	3,0±0,3	3,2±0,4*
15	2,6±0,2	3,0±0,3	3,2±0,4*
16	2,6±0,2	3,0±0,3	3,2±0,3*
17	2,6±0,3	2,9±0,3	3,1±0,4
18	2,6±0,2	2,9±0,3	3,2±0,3*
19	2,7±0,2	2,9±0,2	3,2±0,3
20	2,7±0,3	2,8±0,2	3,2±0,3
21	2,6±0,3	2,9±0,3	3,2±0,3
22	2,5±0,4	3,0±0,4	3,1±0,4
23	2,4±0,2	3,0±0,3	3,1±0,3*
24	2,4±0,2	2,9±0,3	3,4±0,4*
1	2,5±0,2	2,9±0,3	3,3±0,4*
2	2,5±0,1	2,9±0,3	3,3±0,3*

3	2,6±0,2	3,0±0,4	3,3±0,4*
4	2,6±0,2	3,0±0,3	3,3±0,4*
5	2,6±0,2	2,8±0,3	3,3±0,4*
6	2,7±0,3	2,9±0,3	3,3±0,3
7	2,7±0,3	2,9±0,4	3,3±0,3

*-significantly relative to the indicator of group 1

Analysis of the average values of the MBV in the circadian rhythm in the phase of anuria of acute renal failure (tab. 3) up to 3 years made it possible to state a significant significantly significant increase in the MBV in the daytime (from 11 to 18 hours) by 32% -24%, and at night (from 23 hours to 5 hours) by 28%-32% ($p < 0.05$, respectively). The revealed increase in the MBV both in the daytime and at night was evidence of an unfavorable change in hemodynamics in children of the 3rd group, even in the absence of significant differences in the circadian mesor the rhythm of the studied indicator from the indicators of patients with a favorable outcome (Fig. 1,2).

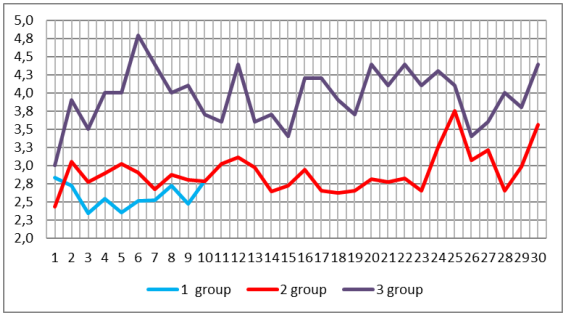

Figure 1. *Dynamics of the mesor of the circadian rhythm of the MBV in l / min.*

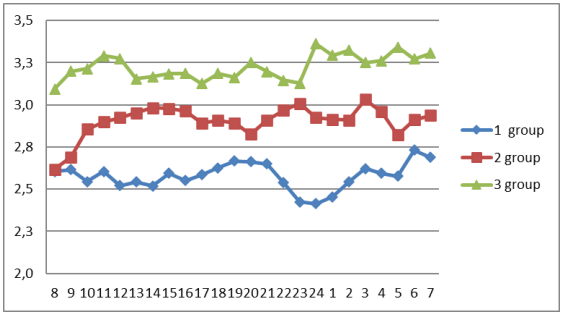

Figure 2. *The average values of the MBVin the circadian rhythm in the phase of anuria of ARF up to 3 years*

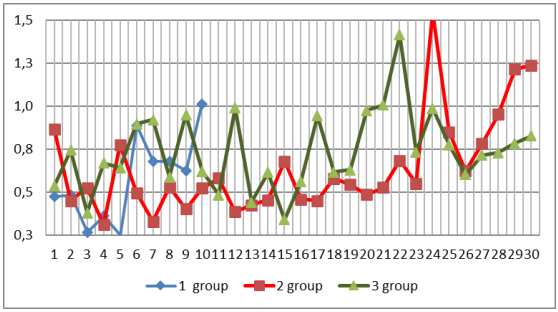

Figure 3. *Dynamics of the amplitude of the circadian rhythm MBV, l/min*

Attention is drawn to the oscillatory nature of the change in the amplitude of the daily rhythm of the MBV. The trend towards an increase in the amplitude of the circadian rhythm of the MBV in group 1 on days 6-10 was due to an increase in the volume of infusion therapy as the excretory function of the kidneys was restored (Fig. 3). In the 2nd group of children, the amplitude of daily fluctuations in the MBVup to 23 days was no more than 200 ml, an increase in the indicator by 24.28 days was explained by the transfer of children to spontaneous breathing as reflexes, adequate breathing, and consciousness were restored, which, as a rule, was accompanied by a compensatory reaction of the heart of the vascular system, primarily of an adaptive nature under conditions of restoration of adequate spontaneous breathing in the process of effective treatment of pneumonia at an early age (Fig. 3). the development of decompensation of the function of other organs, including acute heart failure, impaired regulatory function of the central nervous system in acute cerebral insufficiency (Fig. 3).

The longest inversion of the circadian rhythm of the MBV was found in children of the 2nd group (12 days), in the 3rd group, the shift of the acrophase of the circadian rhythm of the MBV to the night hours lasted 10 days (Fig. 4). That is, a violation of the circadian rhythm of the MBV in the form of a shift in the peak of the acrophase to the dark time of the day fully corresponded to the severity of the disease, which leads to the advisability of more careful monitoring of the circulatory system at night due to an increased risk of developing acute cardiac decompensation in more severe children of groups 2 and 3, more intensive pathogenetically substantiated syndromic correction.

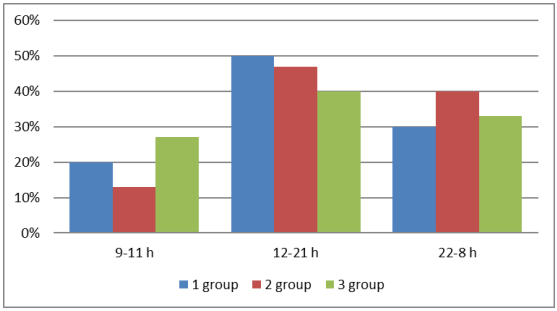

Figure 4. *Duration and severity of the shift of the acrophase of the circus rhythm of the MBV*

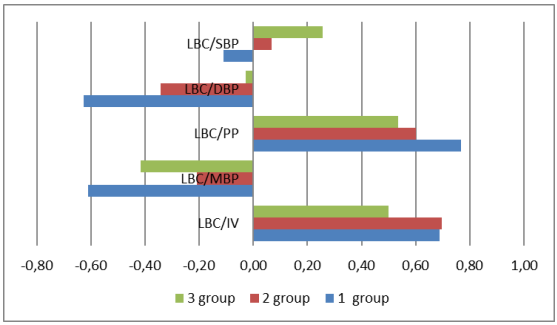

Figure 5. *MBV correlations*

A direct strong correlation was found between changes in the MBVwith SV (0.69; 0.7) and PBP (0.77; 0.6) in groups 1 and 2, which weakened in group 3 (0.5; 0.54, respectively).). The negative correlation dependence of the mean BP on the MBV (-0.61) and between the MBV and DBP (-0.63) in group 1 reflected, compared with other groups, a more pronounced compensatory involvement of peripheral vascular tone with changes in the MBV.

Conclusion. In the group with an unfavorable outcome, from the first day, a statistically insignificant, but clinically significant trend towards an increase in the mesor of the circadian rhythm of the MBV was revealed, as well as a significant increase in the MBV both in the daytime and at night relative to the indicator in groups 1 and 2. In group 1, compared with other groups, a more pronounced compensatory participation in the process of adapting the tone of peripheral vessels with a change in the MBV was revealed.

References

1. *https://safra.hospital-direct.org.il/news-acute-renal-failure.aspx*
2. *https://cyberleninka.ru/article/n/ostraya-pochechnaya-nedostatochnost-1*
3. *https://cyberleninka.ru/article/n/klinicheskie-effekty-primenenie-modifitsirovannoy-ultrafiltratsii-krovi-u-detey-rannego-vozrasta*
4. *https://diseases.medelement.com/disease/%D0%B3%D0%B5*

DOI 10.34660/INF.2023.98.37.053

WIDESPREAD OSTEONECROSIS OF THE UPPER JAW AFTER CORONAVIRUS INFECTION

Bairikov Ivan Mikhailovich
Corresponding Member of the Russian Academy of Sciences, Doctor of Medical Sciences, Professor
Federal State Budgetary Educational Institution of Higher Education "Samara State Medical University" of the Ministry of Health of the Russian Federation

Samutkina Marina Gennadevna
Department of Maxillofacial Surgery and Dentistry, Federal State Budgetary Educational Institution of Higher Education "Samara State Medical University" of the Ministry of Health of the Russian Federation, Samara, Russian Federation

Yuldasheva Nargiza Timurovna
Department of Maxillofacial Surgery and Dentistry, Federal State Budgetary Educational Institution of Higher Education "Samara State Medical University" of the Ministry of Health of the Russian Federation, Samara, Russian Federation

Vasilyev Yuriy Leonidovich
Department of Operative Surgery and Topographic Anatomy, Federal State Autonomous Educational Institution of Higher Education First Moscow State Medical University named after I.M. Sechenov Ministry of Health of the Russian Federation, Moscow, Russian Federation

Fatenkov Oleg Veniaminovich
Department of Faculty Therapy, Federal State Budgetary Educational Institution of Higher Education "Samara State Medical University" of the Ministry of Health of the Russian Federation, Samara, Russian Federation

Abstract. *The pandemic caused by the new coronavirus SARS-CoV-2 is another challenge for humanity. The efforts of scientists and doctors around the world are aimed at studying the features of the epidemiology, pathogenesis, clinic and treatment of the coronavirus infection COVID-2019. Direct interaction of the*

causative agent of a new coronavirus infection with ACE-2 receptors, which are present both in the alveoli of the lungs, the myocardium, and in the endothelium of blood vessels, leads to damage to the vascular wall, stimulates response thrombus formation. One of the important mechanisms in the pathogenesis of osteonecrosis, including that of the jaw bones, in the occurrence of bone necrosis is a violation of blood circulation, as well as a deterioration in the rheological properties of blood and a slowdown in the rate of volumetric blood flow, which can be the cause of intravascular coagulation. These two factors are the main cause of bone necrosis with the release of inflammatory mediators. Therefore, it can be assumed that damage to the vascular wall and impaired microcirculation in a new coronavirus infection may contribute to the development of a destructive form of osteonecrosis of the jaw bones.

We report a case of diffuse destructive osteonecrosis of the maxilla in a 67-year-old female patient suffering from hypertension and type 2 diabetes mellitus after bilateral pneumonia associated with a new coronavirus infection.

During the first hospitalization, surgical intervention consisted in the removal of teeth 2.4, 2.5, 2.6, a freely located bone sequester of the alveolar process within the boundaries of teeth 2.4, 2.5, periostectomy within the boundaries of teeth 2.2, 2.3, 2.4, 2.5. There was no bleeding from the sockets of the teeth, the visible bone of the alveolar process was white, bloodless, "naked".

When examined 2 months after the operation, in the oral cavity - exposure of the bone of the alveolar process within the boundaries of 2.1 - 2.6 teeth, when probing from the side of the palate - a pathological pocket extending in the direction of the soft palate to a depth of more than 2.0 cm. Bone sequestration within the boundaries of the alveolar the process containing the sockets of the removed teeth is mobile. A surgical intervention was performed - sequestrectomy, during which a defect was formed that communicates the oral cavity with the nasal cavity on the left and the maxillary sinus. The defect is closed by a protective plate that separates the cavity of the mouth, nose and maxillary sinus.

Key words: *new coronavirus infection, maxillary osteonecrosis, osteonecrosis, sequestrectomy.*

Introduction

On December 31, 2019, the Center of the World Health Organization (WHO) in China officially announced the registration of pneumonia of unknown etiology in the city of Wuhan (Hubei Province). All the first sick patients were somehow connected with the local Huanan animal and seafood market [6]. On January 7, 2020, scientists from the Shanghai Clinical Center for Public Health and the School of Public Health established the complete genomic sequence of the causative agent of this pneumonia [4], on February 11, 2020, a new coronavirus in-

fection was named COVID-2019, and the virus that causes it was renamed SARS -CoV-2 (Severe acute respiratory syndrome coronavirus 2) [3].

The new SARS-CoV-2 coronavirus is a single-stranded RNA-containing virus of the Coronaviridae family, Beta-CoV B line. It is assigned to pathogenicity group II, like some other members of this family (SARS-CoV virus, MERS-CoV) and, presumably, is a recombinant virus between a bat coronavirus and a coronavirus of unknown origin. The genetic sequence of SARS-CoV-2 is at least 79% similar to that of SARS-CoV [2].

According to the literature, the infectious process is realized mainly by airborne and contact-household transmission of the pathogen, which contributes to the pandemic spread of SARS-CoV-2.

To date, Hoffmann et al. and Walls et al. provided compelling evidence that SARS-CoV-2 accesses body cells via angiotensin-converting enzyme 2 (ACE-2) receptors in the same way that SARS-Cov did earlier. The genes responsible for the expression of ACE-2 localized on the X chromosome have been identified. ACE2 receptors are found in the heart (endothelium of the coronary arteries, myocytes, fibroblasts, epicardial adipocytes), vessels (endothelial and vascular smooth cells), intestine (epithelial cells of the intestine), lungs (epithelial cells of the trachea and bronchi, type 2, pneumocytes, macrophages), kidneys (luminal surface of tubular epithelial cells), testicles, brain. The vulnerability of the lungs due to viral infection can be explained by the large surface area of alveolar epithelial cells. At the same time, ACE-2 receptors are mainly associated with cell membranes and are almost not present in the bloodstream in a soluble form [8].

The incubation period for a new coronavirus infection ranges from 2 to 14 days, on average 5-7 days. Among the first symptoms of COVID-19, as the frequency of occurrence decreases, an increase in body temperature, a cough - dry or with a small amount of sputum, shortness of breath, myalgia and fatigue, a feeling of tightness in the chest, as well as headaches, hemoptysis, diarrhea and nausea. These symptoms at the onset of infection can also be observed in the absence of an increase in body temperature [7].

Clinical forms of COVID-19: asymptomatic (1-3%); mild (affecting only the upper respiratory tract); moderate (pneumonia without respiratory failure); severe (pneumonia with the development of respiratory failure); very severe (critical) form (pneumonia, sepsis, septic shock, multiple organ failure). Neurological symptoms of varying severity are observed in 36% of patients [1].

Mortality in COVID-2019 is proportional to the age of patients: from 0% in children under 9 years old to 14.8% in people over 80 years old [9].

Direct interaction of the causative agent of a new coronavirus infection with ACE-2 receptors, which are present both in the myocardium and in the endothelium of blood vessels, leads to damage to the vascular wall, stimulates response thrombus formation with subsequent deposition of cholesterol and a decrease in

the diameter of the lumen up to critical obstruction, which, according to studies, leads to myocardial damage in many patients with COVID-19 [10].

One of the important mechanisms in the pathogenesis of osteonecrosis, including jaw bones, in the occurrence of bone necrosis is circulatory disorders. The accumulation of inflammatory exudate in the bone leads to an increase in intraosseous pressure (M. V. Grinev, 1977), a violation of microcirculation. This is also facilitated by the deterioration of the rheological properties of the blood and the slowing down of the rate of volumetric blood flow, which can be the cause of intravascular blood coagulation. These two factors are the main cause of bone necrosis with the release of inflammatory mediators [11]. In the upper jaw, peripheral sequesters are predominantly formed, in contrast to osteonecrosis of the bone caused by desomorphine or treatment with bisphosphonates, in particular, zolidronic acid [5]. Therefore, it can be assumed that damage to the vascular wall and impaired microcirculation in a new coronavirus infection may contribute to the development of a destructive form of odontogenic osteonecrosis of the jaw bones.

Own observations

In the period from 12/12/2020 to 12/28/2020, patient M., born in 1953, was treated at the Department of Maxillofacial Surgery at clinics of Samara State University. Upon admission, she complained of nasal congestion, swelling of the face on the left. From the anamnesis, it was revealed that after suffering COVID-19, at the end of October, nasal congestion appeared, swelling on the face on the left. At the end of November, her condition worsened, she was hospitalized to the ENT department of City Hospital No. 8. Then she was transferred to the therapeutic department of hospital No. 8 due to anemia. After the discharging from the hospital, she turned to the dentist at the place of residence, taking into account the defeat of the maxillary sinuses, the presence of 2.4, 2.5, 2.6 teeth with foci of chronic infection in the periodontal area, spontaneous dislocation of the tooth 2.1, tooth mobility 2.2, 2.3, 2.4, 2.5, 2.6, consultation and treatment was recommended at the department of maxillofacial surgery.

When examined by a maxillofacial surgeon, asymmetry of the face was noted due to a slight swelling of the soft tissues of the infraorbital, buccal regions on the left, the skin integuments of a physiological color, without infiltration, are collected in a fold. Nasal breathing is difficult on the left, in the left nasal passage there are purulent crusts. Palpation of the anterior wall of the maxillary sinus on the left is moderately painful. Full opening of the mouth, painless. There was a classic "muft-like" infiltrate in the region of the alveolar process of the upper jaw on the left, smoothness and pain on palpation of the transitional fold in the boundaries of 2.2 - 2.6 teeth. Tooth 2.4 is cariously destroyed, 2.6 is restored with a filling, 2.2, 2.3, 2.5 are intact. During percussion, she noted soreness of 2.2 - 2.6 teeth, mobility of 2-3 degrees.

Clinical and radiological examinations were conducted. In the general (clinical) blood test - changes characteristic of the inflammatory process, the level of

CRP - 36.35 mg / l; biochemical blood test, coagulogram at admission - within the reference limits of the norm. According to X-ray data of the bones of the facial skull, the anterior wall of the left maxillary sinus extending to the lateral wall, zygomatic bone, and lateral wall of the orbit are represented by modified bone fragments with reduced density. In both maxillary sinuses, frontal sinuses, cells of the ethmoid labyrinth - thickening of the mucous membrane. The diagnosis was made: Chronic osteonecrosis of the upper jaw on the left in the acute stage. Chronic pansinusitis.

Surgical intervention consisted in the removal of teeth 2.4,2.5,2.6, a freely located bone sequester of the alveolar process within the boundaries of teeth 2.4,2.5, periostotomy within the boundaries of 2.2, 2.3, 2.4, 2.5 teeth. No pus was obtained from the sockets of the extracted teeth during periostectomy. The wound contained loose granulation tissue, which was sent for histological examination. An abscess was opened on the hard palate. Traces of pus were received, 2 drainage were installed, hemostasis was performed. There was no bleeding from the sockets of the teeth, the visible bone of the alveolar process was white, bloodless, “naked”.

Conducted traditional complex drug treatment, physiotherapy, 5 sessions of hyperbaric oxygen therapy. On the 3rd day after the intervention, there were symptoms of perforation of the maxillary sinus on the left, during the examination a communication with the maxillary sinus in the area of the extracted tooth 2.6 was found as a result of rejection of the interradicular septum. The patient was discharged with improvement on the 14th day after the operation.

After discharge from the hospital, outpatient monitoring of the patient continued for 1.5 months. During this time, the patient had an abscess of the lower eyelid, spontaneous extraction of teeth 2.2, 2.3, rejection of small bone sequesters, scanty purulent discharge from the wound in the oral cavity remained, as well as growth of granulations without a tendency to epithelialization and exposure of sequestering bone areas (Fig. 1.).

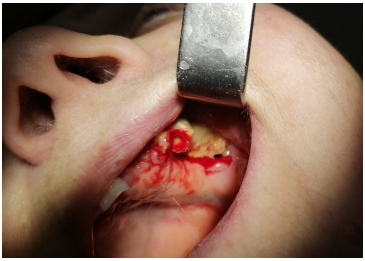

Figure 1. *The view of the oral cavity of patient M. Forming sequester in the region of the alveolar process of the upper jaw on the left 1 month after the operation of tooth extraction, periostectomy.*

When examined 2 months after the operation, moderate asymmetry of the face remained due to a slight swelling of the infraorbital region on the left, nasal voice. In the oral cavity the exposure of the bone of the alveolar process within the boundaries of 2.1 - 2.6 teeth is observed, when probing from the side of the palate - a pathological pocket extending in the direction of the soft palate to a depth of more than 2.0 cm. A slight purulent discharge from the granulating wound remains. Teeth 1.1, 1.2 are mobile 3 degrees, 2.7 - immobile (Fig. 2.).

Figure 2. *The view of the oral cavity of the patient M. Sequestration of the upper jaw on the left 2 months after the operation of tooth extraction, periostectomy.*

According to computed tomography with 3D reconstruction, there is a bone sequester in the region of the alveolar and palatine processes of the upper jaw with a demarcation zone (Fig. 3.A, 3.B, 3.C). A decision was made to perform a sequestrectomy.

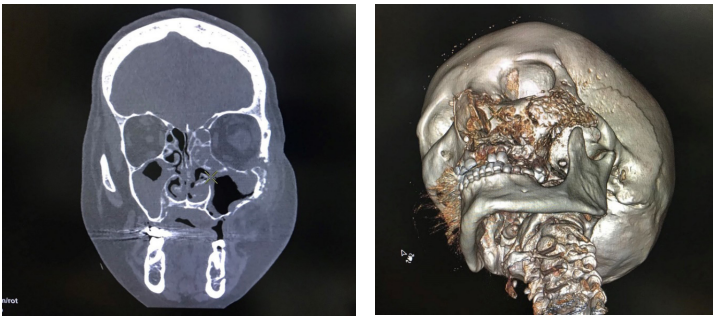

Figure 3A and 3B. *The computed tomogram of the patient M., 2 months after the operation of tooth extraction, periostotomy. Front and Horizontal cuts.*

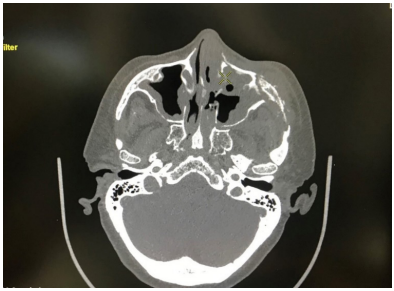

Figure 3C. *The computed tomogram of patient M., 3D reconstruction, 2 months after tooth extraction, periostectomy.*

The operation was performed under general anesthesia (intubation anesthesia). Teeth 1.1, 1.2 were removed; using a raspator, without much effort. The bone sequester formed by the alveolar process of the upper jaw within 1.2–2.6 teeth and the palatine process of the upper jaw with the nasal crest and lower part of the vomer is dislocated into the oral cavity (Fig. 4A., 4B.).

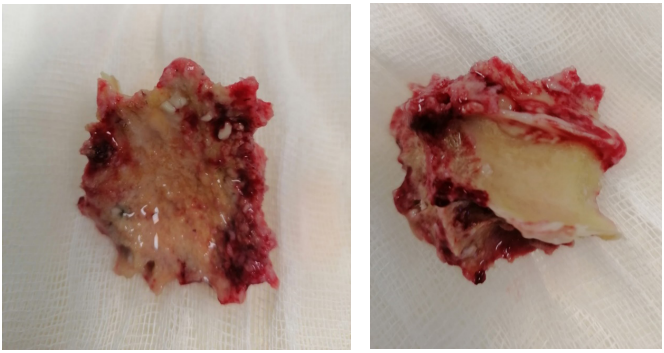

Figure 4A and 4B. *The sequester of the upper jaw, palatal and nasal surfaces.*

A defect was formed, communicating the oral cavity with the nasal cavity and the maxillary sinus on the left. In the sinus there is a polyposis-altered, partially necrotic, mucous membrane, which is removed and sent for histological examination. The edges of the wound are mobilized, brought together, the wound is sutured tightly.

Unfortunately, on the 7th day there was a divergence of the wound edges at the level of tooth 2.6, subsequently the defect increased, despite the manufacture of a protective plate that separates the oral cavity, nose and maxillary sinus (Fig. 5, Fig. 6).

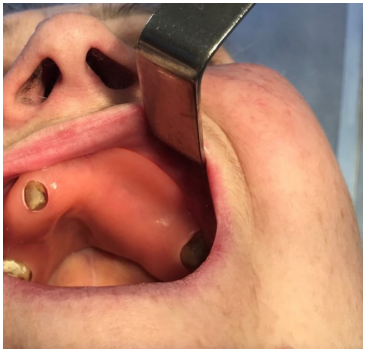

Figure 5. *The view of the oral cavity of the patient M. The communication of the oral cavity with the maxillary sinus and the nasal cavity on the left.*
Figure 6. *The view of the oral cavity of the patient M. with a protective plate applied.*

Discussion

Osteonecrosis of the jaw bones is a complex inflammatory disease, most often of odontogenic etiology, which is most severe in the lower jaw. A lighter, "benign" course of the disease in the upper jaw with no extensive destruction of bone tissue, the rare development of phlegmon in the adjacent soft tissues is explained by its anatomical and topographic features - good vascularization, the presence of a large number of holes in the compact layer, which contributes to the rapid evacuation of purulent exudate under periosteum or submucosal. In some cases, the maxillary sinus is involved in the inflammatory process. At the same time, the spread of the inflammatory process from the maxillary sinus deep into can lead to bone damage and the development of osteonecrosis of the upper jaw. In the upper jaw, peripheral sequesters are predominantly formed, in contrast to osteonecrosis of the bone caused by desomorphine or treatment with bisphosphonates, in particular zolidronic acid. In this case, significant areas of necrosis are predominantly formed, including the maxillary bone, areas of the zygomatic bone. In our case, we observed the formation of an extensive sequester in the upper jaw in a patient with comorbid pathology after a new coronavirus infection.

Conclusions

Thus, a violation of microcirculation in bone tissue caused by the direct effect of the SARS-CoV-2 virus on ACE-2 receptors in the vascular endothelium leads to the development of a widespread destructive inflammatory process with the formation of extensive areas of necrosis during exacerbation of existing foci of chronic odontogenic infection.

References

1. *Corman V.M. et al. Detection of 2019 novel coronavirus (2019-nCoV) by real-time RT-PCR //*
2. *https://www.eurosurveillance.org/content/10.2807/1560-7917.ES.2020.25.3.2000045#abstract_content. Дата обращения 12.04.2021.*
3. *Bassetti M. The Novel Chinese Coronavirus (2019-nCoV) Infections: challenges for fighting the storm. https://doi.org/10.1111/eci.13209 URL: https://onlinelibrary.wiley.com/doi/abs/10.1111/eci.13209.*
4. *https://www.who.int/emergencies/diseases/novel-coronavirus-2019/technical-guidance/naming-the-coronavirus-disease-(covid-2019)-and-the-virus-that-causes-it.*
5. *Severe acute respiratory syndrome coronavirus 2 isolate Wuhan-Hu-1, complete genome. GenBank: MN908947.3. https://www.ncbi.nlm.nih.gov/nuccore/MN908947.3.*
6. *Hakobyan K.A., Poghosyan YuM . Spontaneous closure of bilateral oro-antral communication formed after maxillary partial resection in "Krokodil" drug related jaw osteonecrosis patient: case report /. THE NEW ARMENIAN MEDICAL JOURNAL Vol.11 (2017), No 3, p. 78-80*
7. *Wuhan Municipal Health Commission briefi ng on the pneumonia epidemic situation. 31 December 2019 (in Mandarin). http://wjw.wuhan.gov.cn/front/web/showDetail/2019123108989.*
8. *V.V. Nikiforov, T.G. Suranova, T.Ya. Chernobrovkina, Ya.D. Yankovskaya, S.V. Burova / Novel coronavirus infection (covid-19): clinical and epidemiological aspects// Archives of Internal Medicine • No. 2 • 2020, pp. 87-93.*
9. *Omarova Kh.G., Makashova V.V., Ponezheva Zh.B., Usenko D.V., Maleev V.V., Akimkin V.G. Some aspects of the pathogenesis of Covid-19 and possible pathogenetic methods of prevention and treatment / / Electronic document https://covid19-preprints.microbe.ru/files/47 / date of access 11.04.2021.*
10. *Romanov B.K. Coronavirus infection COVID-2019. Safety and risk of pharmacotherapy. 2020;8(1):3–8.*
11. *https://doi.org/10.30895/2312-7821-2020-8-1-3-8.*
12. *Ruzhentsova T. A., Khavkina D. A., Chukhlyaev P. V., Garbuzov A. A., Meshkova N. A. 2020. Myocardial lesions in patients with Covid-19. Covid19-preprints.microbe.ru. https://doi.org/10.21055/preprints-3111815.*
13. *Shargorodsky A. G. Inflammatory diseases of the tissues of the maxillofacial region and neck // Moscow: GOU VUNMTs of the Ministry of Health of the Russian Federation, 2001. - 273 p.*

DOI 10.34660/INF.2023.98.34.054

CHARACTERISTICS OF CARDIOVASCULAR DISORDERS IN CHRONIC OPISTHORCHIASIS [1]

Karbysheva Nina Valentinovna
Doctor of Medical Sciences, Head of Department
Altai State Medical University
Nikonorova Marina Anatolyevna
Doctor of Medical Sciences, Full Professor
Altai State Medical University

Beskhlebova Olga Vasilyevna
Doctor of Medical Sciences, Associate Professor
Altai State Medical University
Plotnikova Ekaterina Yurievna
Doctor of Medical Sciences, Full Professor
Kemerovo State Medical University

Ivanova Maria Eduardovna
Applicant of the Department
Altai State Medical University

Annotation. *Relevance. Altai Krai is one of the most intense foci of opisthorchiasis invasion. Manifestations of autonomic dysfunction are a predisposing factor in the development of cardiovascular pathology and can serve as an indicator of cardiovascular disorders. In clinical practice, non-invasive methods that determine heart rate variability are most widely used to assess autonomic dysfunction.*

Purpose of the study: *to assess the nature of cardiovascular disorders in patients with chronic opisthorchiasis.*

Material and methods. *46 patients with a diagnosis of chronic opisthorchiasis verified by coproovoscopic and/or duodenal probing were examined by random sampling. In order to study the manifestations of autonomic dysfunction, daily monitoring of ECG and BP was used. Frequency and spectral analyzes of the heart rate were performed using the Korveg software.*

[1] The study is being carried out in accordance with the State task for 2021-2023. "Technologies for predicting and preventing combined pathology of the liver and cardiovascular system in opisthorchiasis invasion".

Results. *In patients with chronic opisthorchiasis, before deworming, manifestations of autonomic dysfunction were characterized by increased activity of the sympathetic nervous system. The prevalence of sympathicotonia and activity of the central regulatory systems in chronic opisthorchiasis was revealed (indices of regulatory systems of the autonomic nervous system - IVR, p = 0.003 and INRS, p = 0.001). As shown by the data of this study, the manifestations of cardiovascular disorders in opisthorchiasis invasion are expected in at least 69% of cases, with a confidence limit of 69-98% and an average estimate of 88%. The development of autonomic dysfunction can act as a trigger for various prenosological changes, functional arrhythmias, which in the future provide pathology from the cardiovascular system during opisthorchiasis invasion.*

Key words: *opisthorchiasis, cardiovascular disorders, autonomic dysfunction.*

The Ob-Irtysh basin is the largest endemic area for opisthorchiasis, which belongs to the category of “uncontrollable” parasitic diseases in our country. In the middle reaches of the Ob and the lower reaches of the Irtysh, the incidence of the local population reaches 70-80% and even 90%. The uniqueness of the natural data of the region, the peculiarities of the hydrological regime ensure the stable functioning of opisthorchiasis foci throughout its territory. Altai Krai is one of the most significant natural foci of opisthorchiasis not only in Western Siberia, but also on the territory of the Russian Federation as a whole [1]. The incidence rate of this helminthiasis in the territory of the region is from 44 to 34 per 100 thousand of the population, which exceeds the national figure of 12 to 15 per 100 thousand of the population by 2 or more times, while the incidence of carp fish in the Ob-Irtysh basin ranges from 70 up to 90% [2]. The long-term coexistence of helminths with the human body often leads to serious consequences, which cannot but affect the general level of health of the population of endemic territories. With opisthorchiasis, not only allergies develop, but also dysfunctions of many organs and systems: liver, immune and cardiovascular systems, digestive organs, etc. The diversity and non-specificity of the clinical manifestations of opisthorchiasis expands the relevance of this problem to an interdisciplinary one and requires an increase in the effectiveness of care for such patients.

The primary habitat of opisthorchis is the hepatobiliary system, as well as the ducts of the pancreas. The liver is regulated by both the sympathetic and parasympathetic branches of the central nervous system, which play a critical role in energy homeostasis, organ damage, and repair. In various liver diseases, autonomic dysfunction is a frequent clinical manifestation and can aggravate their course.

Autonomic dysfunction is a predisposing factor in the development of cardiovascular pathology (arrhythmias, coronary heart disease) and an indicator of cardiovascular disorders, the risks of which are believed to be associated with

liver diseases [3]. Increased workload on the heart due to altered sympathetic activity and defective parasympathetic response may contribute to functional and structural changes in the heart. In a study by D. Houghton et al., it was found that sustained sympathetic activity is a stimulus for structural and functional changes in cardiomyocytes and the interstitium of the heart muscle, left ventricular remodeling, and ventricular tachyarrhythmia [4]. In clinical practice, non-invasive methods that determine heart rate variability are most widely used to assess autonomic dysfunction [5].

Identification of the influence of autonomic dysfunction and the nature of cardiovascular disorders in chronic opisthorchiasis is of practical importance for determining adequate therapeutic interventions that are aimed at reducing the risks of cardiovascular diseases in such patients.

Purpose of the study: to assess the nature of cardiovascular disorders in patients with chronic opisthorchiasis.

Material and methods of research From 2021 to 2022, 46 patients with chronic opisthorchiasis aged 18 to 55 years were examined by random sampling on the basis of the KGPFHCI “Regional Clinical Hospital” outpatient department. All examined patients underwent deworming of opisthorchiasis on the basis of the infectious diseases departments of the State Budgetary Institution of Healthcare “City Hospital No. 11, Barnaul”.

Criteria for inclusion in the study: laboratory-confirmed opisthorchiasis; age from 18 to 45 years for men, 18-55 years for women, voluntary informed consent to participate in the study. Criteria for exclusion from the study: the presence of other parasitic invasions according to serological and coproovoscopic studies (echinococcosis, trichinosis, toxocariasis, ascariasis, etc.), the presence of acute and chronic liver diseases of an infectious (viral hepatitis) and somatic nature (alcoholic, autoimmune, against the background of metabolic violations); a history of cardiovascular disease; early family history of cardiovascular disease (women under 65, men under 55); smoking, alcohol abuse; a history of diseases that increase the risk of cardiovascular events: impaired glucose tolerance, diabetes mellitus type 1, 2, hypertension, coronary heart disease, congenital malformations of the cardiovascular system, blood diseases, kidney disease (glomerulonephritis, chronic kidney disease); the presence of obesity (BMI from 16 to 25); the presence of a woman in menopause, a history of eclampsia during pregnancy. The examination took into account the data and their dynamics, which were reflected in the developed “Map of clinical and laboratory examination of a patient with chronic opisthorchiasis”. Each patient was made aware of the purpose, principles, and design of the study before it began. The design of the study and its documentation were approved by the Local Committee on Biomedical Ethics (LEC) of FSBEI HE Altai State Medical University of the Russian Ministry of Health.

The examination included: collection of complaints by passive and active questioning, anamnesis of the disease, anamnesis of life, epidemiological anamnesis data with the establishment of the fact of eating river fish in anamnesis and living in an endemic territory for opisthorchiasis (Altai Territory). An objective examination was carried out using generally accepted methods of examination of organs and systems, allowing to identify the symptom complex of invasion.

The diagnosis of chronic opisthorchiasis was verified microscopically by the detection of helminth eggs in the feces (in 80.0% of patients), eggs and/or maritis of opisthorchia in the duodenal contents (in 20.0% of patients). Deworming with praziquantel (biltricid) was carried out in the inpatient department of the infectious diseases department of the KGPFHCI "City Hospital No. 11, Barnaul" in accordance with the standards of medical care and federal clinical guidelines "Opistorchiasis in adults".

In accordance with the design of the study, the main (patients with chronic opisthorchiasis, n=46) and control (n=15) groups of subjects matched by sex and age were formed.

Daily monitoring of the work of the heart (holter monitoring) was carried out using the equipment "Kardiotechnika" (INKART, St. Petersburg). The analysis of the results was carried out using the KTResult 2 program version 2.4.155, channels I, II, III, AVR, AVL, AVF, V1, V2, V3, V4, V5, V6, tones, pressure, movement, movement 2, rheopneumogram were recorded. Analysis of blood pressure (BP) monitoring was carried out according to the Korotkov method with the addition of oscillometry. The number of measurements was sufficient to assess the average values at night and the variability of blood pressure. In order to study the manifestations of autonomic dysfunction, methods of frequency and spectral analysis of the heart rate were used. The functional state of the circulatory system was assessed using the Korveg computer program (certificate No. 2000610883, dated September 8, 2000). The parameters were determined in the rest position (lying) and active orthostasis (standing). The results obtained were entered into the computer program "Korveg" with the subsequent calculation of indicators that make it possible to evaluate the activity of various parts of the autonomic nervous system: mode (Mo) characterizing the most probable level of functioning of the circulatory system; mode amplitude (AMo) reflecting the stabilizing (mobilizing) effect of centralization of heart rhythm control, due to the influence of the sympathetic division of the autonomic nervous system; variation range, considered as an indicator of the activity of the parasympathetic division of the autonomic nervous system. The following indices were calculated according to the above indicators: the regulatory system tension index (RSTI), which reflects the degree of centralization of heart rate control; vegetative balance index (VBI) indicating the ratio between the activity of the sympathetic and parasympathetic divisions of the

autonomic nervous system; an indicator of the adequacy of regulation processes (IARP), which makes it possible to judge the presence of excessive or insufficient centralization of heart rhythm control; centralization index (CI) characterizing the degree of relative activation of subcortical and higher levels of heart rate control; vegetative rhythm indicator (VRI), which allows to judge the vegetative balance from the point of view of assessing the activity of the autonomous regulation circuit.

The paper uses methods of statistical processing, depending on the type of random variables and the task of the study. Continuous values are presented as M±SD, where M is the sample arithmetic mean and SD is the standard deviation. Qualitative feature values are presented as observed frequencies and percentages. Comparison of quantitative parameters in the comparison groups was carried out using the Mann-Whitney test. The level of statistical significance in testing the null hypothesis was taken to be the corresponding $p<0.05$. The $\chi 2$ test was used to compare the frequencies of qualitative features in independent samples. In all cases, two-sided versions of the criteria were used. Calculation of point estimates of probabilities and confidence intervals for them was carried out using the Bayesian estimate for small samples and the binomial distribution model for estimating confidence limits. Processing and graphical representation of the data was carried out using computer programs Statistica 10.0 (Russian version), Excel.

Results. According to the results of the study, it was found that in the clinical polymorphism of the course of invasion, the manifestation of cardiovascular disorders was detected in 9 (19.6%) patients with chronic opisthorchiasis before treatment and was characterized by complaints of tachycardia (7 people), pain in the heart area - 1 person, severe arrhythmia - 1 person. These were patients with an invasion duration of more than five years.

In the group of patients examined using daily monitoring of ECG and blood pressure (n=15), clinical manifestations were observed in 33.3% of patients. Analysis of the results of daily monitoring of ECG and blood pressure revealed the following changes in 86.7% of the examined patients: sinus bradyarrhythmia (66.7%), pairs and triplets of ventricular and supraventricular extrasystoles (40.0%), systolic and/or diastolic hypertension (40.0 %), including those with an insufficient degree of nightly decrease in blood pressure (20.0%), an increase in the average daily pulse pressure (26.7%).

Table 1.

The frequency of cardiovascular disorders according to the data of daily monitoring of ECG and blood pressure in patients with chronic opisthorchiasis before treatment

Cardiovascular disorders	**n=15, %**
sinus bradyarrhythmia	20,0
ventricular extrasystoles	13,3
hypertension (systolic BP and/or diastolic BP)	6,7
sinus bradyarrhythmia	46,7
ventricular and / or supraventricular extrasystoles, pairs, triplets	26,6
hypertension (systolic BP and/or diastolic BP)	20,0
increase in average daily pulse pressure	26,7

When using the Bayesian method, it was found that cardiovascular disorders in opisthorchiasis invasion are expected in at least 69% of cases with a confidence limit of 69-98% and an average estimate of 88%.

Of the patients with chronic opisthorchiasis examined using the Korveg program (n=17), only 2 people complained of manifestations of the cardiovascular system (pain in the heart area, tachycardia). At the same time, a change in vegetative tone by the type of sympathicotonia and hypersympathicotonia, as a trigger for the pathology of the cardiovascular system, detected using the Korveg program, was recorded in 82.4% of the examined main group. It should also be noted that during the survey, only 1 person complained of tachycardia, while according to the results of Corveg, tachycardia (in orthostasis) was registered in 16 out of 17 examined (94.1%).

When comparing the indicators of frequency analysis according to the data of the computer program “Korveg” in patients with chronic opisthorchiasis before treatment, significantly significant changes were revealed compared to the control group. An increase in the average heart rate in orthostasis, an increase in the AMo index both in the rest position (p=0.002) and in orthostasis (p=0.0001) was revealed, which indicates the predominance of the influence of the sympathetic division of the autonomic nervous system (SNS). Spectral analysis of heart rate variability, which allows assessing the sympathetic, parasympathetic, humoral effect on heart rate, revealed a significant increase in first-order waves (LF, p= 0.012) at rest, which indicates an increasing activity of vasomotor and baroreflex mechanisms in the supine position and the possibility of development inappropriate reactions to physical activity.

In the main group, prior to treatment, a significant pronounced shift in autonomic homeostasis towards activation of the sympathetic division of the nervous system was revealed. In comparison with the control group, the regulatory system tension index (RSTI) in orthostasis was 2.27 times higher (p=0.001), the vegeta-

tive balance index (VBI) in orthostasis was 1.8 times higher (p= 0.003), which reflects an increase in sympathetic load regulation. The indicator of adequacy of regulation processes (IARP) was also significantly increased both in the rest position (p=0.019) and in orthostasis (p=0.0001), which indicates excessive centralization of heart rate control and can be considered as a marker of reduced functional and adaptive capabilities of the body as a result of the constant functional stress of the systems that regulate the rhythm of the heart.

A significant increase was also noted in the centralization index (CI) in the standing position (p=0.002), which reflects a more pronounced activation of higher levels of heart rate control.

Thus, vegetative homeostasis at rest and during exercise in the main group in patients with chronic opisthorchiasis was characterized by the predominance of the influence of the sympathetic nervous system. When assessing the adaptive capabilities of patients in the main group, functional and/or moderate tension of regulatory systems was revealed during exercise in 68.4% and 28.6% of cases, respectively (Tables 5, 6).

Table 2.

Parameters of frequency and spectral analysis in patients with opisthorchiasis before treatment and in the control group (M±SD)

Indicators of frequency and spectral analysis	**Patients, n=17**	**Control group,n=15**	**P, for the Mann-Whitney test**
CR (c)	94,08±12,89	84,60±12,98	0,0216
AMo (л)	42,53±12,94	29,84±7,65	0,002
AMo (c)	53,52±14,24	33,53±7,63	0,0001
LF (л)	0,31±0,70	0,18±0,11	0,012
RSTI (c)	412,29±228,76	181,30±94,63	0,001
VBI (c)	503,14±247,32	272,72±152,90	0,003
IARP (л)	48,86±18,08	34,99±9,68	0,019
IARP (c)	86,03±27,48	47,02±13,54	0,0001
CI (c)	412,29±228,76	190,80±109,18	0,002

Note: s - standing, l - lying

Table 3.

Comparative analysis of autonomic homeostasis in patients with chronic opisthorchiasis before treatment and control group (%)

Indicators	**Patients, n=17**	**Control group, n=15**	**P, for the Mann-Whitney test**
Vegetative homeostasis with a predominance of SNS (l)	31,6	4,8	0,03
Vegetative homeostasis with a predominance of SNS (s)	63,2	14,3	0,025
Voltage Regulatory Systems	68,4	28,6	0,02

Conclusion. As shown by the data of this study, manifestations of cardiovascular disorders in opisthorchiasis invasion are expected in at least 69% of cases with a confidence limit of 69-98% and an average estimate of 88%.

It was found that in patients with chronic opisthorchiasis before deworming, the clinical manifestation of cardiovascular disorders was less common (33.3%) than according to the results of instrumental studies - daily monitoring of ECG and blood pressure (86.7%), ($p<0.001$). Manifestations of autonomic dysfunction were observed in all examined and were characterized by an increase in the activity of the sympathetic nervous system in 82.4% of cases. Along with sympathicotonia, the predominance and activity of the central regulatory systems in chronic opisthorchiasis was revealed (indices of regulatory systems of the autonomic nervous system - VBI, $p = 0.003$ and RSTI, $p = 0.001$). Prolonged vegetative dysfunction can act as a trigger for various prenosological changes, functional rhythm disturbances, which provide further pathology from the cardiovascular system.

The assessment of the frequency and nature of cardiovascular disorders in chronic opisthorchiasis is of practical importance for determining indicators of the risk of developing cardiovascular diseases and targeted prevention in such patients.

References

1. Belyaeva M.I., Stepanova T.F., Methodiev V.V., Pustovalova V.Ya. Estimation of infestation of fishes of the cyprinid family with opisthorchis metacercariae in the hyperendemic focus of Western Siberia // Population health and habitat. – 2016. – No. 2 (75). – P32-34.

2. On the state of sanitary and epidemiological well-being of the population in the Russian Federation in 2020: State report. M.: Federal Service for Supervision of Consumer Rights Protection and Human Welfare, 2021. 256 p.

3. Amlaev K.R. Dyslipidemia: epidemiology, clinic, diagnosis, prevention and treatment // Vrach. – 2021. – V. 32. – No. 5. – P. 16-20.

4. The degree of hepatic steatosis associates with impaired cardiac and autonomic function D. Houghton, P. Zalewski, K. Hallsworth, S. Cassidy, C. Thoma, L. Avery, J. Slomko, T. Hardy, A. D. Burt, D. Tiniakos, K. G. Hollingsworth, R.Taylor, C. P. Day, S. Masson, S.M Pherson, Q. M. Anstee, J. L. Newton and M. I. Trenell Journal of Hepatology, 2019-06-01, Vol. 70, Issue 6, Pages 1203-1213.

5. G. Boudet, G. Walther, D. Courteix, P. Obert, B. Lesourd, B. Pereira, et al. Paradoxical dissociation between heart rate and heart rate variability following different modalities of exercise in individuals with metabolic syndrome: the RESOLVE study Eur J Prev Cardiol, 24 (2017), pp. 281-296

DOI 10.34660/INF.2023.31.53.055

ADAPTIVE POTENTIAL FOR SARCOPENIC OBESITY IN ELDERLY AGE

Plutnickiy Andrey Nikolaevich
Doctor of Medical Sciences, Associate Professor, Head of Department
Biomedical University of Innovation and Continuing Education of the State Scientific Center of Russia - Burnasyan Federal Medical Biophysical Center of Federal Medical Biological Agency of Russia

Shadrin Konstantin Alexandrovich
Postgraduate
Biomedical University of Innovation and Continuing Education of the State Scientific Center of Russia - Burnasyan Federal Medical Biophysical Center of Federal Medical Biological Agency of Russia

Kurilo Irina Nikolaevna
Research Officer
Research Medical Center "Gerontology"

Karimova Daniia Iusufovna
Doctor of Medical Sciences, Full Professor
Biomedical University of Innovation and Continuing Education of the State Scientific Center of Russia - Burnasyan Federal Medical Biophysical Center of Federal Medical Biological Agency of Russia

Abstract. *Sarcopenia is an age-associated atrophic degenerative change in skeletal muscles, leading to a loss of strength and volume, contributes significantly to an increased risk of disability, and is one of the five risk factors for mortality in the elderly. The article presents the results of studying the adaptive potential in sarcopenic obesity in the elderly: in practically healthy elderly people, a normal level of adaptation was observed, in people with obesity, adaptation strain, in people with sarcopenia, unsatisfactory adaptation, and in people with sarcopenic obesity, adaptation failure. To predict the decline in functional ability after 60 years, it is advisable to use the continuum obesity - sarcopenia - sarcopenic obesity, to determine the level of energy metabolism.*

Introduction. Sarcopenia is an age-associated atrophic degenerative change in skeletal muscles that leads to loss of strength and volume, contributes significantly to an increased risk of disability, and is one of the 5 risk factors for mortality in the elderly. The term "sarcopenic obesity", reflecting the combination of obesity and sarcopenia, has been used relatively recently. Currently, there is an increase in the prevalence of both sarcopenia and sarcopenic obesity, which is due, on the one hand, to an increase in life expectancy of the population (in 2000 there were about 600 million people over 60 years old, and by 2050 up to 2 billion are expected).). On the other hand, this is due to an increase in the prevalence of obesity in the population [1-6].

The purpose of this work is to study the adaptive potential in sarcopenic obesity in the elderly.

Materials and methods

The study included 162 elderly people aged 65 to 74 years, incl. 72 men and 90 women, the average age of the patients was 69.2+3.4 years.

All people were divided into 4 groups. The 1st group included practically healthy elderly people (38 people), the 2nd group - obese, but not having sarcopenia (46 people), the 3rd - elderly people with sarcopenia, but not obese (37 people), in the 4th - people with sarcopenic obesity (41 people). The relevant characteristics are shown in table 1.

All people included in the study underwent anthropometric measurements: measurement of height, body weight, measurement of waist, hips, their ratio, calculation of the Quetelet index. Also, a bioimpedance study was performed using the AVS-02 Medass equipment (Russia), muscle strength was measured using a DMER-120-0.5-D dynamometer (Tves, Russia).

The interpretation of the results of the study was carried out in accordance with the recommendations of the European Working Group on Osteoporosis and Sarcopenia (2009).

Blood samples were taken from all people included in the study.

The state of adaptation of the body was assessed on the basis of anthropometric and hemodynamic data, as well as biochemical blood parameters: the content of adenosine triphosphate (ATP), adenosine diphosphate (ADP) and lactate dehydrogenase (LDH). The cell energy potential (EP) was calculated, reflecting the rate of mitochondrial respiration according to the ratio: EP = ATP/ADP. The level of adaptation was characterized based on the values of the adaptive potential (AP), the calculation of which was carried out according to the method of R.M. Baevsky in the modification of A.P. Berseneva et al. (1987, 1997) according to the following formula:

AP (in points) = 0.011 • (HR) + 0.014 • (SBP) ++ 0.008 • (DBP) + 0.014 • (age, years) ++ 0.009 • (body weight, kg) – 0.009 • (height, cm) - 0.27,

where HR is the heart rate (per minute); SBP - systolic blood pressure (mm Hg); DBP - diastolic blood pressure (mm Hg).

Index values were taken as satisfactory adaptation

AP = 2.1 and below, the adaptation voltage was stated at values from 2.11 to 3.2 points; at values from 3.21 to 4.3 - unsatisfactory adaptation and from 4.3 and above - failure of adaptation.

For statistical analysis of the results obtained during the study, we used the Student's t-test. and the 0-distribution hypothesis, wherein the difference in scores is significant at t 2, in which case $p<0.05$. The Upton method was also applied (the study of data in contingency tables «2x2» to assess the differences between non-parametric parameters with the calculation of the indicator $\chi 2$. Statistical processing of the data was carried out, which were entered into Excel spreadsheets, mathematical and statistical analysis of the data was carried out using program «Statgraphics plus for Windows», version 11.0.

Results and its discussion

Table 1 shows the characteristics of adipose tissue in the composition of the body of the elderly, depending on the presence / absence of sarcopenia and obesity. The index of fat mass in obesity (Group 2) and sarcopenic obesity (Group 4) was comparable and amounted to 27.1+0.7 kg and 26.2+0.2 kg, respectively. At the same time, the indicator of fat mass in obesity was significantly higher ($p<0.05$) than in people without obesity and sarcopenia (Group 1), in which this indicator was 18.1+0.6 kg, and in elderly people with sarcopenic obesity, this indicator was significantly higher ($p<0.05$) than in people with sarcopenia (group 3), in which it was 17.2 + 0.5 kg.

The proportion of fat in obesity (Group 2) and sarcopenic obesity (Group 4) was comparable and amounted to 35.8+0.03% and 32.7+0.02%, respectively. At the same time, the indicator of fat mass in obesity was significantly higher ($p<0.05$) than in people without obesity and sarcopenia (Group 1), in which this indicator was 28.5+0.02, and in elderly people with sarcopenia In obese patients, this indicator was significantly higher ($p<0.05$) than in people with sarcopenia (Group 3), in whom it was 26.4+0.01.

Table 1

Body composition data in the elderly

Index	**Patients groups**			
	1 (n=38)	**2 (n=46)**	**3 (n=37)**	**4 (n=41)**
Fat mass (kg)	18,1±0,6	27,1±0,7*	17,2±0,5	26,2±0,2*
Fat percentage (%)	28,5±0,02	35,8±0,03*	26,4±0,01	32,7±0,02*
Subcutaneous fat (cm2)	211,3±4,0	261,1±2,2*	215,1±4,1	256,2±3,2*

Visceral fat (cm^2)	46,2±0,3	65,9±2,9*	45,2±0,4	62,2±1,8*
Body mass index (kg/m^2)	23,2±1,1	33,1±0,7*	21,4±2,0**	26,2±3,1**

*p<0.05 compared with the 1st (control) group and with the 3rd group (with sarcopenia);

**p<0.05 compared to group 2 (obese).

The index of subcutaneous fat in obesity (Group 2) and sarcopenic obesity (Group 4) was also comparable and amounted to 261.1+2.2 cm^2 and 256.2+3.2 cm^2, respectively. At the same time, the indicator of fat mass in obesity was significantly higher (p<0.05) than in people without obesity and sarcopenia (Group 1), in whom this indicator was 211.3+4.0 cm^2, and in elderly people with in sarcopenic obesity, this indicator was significantly higher (p<0.05) than in people with sarcopenia (group 3), in whom it was 215.1+4.1 cm^2. A similar picture was observed in the analysis of indicators characterizing visceral fat. The indicator of visceral fat in obesity (Group 2) and sarcopenic obesity (Group 4) was also comparable and amounted to 65.9+2.9 cm^2 and 62.2+1.8 cm^2, respectively. At the same time, the indicator of fat mass in obesity was significantly higher (p<0.05) than in people without obesity and sarcopenia (Group 1), in which this indicator was 46.2+0.3 cm^2, and in elderly people with in sarcopenic obesity, this indicator was significantly higher (p<0.05) than in people with sarcopenia (group 3), in whom it was 45.2+0.4 cm^2.

Thus, it turned out that the characteristics of adipose tissue in the body of elderly people who are practically healthy and those with sarcopenia are identical. Characteristics of fat in the body composition of people with sarcopenic obesity were generally similar to those in people with obesity, with the exception of the body mass index, which was significantly lower (26.2+3.1 kg/m^2 vs. 33.1+0.7 kg /m^2, p<0.05), which is explained by the loss of muscle mass.

We studied adaptation rates in the elderly depending on the presence/absence of sarcopenia and obesity (Table 2).

Table 2

Data on adaptation levels (adaptive potential) in elderly patients

Index	**Group**			
	1 (n=38)	**2 (n=46)**	**3 (n=37)**	**4 (n=41)**
Normal adaptation (Person /%)	9 (23,6%)	3 (6,5 %)	0	0
Adaptation voltage (Person/%)	26 (68,5%)	21 (45,8 %)	9 (24,3 %)	8 (19,5 %)
Unsatisfactory adaptation (Person /%)	3 (7,9 %)	17(36,9%)	12 (32,5%)	6 (14,7%)
Disruption of adaptation (Person /%)	0	5 (10,8%)	16 (43,2 %)	27 (65,8 %)
AP, points	2,0±0,02	2,9±0,04*	3,4±0,03*,**	4,4±0,07*,**,#

*p<0.05 compared with the 1st (control) group;
**p<0.05 compared with group 2 (obese);
#p<0.05 compared to the 3rd group (with sarcopenia).

Analysis of adaptation in elderly patients showed the following results. Thus, in the group of practically healthy elderly people, the level of normal adaptation was 23.6%, the level of stress of adaptation was 68.4%, the level of unsatisfactory adaptation was 7.9%, and the indicator of the level of adaptation failure was 0. For a group of people with obesity , but without sarcopenia, the following results were obtained: the level of normal adaptation - 6.5%, the level of stress of adaptation - 45.6%, the level of unsatisfactory adaptation - 36.9%, the level of adaptation failure - 10.8%. In the group of elderly people with sarcopenia, but not obese, the indicators were as follows: the level of normal adaptation - 0, the level of stress of adaptation - 24.3%, the level of unsatisfactory adaptation - 32.4%, the level of adaptation failure - 43.2% . In the group of people with sarcopenic obesity, the indicator of normal adaptation was equal to 0, the level of stress of adaptation was 19.5%, the level of unsatisfactory adaptation was 14.6%, the level of adaptation failure was the highest in comparison with other groups - 65.8%.

Conclusions

1. Practically healthy elderly people had a normal level of adaptation, people with obesity had a strain of adaptation, people with sarcopenia had an unsatisfactory adaptation, and people with sarcopenic obesity had a failure of adaptation.

2. With an increase in the degree of carbohydrate metabolism disorder, an increasing decrease in the adaptive capabilities of the body took place, and the development of senile asthenia in the form of sarcopenia as its manifestation potentiates this negative cascade up to a breakdown in adaptation during the development of sarcopenic obesity.

3. To predict the decline in functional ability after 60 years, it is advisable to use the continuum obesity - sarcopenia - sarcopenic obesity.

4. To develop comprehensive gerontological programs in the detection of sarcopenic obesity, it is advisable to use not only standard methods, such as bioimpedancemetry, but also to determine the level of energy metabolism, which reaches maximum values in sarcopenic obesity, which should be considered as a predictor of adaptation failure and risks of a progressive decrease in functional ability .

References

1. *Бочарова К.А., Герасименко А.В., Жабоева С.Л. К вопросу об ассоциации Bocharova K.A., Gerasimenko A.V., Zhaboeva S.L. To the question of the association of sarcopenia with the main geriatric syndromes // Modern problems of science and education. 2014._ No. 6._C. 1036–1043 [Bocharova K.A., Gerasimenko A.V., Zhaboeva S.L. K voprosu ob assotsiatsii sarkopenii s osnovnymi geriatricheskimi sindromami // Sovremennye problemy nauki i obrazovaniya. 2014._ No. 6._ P. 1036–1043 (in Russian)].*

2. *Povoroznyuk V.V., Dzerovich N.I. Sarcopenia. Literature review and results of own research // Reproductive endocrinology. 2013._ No. 1._ P. 16-23 [Porovoznyuk V.V., Dzerovich N.I. Sarkopeniya. Obzor literatury i rezultaty sobstvennyh issledovanij // Reproduktivnaya endokrinologiya. 2013._ No. 1._P. 16–23 (in Russian)].*

3. *Cruz-Jentoft A.J., Baeyens J.P., Bauer J.M. et al. Sarcopenia. European consensus on definition and diagnosis: report of the European Working Group on Sarcopenia in older people // Age Ageing. 2010. Vol. 39(4). P. 412–423.*

4. *Delmonico M.J., Harris T.B., Lee J.S. et al. Alternative definitions of sarcopenia, lower extremity performance, and functional impairment with aging in older men and women // Journal of the American Geriatrics Society. 2007. Vol. 55(5). P. 769–774.*

5. *Pasca Luminita Aurelia, Dogaru Gabriela, Donca Valer. Sarcopenia: diagnosis, stages and treatment // Balneo Research Journal 2015. Vol. 6(1). P. 32–35.*

6. *Rosenberg I.H. Sarcopenia: origins and clinical relevance // The Journal of Nutrition 1997. Vol. 127(5). P. 990S–991S.*

DOI 10.34660/INF.2023.39.62.056

BASIC MECHANOTHERAPY DEVICES IN THE REHABILITATION OF PATIENTS WITH SPINAL DYSFUNCTION

Plutnickiy Andrey Nikolaevich
Doctor of Medical Sciences, Associate Professor, Head of Department
Biomedical University of Innovation and Continuing Education of the State Scientific Center of Russia - Burnasyan Federal Medical Biophysical Center of Federal Medical Biological Agency of Russia

Kurnosenko Viacheslav Yrevich
Postgraduate
Biomedical University of Innovation and Continuing Education of the State Scientific Center of Russia - Burnasyan Federal Medical Biophysical Center of Federal Medical Biological Agency of Russia

Osipov Kirill Vladimirovich
Head of the day hospital
State Scientific Center of Russia - Burnasyan Federal Medical Biophysical Center of Federal Medical Biological Agency of Russia

Lobinskiy Oleg Aleksandrovich
Research Officer
Research Medical Center "Gerontology"

Introduction.

Vertebral osteochondrosis ranks first, accounting for 48% of all diseases of the nervous system. Scientists and leading experts say that a person under 30, even leading an active lifestyle, once a year needs a correction of the spine, and at 40 and older, at least 2 times a year, a preventive treatment of the spine should be performed. The reasons for most cases of treatment of diseases of the spine or heavy physical activity, or a long tense posture (sitting). In these categories of patients, the musculoskeletal system of the spine weakens, the back muscles cease to play the role of shock absorbers of the vertebrae, the nerve roots are infringed, and the so-called "lumbago" occurs. Methods of medical rehabilitation based on mechanotherapy are pathogenetically justified and effective for the largest number of patients with diseases of the spine.

The purpose of this work is to describe our own experience of using devices for mechanotherapy.

Material and methods. The work used our own observations made during the implementation of rehabilitation programs during 2019-2022 in 628 patients with spinal dysfunction. This work is descriptive in nature and aims to familiarize practitioners with the possibilities of mechanotherapy. In the work, the devices of the Research and Production Enterprise "ORMED" (Ufa) were used.

Results and its discussion.

A variant of a professional decompression apparatus for traction and vibration-thermal, roller massage of the spine is the ORMED-professional apparatus. Its features: local traction when the angles of traction change, it is possible to locally stretch exactly the part of the spine in which the problem arose; color touch LCD control panel, allows you to set all the parameters of the procedure, load, time, mode, type of traction, rate of increase in load, rate of decrease, rest time. All this can be visually controlled on the real-time traction graph during the procedure and the parameters can be changed at any time. Areas of traction: cervical spine; lumbosacral spine; joints of the upper and lower extremities. Traction force: for the cervical region from 2 to 20 kg, for the lumbosacral spine from 2 to 60 kg. Stretching modes: constant (continuous) stretching with the use of a constant dosed force in a continuous time interval; variable traction - for short intervals of time, the dosed effort increases or decreases; differentiated traction - in the frontal plane (achieved due to the difference in the lengths of the traction belts. In this case, the length of the belt on the diseased side is greater than that of the healthy one); vector extension - in the sagittal plane in front and behind (achieved by changing the angle of traction with respect to the horizon).

Therapeutic effects: unloading of the spine, by increasing the distance between the vertebrae; non-surgical treatment of herniated intervertebral discs by reducing the hernial protrusion and reducing (decompression) intradiscal pressure; elimination of subluxations in the intervertebral joints, which gives a decompressive effect, eliminating disc displacement and curvature of the spine; improves blood circulation and trophism of the entire spinal column; the muscular corset of the spine is strengthened.

An example of the installation of horizontal and vertical traction of the spine is "ORMED traction". The traction device is designed for professionals who combine traction, manual therapy and medical massage. Stretch options: horizontal, vertical. Traction areas: cervical spine, lumbosacral spine, joints of the upper and lower extremities. Traction force: for the cervical region from 2 to 15 kg; for the lumbosacral region from 2 to 70 kg. Therapeutic effects: non-surgical treatment of herniated intervertebral discs, by reducing the hernial protrusion and reducing (decompressing) internal pressure; treatment of osteochondrosis and degenerative-dystrophic diseases of the spine; treatment of protrusions of intervertebral discs; treatment of curvature of the spine, scoliosis. Stretching modes: constant

stretching mode; the constant traction mode is most often used to perform local traction (on a specific area of the body, joint or SMS) and has mainly a decompression effect. The effectiveness of this stretching regimen is increased when combined with various types of physical therapy, manual therapy and reflexology. Continuous traction mode is successfully used by traumatologists, orthopedists in the treatment of diseases of the spine and joints of the upper and lower extremities.

Variable traction mode: variable (intermittent) traction - for short periods of time, the dosed force increases or decreases. Intermittent traction is more effective than continuous traction and the impact is less sharp and intense. Intermittent stretching consists in the fact that fast traction, performed over a different period of time (the strength of traction varies), is replaced by fast relaxation, performing stretching with a given rhythm. Intermittent and continuous tractions are often combined to obtain an effective result.

It is also possible to note the following variants of devices: the apparatus of physiological traction "ORMED prophylactic" (traction is carried out on an inclined plane under the influence of the patient's own body weight - autogravitational traction); "Ormed relax" (apparatus for roller vibration-thermal mechanical massage); "AQUATRACTION" (automated complex for underwater traction and hydro-aeromassage with a counter patient lift. The success of treatment with underwater traction is explained by the fact that in warm water, under the influence of a small load on the spine, there is complete relaxation of the muscles and stretching of the paravertebral elastic tissues and ligaments); "ORMED - kineso" (installation for active-passive mechanotherapy of the spine; kinesiotherapy device is designed for dosed dynamic changes in angles in the anterior-posterior directions with different modes of flexion and extension in the thoracic and lumbar spine. It allows you to perform procedures with the ability to change the frequency and height of the amplitude In this case, there is a non-forced traction of the spine in a passive mode, when lying down without the active participation of the muscles of the body. This has a therapeutic and training effect on the ligaments of the vertebrae and intervertebral discs, contributes to the prevention and treatment of curvature of the spine, and improves the mobility of its links. In addition, therapeutic movements on the apparatus develop deep muscles that are not involved in ordinary life, restore the rhythm and depth of breathing).

Conclusions

1. Mechanotherapeutic devices for complex treatment and biomechanical correction of functional disorders of the spine are the most effective therapeutic technical means.

2. The main operating factors are dosed axial traction, local vibrational and thermal effects on the spinal column.

3. Restoration of the functions of the spine occurs in the following areas: the elimination of muscle tension and the removal of local functional blocks; increase

in range of motion and restoration (correction) of physiological curves and mobility of the spine; an increase in the intervertebral space (decompression) of the spine and the elimination of intervertebral hernias.

4. Hardware mechanotherapy contributes to the development and strengthening of the paravertebral muscles and ligaments in the form of a muscle corset, allows you to return displaced vertebrae to the correct physiological state, prevent and cure postural disorders and scoliotic deformities (curvature) of the spine.

References

1. Robotic technologies for restoring the function of walking in neurorehabilitation / V.D. Daminov [et al.]. M.: RANS, 2010. 128 p.

2. Changes in supraspinal activation patterns following robotic locomotor therapy in motor in complete spinal cord injury / P. Winchester [et al.] // Neurorehabil. Neural Repair. 2005. Vol. 19. Iss. 4. P. 313–324.

3. Effect of training intensity on physical capacity, lipid profile and insulin sensitivity in early rehabilitation of spinal cord injured individuals / P. C. de Groot [et al.] // Spinal Cord. 2003. Vol. 41. Iss. 12. P. 673–679.

DOI 10.34660/INF.2023.53.82.057

PHARMACOKINETICS AND PHARMACODYNAMICS OF EPINEPHRINE WITH ARTERIAL RECEPTORS DURING ADAPTATION TO COLD BY THE LINEWEAVER-BURK AND SKETCHARD METHOD

Ananiev Vladimir Nikolaevich
Doctor of Medical Sciences, Full Professor, Leading Research Officer
State Scientific Center of the Russian Federation Institute for Biomedical Problems of the Russian Academy of Sciences, Moscow

Ananiev Georgiy Vladimirovich
Postgraduate
Moscow Pedagogical State University

Prokopyev Nikolay Yakovlevich
Doctor of Medical Sciences, Full Professor
Tyumen State University

Gurtovoy Elisey Sergeevich
Student
Tyumen State Medical University

Abstract. *Adaptation of the body to cold requires a multifaceted restructuring of the work of many functional systems of the body. A special role in adaptation to cold is played by the sympathetic nervous system and its neurotransmitters norepinephrine and adrenaline. In our work, we studied the receptor mechanisms of regulation of the tone of the arteries of the rabbit extremity to the neurotransmitter adrenaline during 10 days of cold adaptation. Pharmacokinetic and pharmacodynamic changes in the reactivity of arterial alpha-adrenergic receptors to adrenaline were studied by the Lineweaver -Burk and Sketchard method. This made it possible to determine the number of active a-adrenergic receptors in the arteries and their sensitivity to adrenaline during adaptation to cold. The work shows that after 10 days of cold, the pressor response of the arteries to all 8 doses of adrenaline increased due to an increase in the number of active arterial adrenoreceptors by 32% and an increase in the sensitivity of adrenoreceptors to adrenaline by 50%.*

Keywords: *rabbits, cold adaptation, arteries, alpha-adrenergic receptors, epinephrine, Lineweaver -Burk and Sketchard plot.*

Introduction. Adaptation to the cold of the body occurs constantly from year to year, which activates the genetic reserves of survival in extreme conditions [1, 4]. To such long-term switching of the body's work to the cold, a multimillion-dollar temporary adaptation took place. But in the last century, the body began to undergo more often short-term adaptation to cold and maladaptation processes during subsequent stay in heat. Such short-term processes of adaptation to cold [2, 4] were not developed in the evolutionary process and caused a disturbance in the activity of the functional systems of the body. Therefore, in recent years, more and more studies have appeared to study the results of short-term adaptations to cold [4, 6, 7].

Thus, whole body heat acclimatization has been shown to increase the vasodilating response of the fingers during cold water immersion and increase the rate of hand warming, potentially improving local cold tolerance [7]. A study showed [8] that seven consecutive days of cold water immersion can reduce the intensity of chills by 36%.

The authors [6] showed that a 4-week cold acclimatization suppressed the cold-induced increase in proton leakage and decreased the intensity of shivering in skeletal muscle, observed an increase in the association between the cold-induced increase in heat production and the intensity of shivering after 4 weeks of cold acclimatization.

In the studies of Novosibirsk scientists [4], the term appeared as incomplete adaptation, when they showed that adaptation to cold occurs only after 24-5-30 days of staying in cold. According to their data, the body endured the 10-15th day of cold adaptation especially badly, which was expressed by the presence of extrasystoles, insomnia, pain in the heart, but the authors did not find out the physiological mechanisms of these symptoms.

Therefore, the aim of our research was to study the receptor mechanisms of ligand-receptor interactions of adrenaline with arterial alpha-adrenergic receptors after 10 days of cold adaptation.

Material and research methods. Studies have been carried out on male rabbits. The control group consisted of 28 rabbits kept at ambient temperature (+)18-22'C for 30 days. Cold exposure was carried out daily for 6 hours in a cooling chamber at a temperature of (-)10'C, the rest of the time the rabbits (18 animals) were at a temperature of (+)18-22'C. The vascular response of a preparation from the musculoskeletal region of the hind limb was studied when perfused with the blood of the same animal using a constant-capacity pump [3, 5]. Eight doses of epinephrine were injected intra-arterially before the pump inlet, changes in perfusion pressure were recorded with an electromanometer and recorded via an ADC in a computer.

To describe the interaction of a mediator [3] with a specific receptor, the theory of Clark and Ariens was used, which is based on the fact that the magnitude of the effect is proportional to the number of receptor-mediator complexes. The maximum effect occurs when all receptors are occupied. To analyze the response

of vascular regions, we used a graphical method for determining the parameters of mediator-receptor interaction in double inverse Lineweaver-Burk coordinates and Sketchard coordinates [3, 5]. The maximum possible pressor response (Pm) of perfusion pressure to adrenaline was determined, which was proportional to the number of active alpha-adrenergic receptors. The dissociation constant (Kd) of the mediator receptor was calculated, which was equal to the dose of adrenaline causing 50% of the maximum possible (Pm) perfusion pressure response. The value of sensitivity (1/K) of the interaction of adrenaline with adrenoreceptors of the arteries of the limb was also determined, which is numerically equal to the reciprocal of the dissociation constant (Cd).

Research results and discussion. The introduction of eight increasing doses of adrenaline caused, as in the control group, an increase in the pressor response of the perfusion pressure of the arteries of the hind limb. Comparison of the average values of the increase in perfusion pressure at doses of injected adrenaline from 0.125 μg/kg to 3.0 μg/kg showed their significant increase after 10 days of cold adaptation.

Figure 1 shows the increase in perfusion pressure (Pm mm Hg) of the control group (N) of animals and rabbits after 10 days of cooling (10 DAYS). In both groups, an increase in the dose of adrenaline leads to an increase in the pressor response to perfusion pressure (Pm). At a dose of 0.125 mcg/kg in the control group Pm=28 mm Hg. , and after 10 days of cooling, the perfusion pressure increased by 89% and amounted to Pm=54 mm Hg, this difference is significant P<0.001.

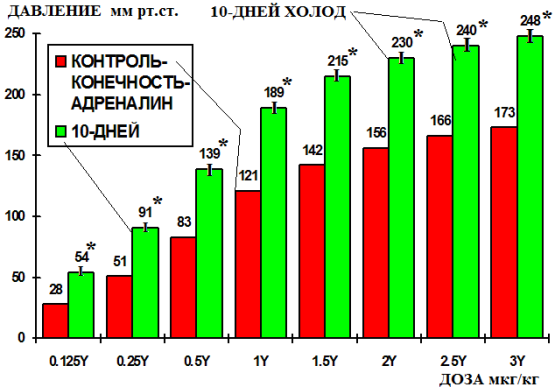

Figure 1. *Average values of the increase in the perfusion pressure of the arterial bed of the hind limb in response to adrenaline in the control group and after 10 days of cold adaptation. Abscissa: drug doses in mcg/kg (Y). Y-axis: change in perfusion pressure in mm Hg, first columns - animals of the control group, second columns - animals after exposure to cold, asterisks - significant differences to the control group (*P<0.01).*

At a dose of adrenaline 0.25 mcg/kg in the control group Pm=51 mm Hg, and after 10 days of cold Pm=91 mm Hg, which is 79% more than in the control group (at P<0.001). As can be seen from Fig. 1, subsequent doses of adrenaline 0.5 μg/kg, 1.0 μg/kg, 1.5 μg/kg, 2.0 μg/kg, 2.5 μg/kg, 3.0 μg/kg revealed the following pattern: at all these doses, perfusion pressure in animals after 10 days of cold adaptation was much higher than the corresponding perfusion pressure in animals in the control group with a high degree of significance (P<0.001). So at a dose of 0.5 μg/kg, the perfusion pressure was 67% more, 1.0 μg/kg more by 56%, 1.5 μg/kg more by 51%, at 2.0 μg/kg more by 47%, by 2.5 μg/kg more by 44%, at 3.0 mcg/kg more by 42% when compared with the control group.

To elucidate the mechanisms of changes in alpha-adrenergic reactivity of the arterial vessels of animals after a 10-day cold exposure to adrenaline and to quantify the mediator-receptor interaction, Fig. 2 shows a graph of changes in perfusion pressure in double inverse coordinates. As can be seen from Fig. 2, the straight line, reflecting the reactivity of the arteries of animals after 10 days of cooling, crosses the y-axis at 1/Pm=0.0034, which corresponds to Pm=294 mm Hg. This figure characterizes the number of active alpha-adrenergic receptors and is theoretically equal to the perfusion pressure when 100% of arterial alpha-adrenergic receptors are excited by an infinitely large dose of adrenaline.

The control group of animals is shown in Figure 2 by a straight line (N), which crosses the y-axis at 1/Pm=0.0045, which corresponds to Pm=222 mm Hg and reflects the number of active alpha-adrenergic receptors of arterial vessels in animals of the control group. Thus, the number of active alpha-adrenergic receptors after 10 days of cooling increased from Pm=222 mm Hg in control up to Pm=294 mm Hg after 10 days of cooling, that is, the number of active alpha-adrenergic receptors increased by 1.32 times or increased by 32% compared with the control group.

To characterize the sensitivity of the interaction of adrenaline with arterial alpha-adrenergic receptors, the straight line characterizing the group of animals after 10 days of cooling was extrapolated to the intersection with the abscissa axis, which made it possible to obtain the parameter 1/K=1.8 (1/μg.kg), which characterizes the sensitivity of the interaction adrenaline with alpha-adrenergic receptors. As can be seen from Fig. 2, in the control group (N) this indicator was 1/K=1.2 (1/mcg.kg). Thus, after 10 days of cold adaptation, the sensitivity of alpha-adrenergic receptors to adrenaline increased from 1/K=1.2 in control to 1/K=1.8 (mcg.kg), that is, after 10 days of cold, the sensitivity of receptors increased by 1.5 times or increased by 50%. Thus, it can be concluded that after 10 days of cooling, the sensitivity (1/K) of arterial alpha-adrenergic receptors to adrenaline increases by 1.5 times, and the number of active alpha-adrenergic receptors (Rm) increases by 1.32 times. As a result, the following changes in the perfusion pressure of the arteries of the hind limb on the introduction of increasing doses of adrenaline are

noted: for all doses of adrenaline (0.125-3.0 μg/kg), the pressor effect is significantly (P<0.001) greater in animals after 10 days of cooling (Fig. 1, 2) compared to the control group.

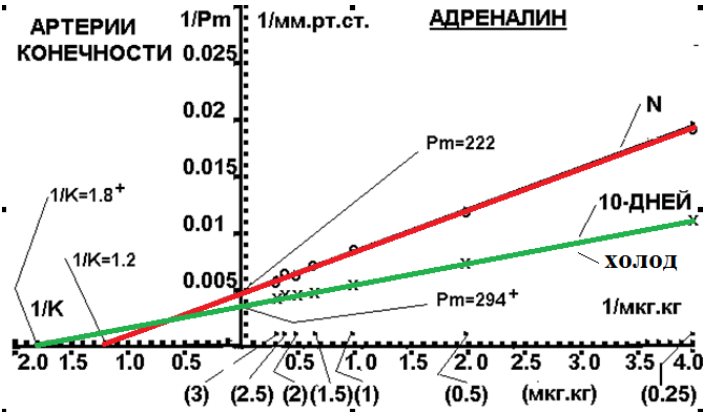

Figure 2. *An increase in the perfusion pressure of the arterial bed of the hind limb of a rabbit in response to adrenaline in double inverse coordinates in the control group (N) and after 10 days of cold adaptation. The abscissa shows the reciprocal of the dose (1/mcg.kg). The y-axis shows the reciprocal of the perfusion pressure (1/mm Hg) per 8 doses of adrenaline.*

We see the explanation for these changes in the following mechanisms of self-regulation, so when the body is exposed to cold on the 10th day of cold adaptation, low doses of adrenaline narrow the peripheral arteries more strongly, blood flow in the skin and muscles worsens, which contributes to the preservation of heat and longer survival in the cold. But this, at the same time, dramatically increases the risk of frostbite. Therefore, on the 10th day of cold adaptation, with a significant cold load (in our experiments, this is a large dose of adrenaline), the risk of frostbite increases, compared with the control group.

On fig. 3 on the abscissa axis - the value of the pressor response of the arteries to 8 doses of adrenaline (mm Hg), Pm1 - the maximum pressor response in the control, Pm2 - the maximum pressor response after the cold (mm Hg). On the y-axis, the value (Y mm Hg/DOSE) from dividing the pressure response (mm Hg) to the introduction of 8 doses of adrenaline (mcg.kg). Angles a1-tg1 and a2-tg2 reflect the sensitivity of adrenergic receptors to adrenaline in control (1/K=tg1=Y1/Pm1=266.4/222=1.2), reciprocal of sensitivity (1/K) dissociation constant of mediator-receptor (K = 0.833 mcg.kg - dose giving 50% of the effect of the maximum).

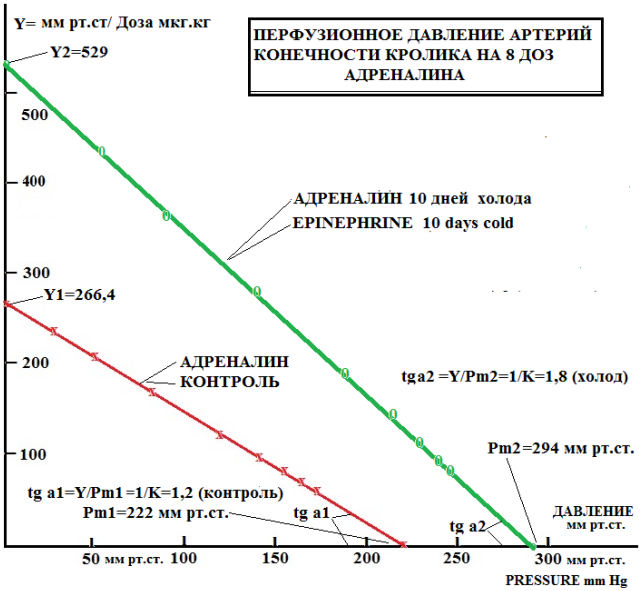

Figure 3. *Graph of changes in the pressor response of the arterial bed of the rabbit limb to 8 doses of adrenaline in the control and after 10 days of cold adaptation in the Sketchard coordinate. On the abscissa axis, the pressure is mm Hg. On the y-axis, mm Hg/mcg.kg.*

After cold (1/K=tg2=Y2/Pm2=529/294=1.8) reciprocal value of sensitivity (1/K) mediator-receptor dissociation constant (K=0.555 µg.kg – dose giving 50% of the effect of the maximum).

Conclusions. As a result of our studies, we can conclude that after 10 days of adaptation to cold, the reactivity of arterial vessels to adrenaline significantly increased due to an increase in the number of adrenoreceptors by 32% and an increase in the sensitivity of adrenoreceptors to adrenaline by 50%.

References

1. Agadzhanyan N.A., Petrova P.G. Man in the conditions of the North. - M.: <KRUK>, 1996.- 208 p.

2. Glezer, G.A. Arterial hypertension / G.A. Glezer, M.G. Glaser. - M.: Medicine, 2019. - 661 p.

3. Cornish-Bowden E. Fundamentals of enzymatic kinetics. M. Mir, 1979. 280 p.

4. Krivoshchekov S.G., Divert G.M. Principles of physiological regulation of body functions with incomplete adaptation.// Human Physiology, 2001, volume 27, M 1, p. 127 - 133

5. Anan'ev VN, Kichikulova TP, Manukhin BN. Alpha- and beta-adrenergic blood pressure response of the rabbit hind limb vessels during cold adaptation.// Dokl Biol Sci. 2000 Sep-Oct;374:448-51. PMID: 11103311

6. Blondin DP, Daoud A, Taylor T, Tingelstad HC, Bézaire V, Richard D, Carpentier AC, Taylor AW, Harper ME, Aguer C, Haman F. Four-week cold acclimation in adult humans shifts uncoupling thermogenesis from skeletal muscles to brown adipose tissue. J Physiol. 2017 Mar 15;595(6):2099-2113. doi: 10.1113/JP273395.

7. Ciuha U, Sotiridis A, Mlinar T, Royal JT, Eiken O, Mekjavic IB. Heat acclimation enhances the cold-induced vasodilation response. Eur J Appl Physiol. 2021 Nov;121(11):3005-3015. doi: 10.1007/s00421-021-04761-x. Epub 2021 Jul 10.PMID: 34245332.

8. Gordon K, Blondin DP, Friesen BJ, Tingelstad HC, Kenny GP, Haman F. Seven days of cold acclimation substantially reduces shivering intensity and increases nonshivering thermogenesis in adult humans. J Appl Physiol (1985). 2019 Jun 1;126(6):1598-1606. doi: 10.1152/japplphysiol.01133.2018. Epub 2019 Mar 21.PMID: 30896355

DOI 10.34660/INF.2023.57.38.091

REGULAR DOSED WALKING AND RUNNING IN THE NORMALIZATION OF HIGH BLOOD PRESSURE

Ananiev Vladimir Nikolaevich
Doctor of Medical Sciences, Full Professor
SSC of the Russian Federation "Institute of Biomedical Problems of the RAS", Moscow

Prokopyev Nikolay Yakovlevich
Doctor of Medical Sciences, Full Professor
Tyumen State University, Tyumen

Ananieva Olga Vasilievna
Doctor of Medical Sciences, Full Professor
Tyumen State Medical University, Tyumen

Gurtovoy Elisey Sergeevich
Student
Tyumen State Medical University, Tyumen

Abstract. *The article discusses the possibility of reducing systolic blood pressure (SBP, mmHg) in a person suffering from hypertension (H) through regular dosed physical activity in the form of running and walking. For the first time, the authors consider the mechanism of occurrence of muscle hyperemia (MH), which is manifested by a decrease in the sensitivity of alpha-1-adrenergic receptors of arterial vessels to the reducing effect of norepinephrine. It has been proven for the first time that active muscular activity in the form of running and walking for an hour in men with H contributes to a decrease, but also to the normalization of elevated SBP due to MH, not only during the day, but also for a much longer time. From a physiological point of view, this is important for restoring metabolic processes in muscles and switching on the mechanisms of adaptation of the whole organism to muscle loads. After daily regular physical activity (PA) for a month, increased SBP in men decreased from 160-170 mm. rt. Art. up to standard values. At the same time, the heart rate (HR, beats/min) did not undergo significant changes.*

Keywords: *dosed running and walking, systolic blood pressure, men, norepinephrine, muscle hyperemia.*

Relevance. From a physiological point of view, during muscle activity, arterial vessels expand due to MH, while muscle blood flow increases [1]. It would seem that the expansion of the lumen of arterial vessels in the muscle tissue should lead to a decrease in blood pressure (BP) during muscular work, but this does not happen, since the concentration of norepinephrine and adrenaline increases in the blood, which, acting on the alpha-adrenergic receptors of the arteries, reduce them, resulting in a decrease in blood flow [3]. The fact that during muscular work there is an expansion of the arteries and an increase in muscle blood flow has long been known, but why this happens has not been proven. We assumed that if MH dilates arterial vessels and if physical activity in the form of walking and running is quantitatively selected, then it is possible not only to reduce and normalize blood pressure in hypertension. When asked about the strength and duration of physical activity, only fragmentary and fragmentary studies are given [4, 5]. Regular, moderate-intensity sports activity is known to be sufficient to lower blood pressure. Forms of training recommended for this include walking, jogging, cycling, and dynamic strength training. However, the intensification of general physical activity can also lower blood pressure, regardless of other risk factors [6]. Many athletes train too intensely or too repetitively [2]. There are two ways to set the optimal training intensity: by measuring the level of lactate (lactic acid) in the blood or by using the heart rate (HR).

The oxygen, or aerobic, system is the most important for endurance athletes because it can support physical performance for a long time. The oxygen system provides muscle activity with energy through the chemical interaction of nutrients (mainly carbohydrates and fats) with oxygen. Glycogen stores can vary greatly, but in most cases they are enough for at least 60-90 minutes of submaximal intensity work. At the same time, the reserves of fats in the body are practically inexhaustible. Under the influence of training, a person's aerobic capacity can increase by 50%.

The lactate system manifests itself when muscle work can no longer be supported by the aerobic system alone due to lack of oxygen. From this point on, the lactate mechanism of ATP resynthesis, the by-product of which is lactic acid, is involved in the energy supply of physical work. With a lack of oxygen, the lactic acid formed in the first phase of the aerobic reaction is not completely neutralized in the second phase, resulting in its accumulation in the working muscles, which leads to acidosis, or "acidification" of the muscles [2].

An analysis of the scientific studies available to us showed that the load should be chosen at a low concentration of norepinephrine and lactate. Heart rate should be in the range of 90-105 times per minute at a speed of 4-6 km / h, which we used in our studies. At the very beginning of any exercise, regardless of the intensity of physical activity, the energy supply of the body occurs only in the anaerobic

way. Each time, it takes the body several minutes for the aerobic system to fully kick in - until the lungs, heart, and oxygen transport systems adjust to the demands of the load. Until then, the required energy is supplied by the lactate mechanism.

Thus, the identification of the mechanisms of MH during physical exertion in humans is not only fundamental for science, but can also help to partially solve the problem of prevention and treatment of H with a physical activity selected for a given person.

Material and research methods. The study involved 18 men (63.4±1.6 years) whose systolic blood pressure was in the range of 173±8 mm Hg., and diastolic - 120 ± 7 mm Hg. During the last two months, the men endured high blood pressure without complaints. They did not take drugs, did not smoke or drink energy drinks, did not get sick, led a healthy lifestyle, limited salt intake, had at least 8 hours of sleep at night, and had no pronounced stress factors. Prior to the study of the effect of physical activity on blood pressure, men firstly ran for 30 days daily for 60 minutes in the morning at a pace of 92-105 steps per minute. Secondly, 6000-8000 steps were taken daily in the afternoon. After that, they ran and walked for another 30 days, during this period blood pressure was measured immediately after exercise and then regularly during the day from 7 am to 12 pm. These changes in systemic pressure per day for 30 days of running and walking were statistically processed. Changes in systemic pressure were analyzed before and after running, then during the day every 2 hours. During the run, blood oxygen saturation was measured with a pulse oximeter, which was always in the range of 95% -98%, heart rate did not exceed 110 bpm. Systemic pressure was measured with an automatic tonometer UA-777.

The study was conducted in compliance with the ethical standards set forth in the Declaration of Helsinki and the Directives of the European Community (8/609EC) and the oral consent of the men.

Results of the study and their discussion. We have shown that during MH norepinephrine significantly reduces its vasoconstrictive effect on arteries in working muscles. The results of regularly measured blood pressure in men who trained for 30 days showed that before training by running at 8 am, SBP was 173.6 ± 4.1 mm. rt. Art. I would like to draw attention to the fact that after daily morning (starting at 8 am) hourly running and walking (Fig. 1) for 30 days, blood pressure in absolute values was 137.4 ± 3.8 mm. rt. Art. ($p<0.05$). Thus, it can be stated that regular dosed physical activity in the form of running and walking reduced the SBP by 36.2 mm. rt. Art.

As for the heart rate (Fig. 2), it decreased from 88.7±2.9 beats/min before the start of the study to 81.2±2.5 beats/min ($p<0.05$) after 30 days of regular exercise .

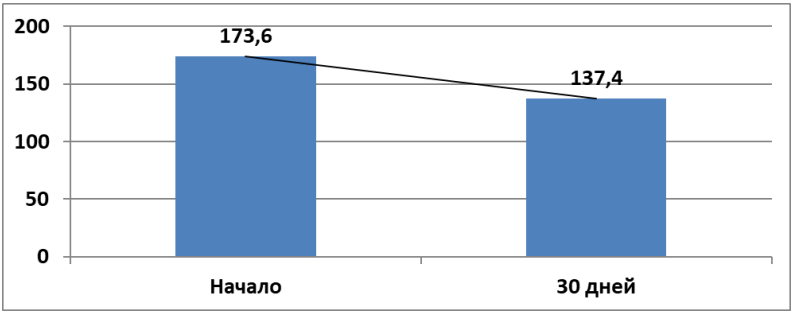

Figure 1. *The indicator of the systolic blood pressure in men after 30 days of regular jogging and walking.*

In our opinion, the decrease in systemic pressure was the result of a monthly muscle training by running and walking due to MH. At the beginning of training, up to 30 days of running, there were no such pressure reduction results. After 30 days of regular daily running and walking, systemic pressure was normal for the entire 24 hours. Based on these data, we for the first time put forward a hypothesis that after sufficient intense muscle loads, MH has a pronounced aftereffect during the day of observation.

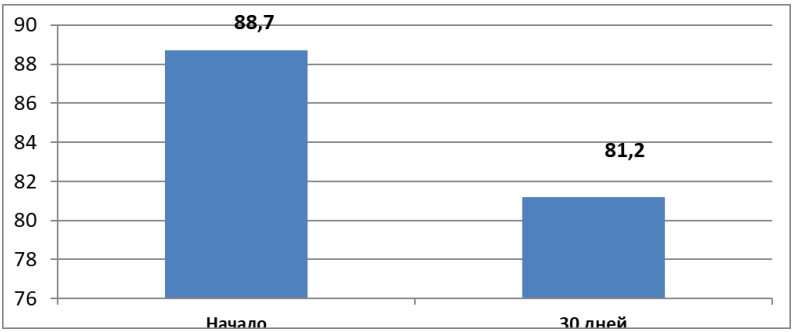

Figure 2. *Men's heart rate after 30 days of regular jogging and walking.*

The most important indicator of men's tolerance to dosed physical activity is blood oxygen saturation, which we conduct with a pulse oximeter 7 times within 30 days (Fig. 3).

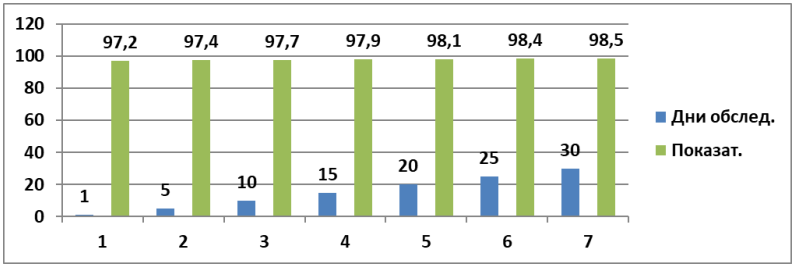

Figure 3. *Dynamics of blood oxygen saturation during 30 days of examination.*

Thus, over 30 days of regular jogging and walking with a health-improving orientation, the percentage of blood oxygen saturation in men increased by 1.3%, while starting from day 20 it steadily exceeded 98%.

Why did we take 30 days of training as a basis? It is known that only after 7-15 days the genome is activated and the synthesis of regulatory peptides begins. The men trained for 2 hours per day, one hour of running and one hour of walking.

Conclusion. The mechanism of MH is to reduce the sensitivity of arterial alpha-1-adrenergic receptors to the pressor action of norepinephrine. We have proven that muscle work in men in the form of 1 hour of running contributes to the expansion of arteries and a decrease in elevated blood pressure due to MH. At the same time, MH manifests itself during the day, i.e. has inertia and aftereffect, which is important for restoring metabolism in muscles and switching on the mechanisms of adaptation of the whole organism to muscle loads. The second muscle load in the form of one hour of walking stabilizes and improves the hypotensive result of one hour of running. We have proved that after daily physical exercises for a month, SBP reaches the age normative values.

References

1. *Arinchin N.I., Borisevich G.F. Micropumping activity of skeletal muscles during their stretching. Minsk: Science and technology, 1986. 112 p.*
2. *Jansen Peter. Heart rate, lactate and endurance training: Per. from English. - Murmansk: "Tuloma" Publishing House, 2006. 160 p.*
3. Richards J.C., Luckasen G.J., Larson D.G., Dinenno F.A. *Role of α-adrenergic vasoconstriction in regulating skeletal muscle blood flow and vascular conductance during forearm exercise in ageing humans. //*J Physiol. 2014 Nov 1; 592(21): 4775-4788. doi: 10.1113/jphysiol.2014.278358.

4. *Joyner M.J., Casey D.P.* Regulation *of increased blood flow (hyperemia) to muscles during* exercise*: a hierarchy of competing physiological //Physiol Rev. 2015 Apr; 95(2): 549-601.*

5. *Mota M.R., Pardono E., Lima L.C. Effects of treadmill* running *and resistance exercises on* lowering blood pressure *during the daily work of hypertensive subjects //J Strength Cond Res. 2009 Nov;23(8):2331-2338.*

6. *Schwarz S., Halle M.* Blood pressurelowering *through physical training-what can be achieved? //MMW Fortschr Med. 2006 Nov 23; 148 (47): 29-30, 32.*

DOI 10.34660/INF.2023.70.27.058

CRITERIA FOR CHOOSING THE SHAPE OF THE ROOT PIN TAB IN THE TEETH OF THE CHEWING GROUP BASED ON THE ANALYSIS OF THE STRESS-STRAIN STATE

Ertuvkhanov Marat Zainulabidovich
Postgraduate
Central Research Institute of Dentistry and Maxillofacial Surgery, Moscow, Russian Federation

Andreeva Svetlana Nikolaevna
Doctor of Medical Sciences, Full Professor
A.I. Yevdokimov Moscow State University of Medicine and Dentistry, Moscow c., Russian Federation

Smerdov Alexey Andreevich
Candidate of Technical Sciences, Tester
Fidesis LLC, Moscow, Russian Federation

Abstract. *The main purpose of the study was to study the influence of various shapes and materials of root pin tabs in multi-root teeth on the distribution of masticatory pressure. Calculations of the stress-strain state in the studied groups of teeth were carried out using 3-D models. In the course of the study, it was determined that the most important factor for an adequate pressure distribution is the length of the pin part of the root tab and the presence of an unloading platform. Modeling of root pin tabs with several short pins was the most unfavorable.*

Keywords: *root pin tabs, mathematical modeling and calculation of the stress-strain state of structures.*

An analysis of the structure of defects in hard tissues of teeth and data on the prevalence of caries diseases and its complications shows that the problems of restoring severely damaged teeth are still relevant. The use of dental implants cannot completely solve the issues of restoring the integrity of the dentition, in addition, the use of a natural tooth root has many advantages in terms of physiological load distribution and preservation of the natural periodontium of the teeth. As studies conducted by various authors show, in the Russian Federation, the use of root pin inlays (RPI) made of metal alloys and zirconium dioxide is a common method for restoring teeth with a destroyed crown part [1,2]. This method is widely known,

easy to use, but has its own peculiarities and difficulties [1,3]. In particular, our studies of judicial practice in dentistry in the country for the ten-year period 2013-2022. showed that in terms of the frequency of occurrence among the reasons that became the basis for the appeal of patients to the courts, RPIs are in 3rd place among fixed orthopedic structures (after metal-ceramic crowns and implant-supported crowns) [4.5]. Moreover, during the period under study, the number of claims to the quality of the manufacture of RPI did not decrease, which indirectly confirms the presence of unresolved issues and problems.

A fairly large number of publications and scientific studies are devoted to the development of optimal methods for the restoration of single-rooted teeth, and there are practically no scientific works on modeling RPI in multi-rooted teeth, and the data in these works are contradictory []. In this regard, the manufacture of RPI in chewing teeth causes certain difficulties. This is due to the peculiarities of the structure of the roots of the chewing group of teeth, with the variability in the distribution of chewing pressure with different types of inlays, etc.

The purpose of our study was to determine the optimal options for modeling RPI in masticatory teeth in the u/j and l/j, depending on the structure of the roots, by conducting a mathematical analysis of 3-D models and calculating the stress-strain state for various modeling options for RPI with one, two, three pins. In addition, options for restoring multi-rooted RPI teeth from a cobalt-chromium alloy (CCA) and from zirconium dioxide were studied.

To achieve the goal and implement the objectives of the study, using the Ansys SpaceClaim software, we created 84 tooth models (48 models with RPI from CCA and 36 RPI from zirconia). Real dental images from CBCT studies were used to create the models. Moreover, the most characteristic teeth in terms of structure were selected: 1 - with a parallel arrangement of the roots (П-shaped shape of the roots); 2 - roots with a divergence angle of more than 35° (Λ-shaped roots). The third group consisted of teeth in which the roots had a bend of more than 35° (Г-shaped roots), in the fourth group there were teeth with an O-shaped root (Figure 1).

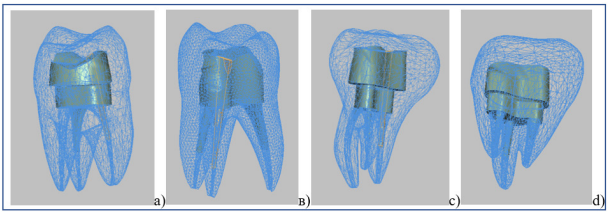

Figure 1. *3D models of teeth with different root structure: a) parallel arrangement of roots (П-shaped); b) divergence of roots more than 35° (Λ-shaped roots); c) with a bend in the area of the middle apical third more than 30° (L-shaped roots); d) roots in the form of the letter O (O-shaped roots)*

Further, for each RPI model for 4 groups of teeth, using the Ansys Workbench software, models with one, two, three CCA pins, as well as with one and two zirconia pins were created. Calculations of stress-strain states were carried out taking into account the application of a load of 100N directed along the axis of the tooth and at angles of 15°, 30° and 45°. An example of tables of values of principal stresses is shown in Figure 2.

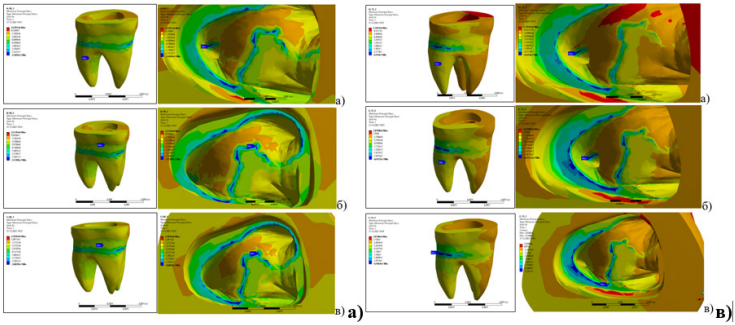

Figure 2. *The third main stresses in the tooth with one, two, three pins at the root tab (cobalt - chromium alloy) in the case of a force acting at an angle of a) 0°; c) 15°*

To verify the results of mathematical modeling in the laboratory, a study was made of the strength properties of chewing teeth restored by RPI (Figure 3).

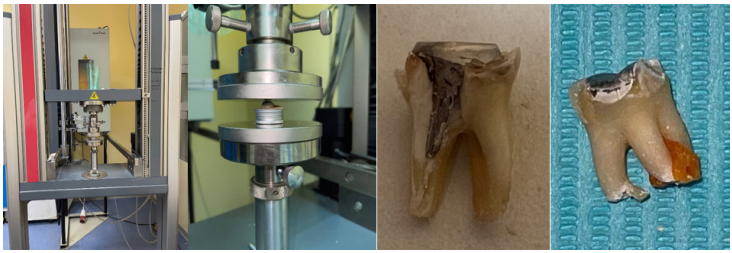

Figure 3. *Laboratory tests of the strength properties of chewing teeth restored by RPI with a different number of pin parts*

As a result of the studies conducted, data were obtained indicating that the most important factor influencing the increase in the load on the hard tissues of a multi-rooted tooth is not the shape of the roots or the number of pin parts of the inlay itself. For adequate load distribution, the length of the pin part is important, since with a long pin, the load is distributed along the length of the root and is less

concentrated at the end of the pin and in the cervical zone. In cases where it is impossible to model long pin parts of the inlay (with curved roots, canal obturation, etc.), it is preferable to model one pin and form an unloading area perpendicular to the tooth axis, because this reduces stress in the most critical areas. Studies have shown that the modeling of RPI in multi-rooted teeth with 2.3 short pins is the most unfavorable, because this reduces the possibility of creating an unloading platform, increases the load in the zone of root furcation, without allowing, at the same time, to distribute pressure over the roots of the teeth. When using zirconium dioxide (less elastic than cobalt-chromium alloy) for the manufacture of RPI, the stresses in the teeth are reduced in almost all cases.

Modern research methods, including the use of mathematical modeling, provide us with opportunities outside the human oral cavity to predict the functionality of orthopedic structures and develop the most rational treatment options.

References

1. *Markov B.P., Tsalikova N.A., Krikheli N.I., Markova G.B. Prevention of errors and complications in planning and conducting orthopedic treatment. Dental Forum. 2017;4:55-56.]*

2. *Ohanyan A.I., Apresyan S.V., Akulovich A.V. Pin structures made of zirconium dioxide used in various areas of the dentition. Russian Dental Journal. 2017;21(3):135-137.]*

3. *Andreeva S.N., Ertuvkhanov M.Z., Andreev M.M. Errors and complications in prosthetics with cast root tabs according to forensic medical examinations 2013-2022. Medico-pharmaceutical Journal Pulse. 2022. Vol.24(10):12-20.]*

4. *Andreeva S.N. Gusarov A.A., Fetisov V.A. Analysis of judicial practice in civil cases related to defects in the provision of dental care to the population of the Russian Federation for the period from 1993 to 2017. Forensic medical examination. – 2018;Vol.3(61):44-48.]*

5. *Andreeva S.N., Analysis of the features of forensic medical examinations in dentistry based on the study of judicial practice for 2013-2022. Forensic medical examination. 2023;Vol.66(1):5-8.]*

DOI 10.34660/INF.2023.50.31.059

RESEARCH AND MATHEMATICAL MODELING OF FUNCTIONING PROCESSES OF MICROBIAL BIOFUEL ELEMENTS WITH BIOTIC CATALYSTS

Arkadeva Irina Nikolaevna
Postgraduate
Vasilenko Violetta Anatolieva
Candidate of Technical Sciences, Associate Professor
Mendeleev University of Chemical Technology of Russia

Abstract. *The processes of a single-chamber cell, which is a prototype of a membraneless microbial fuel cell were studied by electrochemical methods and methods of mathematical modeling. A community of microorganisms of bacterial and fungal cultures immobilized in graphene-like thermally expanded were used as an anode catalyst; enzyme laccase immobilized on a carbon material was used as a cathodic catalyst.*

Keywords: *microbial fuel cell, laccase, glucose oxidation, oxygen reduction, bioanode, biocathode.*

One of the promising areas of modern alternative energy is biofuel cells (BFC) - devices for converting the chemical energy of a fuel into electrical energy using biological catalysts (enzymes, microbiological communities, etc.).

Microbial fuel cells (MFC) are a special case of biofuel cells. MFCs use microorganisms to extract energy from complex organic mixtures. Microorganisms are typically inoculated into the anode chamber to biocatalyze substances to produce electrons, protons, and other bacterial metabolic products. The fuel in this case can be domestic and industrial wastewater, which makes them a very attractive tool for protecting the environment. However, the large-scale application of this technology is still impossible, since an increase in the performance of the MFC is required: higher power and energy efficiency [1].

The efficiency and performance of MFCs should be studied during long-term tests close to real-time practical use (1000 h), taking into account the effects of long-term changes in biomass activity, electrode fouling, membrane plugging, metabolite accumulation and product degradation. In this regard, the development of a mathematical model of the processes occurring in the MFC can be an impor-

tant step towards scaling the technology for extracting electricity from wastewater with its associated treatment.

An important stage in the development of an efficient MFC is the selection of catalytic systems capable of providing high output characteristics for a long period of time, as well as convenient for subsequent scaling.

There are quite a lot of works on MFC designs for wastewater treatment in the literature. However, these studies are mainly devoted to the development of laboratory prototypes of MFCs. Popular designs are single-chamber, double-chamber, cylindrical. Most scaling studies have studied tubular or plate type reactors. To increase the power, individual modules are connected in series or in parallel into batteries [2-10].

This paper presents the results of modeling the phenomena occurring in a single-chamber cell, which is a prototype of a membraneless MFC [11].

Experimental studies of the phenomena of membraneless MFC glucose-oxygen with anodic and cathodic bioelectrocatalysts were carried out by the group of V.A. Bogdanovskaya at the Institute of Electrochemistry and Physical Chemistry. A.N. Frumkin Institute of Chemistry of the Russian Academy of Sciences (hereinafter referred to as IPChE RAS) by employees of the Electrocatalysis laboratory. Experiments on the cultivation of microorganisms and their immobilization on a carbon carrier were carried out at the D. Mendeleev University of Chemical Technology of Russia at the Department of Biotechnology. The results of the study of various electrocatalytic systems, both biotic and abiotic, are presented in our previously published works [11–13]. The catalytic system of the anode was a community of microorganisms of bacterial and fungal cultures, immobilized in graphene-like thermally expanded expanded graphite, the cathode was the laccase enzyme, also immobilized on carbon material (soot and carbon nanotubes).

The electrodes were tested in the developed fuel cell cell with an electrolyte chamber. During the tests, current-voltage curves were recorded, and partial curves were also measured to separate the contributions of cathodic and anode processes to the total voltage of the fuel cell. To obtain partial curves, galvanostatic current-voltage curves were measured with each point held for 1 min, and the voltage that stabilized was recorded. During the measurement of the galvanostatic curve, the displacement of the anode potential relative to the reference electrode was recorded. The sum of the cell voltage and the anode potential was used to calculate the cathode potential at each current value.

Mathematical modeling of the processes occurring in the MFC is based on the method described in [14]. The mathematical model is developed by integrating bioelectrochemical kinetics and mass and charge balances within the MFC. The simulation examines various parameters that significantly affect the performance of the MFC, and the time variation of the MFC voltage, power density and fuel

concentration is investigated using dynamic simulation. This method is relatively simple and easy to implement, which can contribute to the expansion of its practical application in the design and operation of MFCs.

It is assumed that fuel is preliminarily poured into a membraneless MFC, and oxygen is supplied from the cathode side at a certain rate.

It was assumed that glucose on the bioanode is not completely oxidized, the reaction does not go to the end, that is, not with the formation of CO_2 and protons, but with the formation of gluconic acid:

$$C_6H_{12}O_6 + H_2O \rightarrow C_6H_{12}O_7 + 2e^- + 2H^+ \quad (1)$$

At the cathode, oxygen is reduced with the participation of laccase, which is a catalyst in the bioelectrocatalysis reaction. In general, the reaction looks like:

$$\frac{1}{2}O_2 + 2H^+ + 2e^- \rightarrow 2H_2O + L \quad (2)$$

Or with laccase:

$$L + O_2 + 4H^+ + 4e^- \rightarrow 2H_2O + L \quad (3)$$

The rate of glucose oxidation at the anode can be written as the ratio:

$$r_1 = k_1\, exp\left(\frac{n_a \alpha F}{RT}\eta_a\right)\frac{C_G}{K_G + C_G}X \quad (4)$$

where C_G— glucose concentration, mol/m^3; X is the biomass concentration, mol/m^3; η_a is the overvoltage at the anode, *V;* k_1 is the reaction rate constant at the anode, mol/(m3s); K_G, Monod's constant for glucose, mol/m^3; α is the charge transfer coefficient at the anode; *F* is the Faraday constant, C/mol; *R* is the universal gas constant, J/(mol K); T is the operating temperature of the element, *K*; n is the number of electrons involved in the reaction.

We write the oxygen reduction rate at the cathode as follows:

$$r_2 = k_2\, exp\left(\frac{n_c(\beta - 1)F}{RT}\eta_c\right)\frac{C_{O_2}C_L C_{H^+}}{K_{O_2} + C_{O_2}} \quad (5)$$

Where C_L is the concentration of laccase in the active layer of the cathode, mol/m^3. C_{O2} — oxygen concentration, mol/m^3; η_c — is the overvoltage at the cathode, V; K_{O2}— is the Michaelis constant for oxygen, mol/m^3; k_2 is the reaction rate constant at the cathode, mol/(m^2 s); β - the charge transfer coefficient at the cathode.

It is assumed that the MFC is an ideal mixing reactor, in which all mass transfer processes proceed so rapidly compared to biochemical and redox reactions that the concentrations of all reagents in the solution volume can be considered equal to the concentrations on the electrode surface. Consequently, the mass balances of the main participants in the electrode processes can be represented as a system of ordinary differential equations:

The change in glucose concentration can be described using the equation:

$$V\frac{dC_G}{dt} = Qa(C^{in}{}_{CG} - C_G) - Ar_1 \quad (6)$$

The change in the concentration of protons occurs only due to reactions (2-3), can be written in abbreviated form:

$$V\frac{dC_H}{dt} = 2Ar_1 - 4Ar_2 \quad (7)$$

The equation describing the change in the concentration of microorganisms has the form:

$$V\frac{dX}{dt} = Qa(\frac{X^{in} - X}{f_x}) + AYr_1 - V_a k_{dec} X \quad (8)$$

Where V is the volume of the electrode chamber, m^3; Q_a is the volumetric flow rate of the feed solution at the anode, m^3/s; A is the electrode surface area, m^2; f_x is the percentage of microbial leaching; Y growth of active biomass; K_{dec} is the biomass decay constant, 1/s.

The equation for changing the concentration of gluconic acid, taking into account the fact that it enters the system only due to the reaction, has the form:

$$V\frac{dC_{GA}}{dt} = Ar_1 \quad (9)$$

The equation for the reduction of oxygen at the cathode:

$$V\frac{dC_{O2}}{dt} = Qc(C^{in}{}_{O2} - C_{O2}) - Ar_2 \quad (10)$$

The current density in the cell is calculated using the Faraday equation:

$$i_{cell} = F\sum_i Z_i N_M \quad (11)$$

Where i_{cell} is the current density in the cell, A/m^2; z_i is the charge number of particles.

The charge balances at the anode and cathode can be written as:

$$C_a\frac{d\eta_a}{dt} = i_{cell} - 2Fr_1 \quad (12)$$

$$C_c\frac{d\eta_c}{dt} = i_{cell} + 4Fr_2 \quad (13)$$

Where C_a and C_c – capacitances of the anode and cathode, respectively, F/m^2;

When calculating the cell voltage, we assume that the ohmic resistances arise due to the resistance of the solution. The dependence for calculating the voltage can be represented as:

$$U_{cell} = U_0 - \eta_a + \eta_c - \frac{d_{cell}}{k^{lq}} i_{cell} \quad (14)$$

Where U_{cell} – cell voltage, V; $U0$ – cell open circuit voltage, V; d_{cell} is the distance between the electrodes, m; κ_{aq} is the electrical conductivity of the solution, 1/(Ohm m).

The system of ordinary equations was solved by the difference method using the implicit Euler scheme. The scheme is absolutely stable.

The calculations were carried out taking into account the following parameters given in Table 1. Some of the parameters were obtained based on the conditions of the experiment. As a result of the calculations, the values of the reaction constants were found.

Table 1.

Parameters used in MFC simulation

Parameter	Description	Value
F, C/mol	Faraday constant	96485.4
R, J/(mol·K)	Gas constant	8.3144
T, K	Temperature	303
d_{cell}, м	Distance between electrodes (exp.)	$5 \cdot 10^{-3}$
C_a, F/m^2	Anode capacitance [14]	400
C_c, F/m^2	Cathode capacitance [14]	500
V_{lq}, m^3	The volume of the electrolyte chamber	$7 \cdot 10^{-6}$
Y, kg/kg	Bacteria growth	0.01
A_c, m^2	Cathode area	$16 \cdot 10^{-4}$
A_a, m^2	Anode area	$16 \cdot 10^{-4}$
U^0, V	Open circuit voltage:	0.526
K_{O_2}, mol/m^3	Michaelis constant for oxygen[14]	0.004
pH, dimensionless	solution pH	4,7
K_G , mol/m^3	Glucose Mono Constant	$3.68 \cdot 10^{-9}$
k_{aq}, 1/(Om·m)	Solution conductivity	$2.05 \cdot 10^{-3}$
k_1, mol/(m^2·s)	Anode reaction rate constant	$1 \cdot 10^{-8}$
k_2, mol/(m^2·s)	Cathodic reaction rate constant	$1.43 \cdot 10^{-12}$
α, dimensionless	Cathode charge transfer coefficient	0.6

β, dimensionless	Anode charge transfer coefficient	0.7
$C^0_{O_2}$, mol/m³	Oxygen concentration in the feed solution	0.3125
C^0_G, mol/m³	The concentration of glucose in the feed solution	500
C_L, mol/m³	Surface concentration of laccase	$0.468 \cdot 10^{-3}$

As a result of the calculations, the values of the reaction constants were found and the values for voltage and power were obtained. There is comparison of the calculated values with experimental data at Figures 1-2 .

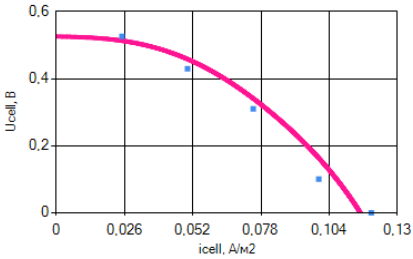

Figure 1. *Dependence of cell voltage on current density*

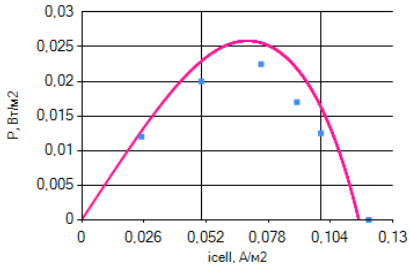

Figure 2. *Dependence of power on current density*

It can be seen from the graphs that the calculated values are close to the experimental ones. The calculation error in accordance with formula (15) was 0.389:

$$S = \sqrt{\frac{1}{N}\sum_{j=1}^{N}(i_j^{\exp} - i_j^{calc})^2} \qquad (15)$$

The dependences for the overvoltage at the anode and cathode were also obtained (Fig. 3):

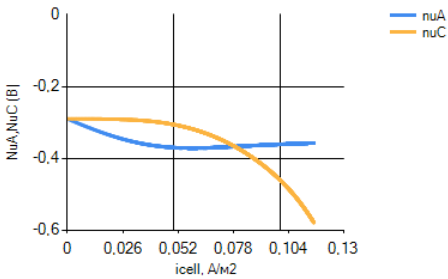

Figure 3. *Dependence of the voltage on the anode and cathode on the current density*

Graphs of changes in the concentrations of components on the anode and cathode from the values of the current density were also plotted (Fig. 4–6). The concentrations of glucose and oxygen are practically independent of the current density. Since the current density of the cell increases with time, it can be concluded that the time of the potentiodynamic tests is short enough to judge the consumption of glucose. The oxygen concentration does not change with time, since oxygen is continuously supplied to the system and the rate of its recovery is much lower than the rate of supply.

On fig. 4 there is the change in the concentration of microorganisms at the anode, their concentration slightly decreases, which is associated with the simultaneous growth and death of microorganisms.

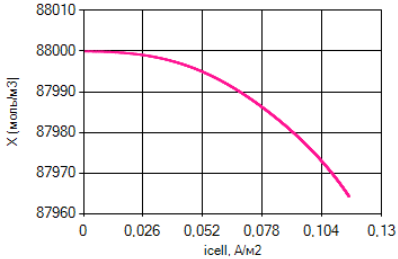

Figure 4. *Dependence of the concentration of microorganisms on the current density*

On fig. 5-6 there are graphs of changes in the concentrations of protons and gluconic acid. It can be seen that their concentration is growing due to their release as a result of the reaction at the anode.

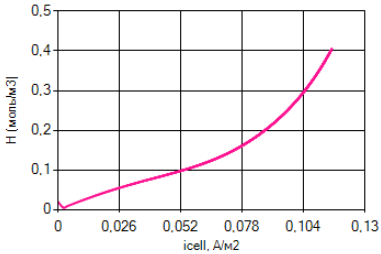

Figure 5. *Dependence of the proton concentration on the current density*

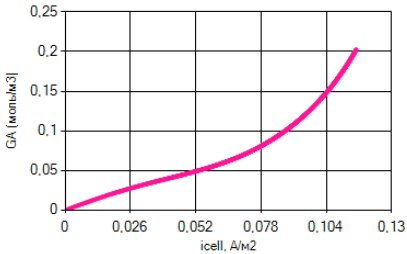

Figure 6. *Dependences of the concentration of gluconic acid on the current density*

Previously [11], we performed an optimization of the glucose concentration in the feed solution, which was approximately 0.55 M. Therefore, optimization of the glucose concentration was not performed for this biocatalytic system.

Conclusions. A mathematical model has been developed that describes the phenomena occurring in a membraneless fuel cell with biotic and abiotic electrocatalysts. When developing the model, it was assumed that the biofuel cell is an ideal mixing reactor. A software module has been developed for solving the equations of a mathematical model. The software module is implemented in the C# programming language. The parameters for solving the equations of the mathematical model are found. The output characteristics of the biofuel cell were calculated, discharge curves, profiles of changes in the concentrations of participants in the electrode processes from the values of the current density were obtained.

For a more detailed description of the behavior of microorganisms, it is necessary to separately describe the rates of their growth and death.

This study is the basis for further work on the development of efficient MBFC designs integrated with a membrane bioreactor for the treatment of a wide class of wastewater.

References

1. Fernandez M.Á., Sanromán M.Á., Marks S., Makinia J., Gonzalez del Campo A., Rodrigo M., Fernandez F. J. A grey box model of glucose fermentation and syntrophic oxidation in microbial fuel cells // Bioresource Technology. - 2016. -v. 200. - c. 396-404.

2. A. Janicek, Y. Fan & H. Liu (2014) Design of microbial fuel cells for practical application: a review and analysis of scale-up studies, Biofuels, 5:1, 79-92

3. You SJ, Zhao QL, Jiang JQ, Zhang JN. Treatment of domestic wastewater with simultaneous electricity generation in microbial fuel cell under continuous operation. Chem Biochem Eng Q 2006;20:407–12.

4. Rodrigo MA, Cañizares P, Lobato J, Paz R, Sáez C, Linares JJ. Production of electricity from the treatment of urban waste water using a microbial fuel cell. J Power Sources 2007;169:198–204.

5. Min B, Kim JR, Oh SE, Regan JM, Logan BE. Electricity generation from swine wastewater using microbial fuel cells. Water Res 2005;39:4961–8.

6. Feng YJ, He WH, Liu J, Wang X, Qu YP, Ren NQ. A horizontal plug flow and stackable pilot microbial fuel cell for municipal wastewater treatment. Bioresour Technol 2014;156:132–8.

7. Zhang, Y., Liu, M., Zhou, M., Yang, H., Liang, L., & Gu, T. (2019). Microbial fuel cell hybrid systems for wastewater treatment and bioenergy production: Synergistic effects, mechanisms and challenges. Renewable and Sustainable Energy Reviews, 103, 13–29. doi:10.1016/j.rser.2018.12.027

8. Li J, Ge Z, He Z. A fluidized bed membrane bioelectrochemical reactor for energyefficient wastewater treatment// Bioresour Technol 2014;167:310– 5.

9. Puig S, Serra M, Coma M, Balaguer MD, Colprim J. Simultaneous domestic wastewater treatment and renewable energy production using microbial fuel cells (MFCs). Water Sci Technol 2011;64:904–9.

10. Malaeb, L., Katuri, K.P., Logan, B.E., Maab, H., Nunes, S.P., Saikaly, P.E., 2013. A hybrid microbial fuel cell membrane bioreactor with a conductive ultrafiltration membrane biocathode for wastewater treatment. Environ. Sci. Technol. 47 (20), 11821–11828.

11. Arkadeva, I., Vasilenko, V., Bogdanovskaya, V., Sudarev, G., Koltsova, E. Glucose-oxygen biofuel cell based on laccase cathode and gold-modified carbon black anode: experimental research and mathematical modelling. IOP Conference Series: Earth and Environmental Science, 2021, 633(1), 012001

12. Vasilenko, V., Arkadeva, I., Bogdanovskaya, V., Sudarev G., Kalenov S., Vocciante, M., Koltsova, E. Glucose-oxygen biofuel cell with biotic and abiotic catalysts: Experimental research and mathematical modeling. Energies, 2020, 13(21), 5630

13. Koltsova, E., Bogdanovskaya, V., Vasilenko, V., Kalenov S., Korchagin, O., Fokina, E. Development of a bioanode, experimental studies and mathematical modelling of membraneless microbial fuel cell. Materials Science Forum, 2020, 995 MSF, p. 77–83

14. Zeng Y., Choo Y.F., Kim B.H., Wu P. Modelling and simulation of two-chamber microbial fuel cell // Journal of Power Sources. -2010. -m.195. -c. 79-89

DOI 10.34660/INF.2023.46.43.060

CREATING KNOWLEDGE BASES IN NATIONAL LANGUAGES OF BUSINESS PROSE WITHOUT PROGRAMMERS

Evgenev Georgy Borisovitch
Doctor of Technical Sciences, Full Professor
Bauman Moscow State Technical University

Abstract. *Software engineering is described, which ensures the creation of intelligent systems by non-programming users in various natural languages. Introduction of knowledge modules for non-programmers and generation of knowledge bases based on them. The principles of creating knowledge bases should be the "humanization" and "automation" of programming. Humanization should be based on the language of "business prose", as close as possible to the natural. The following are described: a knowledge base dictionary, combined modules with formulas, modules - tables, modules of geometric procedures, modules for selecting from a database, modules for generating 3D models, and a choice of knowledge representation language.*

Keywords: *Industry 4.0, Industry 5.0, digital production, Internet of knowledge, Internet of things, integrated systems, intelligent systems.*

Introduction

The Digital Economy project is included in the National projects of Russia for the period from 2019 to 2024. Among the goals of this project is the use of domestic software in the field of digital production, as well as the creation of end-to-end digital technologies mainly based on domestic developments. The task is to transform the industry through the introduction of digital technologies and platform solutions. This problem is relevant for other countries as well.

Conceptual model of knowledge modules

The conceptual model of knowledge modules should be based on the international standard, which is most appropriate to choose IDEF0. IDEF0 as a standard was developed in 1981 as part of the industrial automation program, which bore the designation ICAM (*Integrated Computer Aided Manufacturing*). The IDEF standards set inherited its name from this program (IDEF stands for *ICAM Definition*). In the process of practical implementation, the participants of the ICAM program faced the need to develop new methods for analyzing interaction pro-

cesses in industrial systems. At the same time, in addition to an improved set of functions for describing processes, one of the requirements for the new standard was the availability of an effective methodology for interaction within the "analyst-specialist". The standard provides group work on the creation of a model, with the direct participation of all analysts and specialists involved in the project.

Since here we are talking about intelligent systems, the most important element is the knowledge module, which is chosen as the module of the IDEF0 standard (see Fig. 1), presented in the language of "business prose".

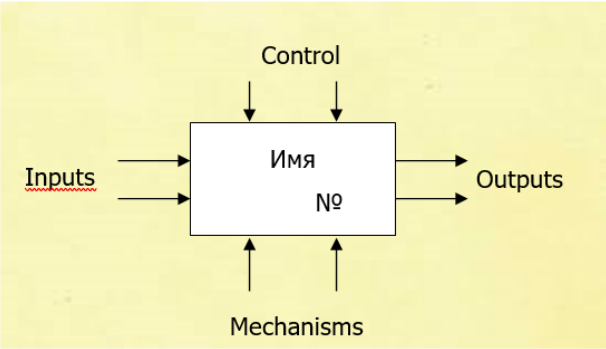

Figure 1. *External representation of the module in the IDEF0 standard*

IDEF0 is a functional modeling methodology. Its peculiarity is the emphasis on the subordination of objects. IDEF0 deals with the logical relationships between modules. The description looks like a "black box" with inputs, outputs, controls and mechanism, which is gradually detailed to the required level.

Knowledge modules in the language of business prose

In order to be properly understood, IDEF0 has dictionaries for describing activities and arrows. In these dictionaries, you can give descriptions of what meaning is attached to a particular activity or arrow.

All control signals are displayed. The model within IDEF0 is used in the organization of business processes and projects based on the modeling of all processes.

The names and names of the input, control and output variables of the MIM should be selected from the dictionary of the knowledge base (see Fig. 2).

Name	Name	type
Standard axle diameter, mm	d	R
Axle length standard, mm	L	R
Chamfer width, mm	c	R
Collar diameter, mm	D	R

	H	R
Collar width, mm	r1	R
Fillet radius, mm	r2	R
Shoulder rounding radius, mm	Grade	S
Material Grade	Mi	R
Bending moment, N*mm	Ti	R
Permissible bending stress, MPa	do	R
Initial axis diameter, mm	Lo	R
Axle length initial, mm	TO	S
Axis type	Ном	I
Detail number	dr	R

Figure 2. *Knowledge Base Dictionary*

The formation of knowledge modules (KM) is carried out using the SPRUT ExPro system [1,2]. In the module in Fig. 3, the calculation is carried out according to the formulas of a number of quantities.

Module: M1
Developer: Evgenev G. B.
Name: Calculation of axle diameter
Source of information: Anuryev V.I. Designer's Handbook, v.2, p.9

Name	Name	Limitation
Axis type	TO	smooth axle axle with collar
Bending moment, Nmm	Mi	(0.,95000)
Permissible bending stress, MPa	Ti	[0.6,0.95]
Estimated axle diameter, mm	dr	(Mi/(0.1*Ti))^(1/3)

Figure 3. *External representation of the module - formulas*

Using knowledge modules to describe formulas, you can create text variables, for example, product designations, texts for the content of technological operations, transitions, etc.

In many cases, engineering knowledge is presented in the form of tables. Fig. 4 shows a table for assigning the basic preparatory-final time for worm wheels. Tables can have multi-tiered headers and sidebars. In this case, the header specifies the replacement of devices with division by the values of the modules of the flight. The sidebar indicates the nature of the machine setup with divisions for the type of feed of worm cutters.

МЗ: "NzTpzbCh" - Назначение Тпз базового для червячных колес

Предусловия запуска

имя	наименование	тип	условие
ViZubKol$	Вид зубчатого колеса	STRING	червячное

Входные свойства

имя	наименование	тип	значение
ZamPris$	Замена приспособлений	STRING	
VidPod$	Вид подачи червячной модульной фрезы	STRING	
HarNal$	Характеристика наладки	STRING	
m_	Модуль детали, мм	REAL	

Механизм - Таблица

Конфигурация свойств в таблице

		ZamPris$
		m_
HarNal$	VidPod$	tpzb

Таблица

		с заменой установочных приспособлений			без замены установочных приспособлений		
		(0,6]	(6,12]	(12,)	(0,6]	(6,12]	(12,)
без замены фрезерного суппорта	радиальная	29	38	47	17	23	27
	тангенциальная	31	40	50	19	24	30
с заменой фрезерного суппорта	радиальная	39	52	67	27	37	42
	тангенциальная	41	56	72	29	40	52

Выходные свойства

имя	наименование	тип	значение
tpzb	Норматив подготовительно-заключительного времени базовый, мин	REAL	

Figure 4. *External representation of the module - tables*

In a system built on the basis of the SPRUT software [1,2], geometric and complex mathematical calculations cannot be represented in the form of an MK. To use mathematical knowledge, modules with mechanisms in the form of software modules have been introduced. An example of such a module is shown in fig. 5. This MK is designed to generate a drawing of the designed part. Similarly, surface and solid models of products can be generated, as well as access to software tools created outside the SPRUT environment.

Module: M8
Developer: Evgenev G. B.
Name: drawing forming
Source of information: Anuryev V.I. Designer's Handbook, v.2, p.7

Name	Name	Limitation
Axis type Standard axle diameter, mm Axle length standard, mm Chamfer width, mm	TO D L c	axis smooth (0 , 50]
Detail drawing	AXLE	AXLES.prt

Figure 5. *External representation of the module - geometric procedures*

(Limitation - the name of the program AXLES.prt; Name - the name of the graphic base segment)

Methods (complex functions) generated from elementary MK can be represented as MK and used to solve complex problems.

Mechanisms of knowledge modules. Selecting from a database

Information about the properties of materials, the parameters of standard and purchased products, as well as production resources (properties of machines, fixtures, tools, etc.) are often stored in databases. During the design process, it is necessary to select information from database tables. For these purposes, the MS of selection (selection) from databases is used.

An example of a database selection module is shown in fig. 6. In this module, the axis type is the control variable. It is necessary to select from the database the values of only those variables that define a part of this type - a smooth axis.

Module: M3

Developer: Evgenev G. B.

Name: Appointment of standard dimensions of the axis smooth

Source of information: Anuryev V.I. Designer's Handbook, v.2, p.7

Name	Name	Limitation
Axis type Estimated axle diameter, mm	TO dr	smooth axis (0, 50]
Standard axle diameter, mm Chamfer width, mm	d c	Base: STND Table: Axes Where " d ">=dr

Axes

d	D	H	r1	r2	c
5.	8.	1.5	0.4	0.6	0.6
6.	10.	2.	0.4	0.6	0.6
8.	12.	2.	0.4	0.6	0.6
10.	14.	2.5	0.6	0.6	1.
12.	16.	2.5	0.6	0.6	1.
14.	18.	3.	0.6	0.6	1.6
16.	20.	3.	0.6	0.6	1.6
18.	22.	3.	1.	0.6	1.6
20.	25.	4.	1.	1.	1.6
22.	28.	4.	1.	1.	1.6
24.	30.	4.	1.	1.	1.6
25.	32.	5.	1.	1.	1.6
28.	36.	5.	1.	1.	1.6

30.	38.	5.	1.	1.	1.6
32.	40.	6.	1.	1.6	2.5
36.	45.	6.	1.6	1.6	2.5
40.	50.	6.	1.6	1.6	2.5
45.	55.	7.	1.6	2.5	2.5

Figure 6. *External representation of the module - selection from the database*

Mechanisms of knowledge modules. Generation of 3D models

SolidWorks provides a formula engine that helps you fully define the geometry of a model, as well as specify relationships and constraints. For design engineers, this is important because the behavior of systems often relies on dynamic ratios of quantities that depend on various geometric parameters.

After creating a solid model from a sketch with dimensions, we can begin to link one global dimension to another, if necessary, to make it more dynamic and responsive to changes in the design of the part, i.e. this size becomes a function of other sizes. It is at this stage that the static part becomes intelligent (Fig. 7).

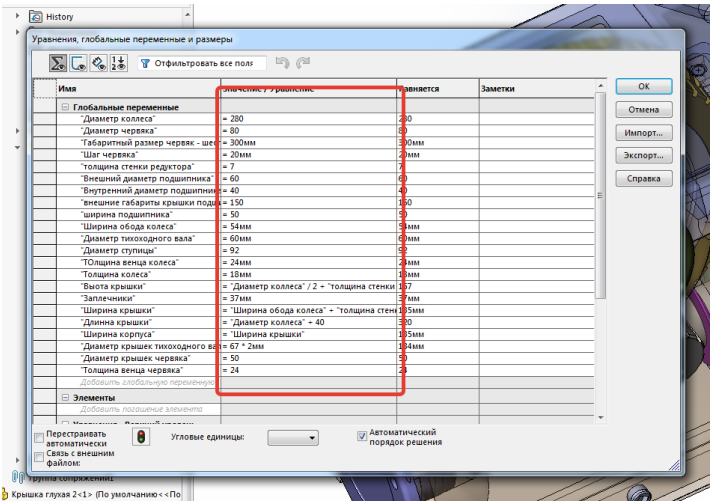

Figure 7. *Global variables binding*

There are a number of works that are devoted to the creation of intelligent CAD systems. However, they do not set the task of creating semi-automatic design systems and rapid generation of 3D models.

To provide the ability to generate 3D models using knowledge bases, it is necessary to connect the previously created knowledge method to the CAD system

using a specialized PRT module, with which, based on the model parameterized in the CAD system, a part and (or) assembly unit could be generated 3D model of a product with dimensions calculated in other modules of engineering knowledge.

If all the parameters indicated and transferred after recalculation are selected and calculated correctly, the system, after a short load, will rebuild the original worm gearbox, for example, a worm gearbox according to new requirements (Fig. 8 and Fig. 9).

Otherwise, the original 3D model will disappear and an error notification will be displayed.

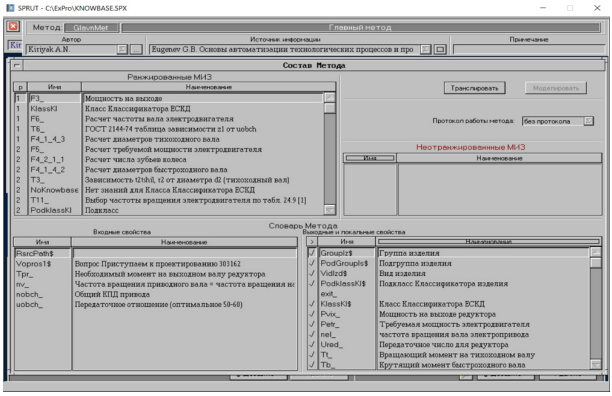

Figure 8. *Method of semi-automatic design of worm gear*

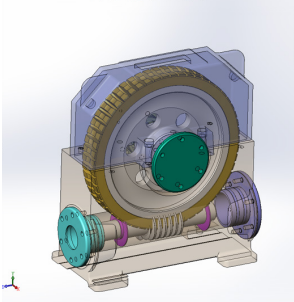

Figure 9. *Generation of a parameterized 3D model of the product*

The SPRUT system provides for the possibility of organizing cyclic processes. Cycles are generated automatically when one of the method modules appears in the output variables, which performs the function of controlling the repetition of the cycle of the selected variable with the identifier FinCalc. A method can contain

only one loop. To set loop variables, engineering knowledge modules without input variables are used, which are not included in the loop body, but are located before it.

Choice of knowledge representation language

The system has the ability to represent knowledge in various natural languages. As noted above, the names and names of input, control and output variables of knowledge modules should be selected from the dictionary of the knowledge base, which for the Russian language is shown in Fig. 2. At the same time, any natural language can be chosen as the language.

Module: V13

Developer: Evgenev G. B.

Name: Calculation of nominal deformation value

Source of information: Shuvalov S. A. Guidelines for the calculation of wave gears on a computer. Publishing house of BMSTU, 1987

Name	Name	Limitation
Reducer type Gear ratio given Number of teeth of the flexible wheel pre	ТипРед uz zf	wave single-crown (0,)
Starting torque increase factor	K1	1.9
Nominal value of radial deformation	NWo	0.84+0.001*uz+1.6*10^(-3) *K1*uz^(1/2)+0.15*10^(-3) *K1*uz
Depth of teeth admissible, mm	hd	4*NWo-(4.6-4*NWo)*zf/10^3-2.45

Figure 10. *External representation of the module with formulas in the source language*

In engineering books, functional dependencies are often represented as formulas. The external representation of the module - formulas is shown in fig. 10 in Russian.

The external representation of the same module in Hindi is shown in fig. 11.

मापांक: V13

डेवलपर : Evgenev G. B.

सूचना का एक स्रोत: Shuvalov S. A. Methodical instructions for the calculation of wave gears on a computer. Publishing house of BSTU, 1987

नाम	नाम	परसीमन
रेड्यूसर गयिर अनुपात दयिा गया	ТипРед uz	लहर एकल-मुकुट (0,)
फ्लेक्सबिल व्हील प्री के दांतों की संख्या	zf	
टाँक बढ़ाने का कारक शुरू करना	K1	1.9
मूल्यांकन मूल्य रेडयिल वरूिपण स्वीकार्य दांतों की	NWo	0.84+0.001*uz+1.6*10^(-3) *K1*uz^(1/2)+0.15*10^(-3) *K1*uz
स्वीकार्य दांतों की ग	hd	4*NWo-(4.6- 4*NWo)*zf/10^3-2.45

Figure 11. *External representation of the module with formulas in Hindi*

The methods of the created Knowledge Base can be rejected from the SPRUT-BZ system and used in various application systems.

Conclusion

The methodology and tools of software engineering with automatic programming, as well as the possibility of using various natural languages, are presented. A description of the knowledge bank and epistemological levels of knowledge representation is given. Described: knowledge base dictionary, combined modules with formulas, modules - tables, modules of geometric procedures, modules for selecting from a database, modules for generating 3D models, expert programming methodology, classification of knowledge levels, choice of knowledge representation language.

When creating modules and methods of knowledge bases, software tools for computers are automatically generated.

References

1. Evgenev, G.B. Basics of automation of technological processes and production. T.1: Information models. Vol.2: Methods of design and management – Moscow, Publishing house of MSTU named after. N.E. Bauman, 2015. – Vol. 1: – 441 p. – T.2: – 479 p. [in Russian]

2. SPRUT-Technology. Design Automation. - https://sprut.ru/. [in Russian] – http://industry5.ru/koncept. [in Russian]

DOI 10.34660/INF.2023.58.68.061
UDC 621.791.16

MODELING AND CONTROL OF THE PARAMETERS OF ULTRASONIC TRANSDUCERS FOR CONNECTING WIRE OUTPUTS

Lanin Vladimir Leonidovich
Doctor of Technical Sciences, Full Professor
Belarusian state university of informatics and radioelectronics
Minsk, Republic of Belarus

Petuhov Igor Borisovich
Candidate of Technical Sciences, chief of R&D centre
OJSC «Planar-SO» Minsk, Republic of Belarus

Abstract. *The methods of modelling and control parameters of the ultrasonic piezoelectric transducers used for wire bonding in the electronic devices are investigated. It is established, that resonance frequencies of ultrasonic transducer may be with different mechanical oscillation modes. It was found that the matching of the piezoelectric driver and the horn in the mode of longitudinal mechanical vibrations at the resonance frequency helps to achieve the maximum quality of the wire bonding. Technological tests carried out confirm this statement.*

Key words: *Piezoelectric driver, horn, ultrasonic transducer, wire bonding.*

Currently, installations for mounting wire and tape leads in electronic products use ultrasonic or thermosonic microwelding with the resonant frequency of an ultrasonic transducer (UST) in a wide frequency range - mainly from 60 to 140 kHz [1,2]. The use of ultrasonic pulsers with a resonant frequency of ≥ 100 kHz expands the technological capabilities of the lead-wire equipment, providing flexible modes of micro-welding on the contact pads of the crystals and the external leads of the package.

A modern UST for microwelding installations is a classic design consisting of a piezoelectric emitter connected to each other and a waveguide with a hole at the end for clamping a working tool (Fig. 1). The main function of the waveguide is to supply the working tool with longitudinal mechanical vibrations enhanced in amplitude from a piezoelectric emitter (piezodriver), which converts the input electrical signal into mechanical vibrations due to the inverse piezoelectric effect. On the back side of the UST there is a piezoelectric emitter based on an even num-

ber (4,6,8) of piezoelectric rings, compressed by two metal plates by means of a pin or bolt. This design converts the supplied electrical voltage of ultrasonic frequency at a certain resonant frequency (depending on the design of the UST) into mechanical vibrations of a piezoelectric emitter. Mechanical vibrations propagate along the waveguide to the attachment point of the working tool, which transmits these vibrations to the connection zone.

The parameters of a piezoelectric radiator or an UST assembly (a piezoelectric radiator with a screwed waveguide by means of a threaded stud) are usually measured by an impedance analyzer or a vector analyzer with the calculation of the values of the elements of the known equivalent circuit of the UST [3,4], its resonant frequency *Fs*, quality factor *Q* and impedance R_1 (Fig. 2).

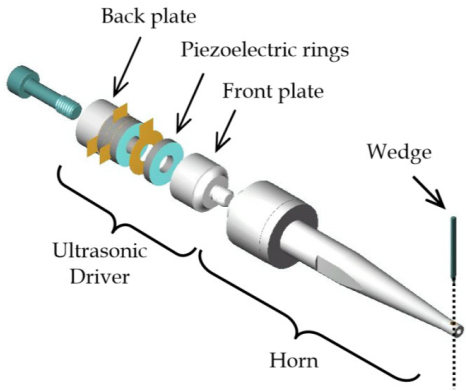

Figure 1. *Design of an ultrasonic transducer for terminal connections*

In this case, not only numerical parameters are available, but also graphical information on the behavior of the impedance, the phase shift between the applied alternating voltage to the SPD and the current flowing through it near resonance, as well as a circular diagram of admittance (similar to the Wolpert-Smith diagram). It can be seen from Fig. 2 that both USTs have almost ideal circular dependences of the total conductivity in the resonance region, which means that there are no side resonances. The graphs below the pie charts show impedance (red line) versus frequency and the phase shift between UST voltage and current (blue line). At the resonance frequency, the phase curve has a stepped character, which is widely used for phase locked loop systems. Despite the different resonant frequencies (99.6 kHz and 108.7 kHz) of the ultrasonic transducers shown in Fig. 2, they are comparable in terms of the quality factor Q_m = 579.9 for the UST in

Fig. 2a and Q_m = 514.1 in Fig. 2a. 2b and impedance 12.3 ohms (for 99.6 kHz) and 17.9 ohms (for 108.7 kHz).

It is obvious that the resonant frequency of the piezoelectric radiator must match or be as close as possible to the natural resonant frequency of the waveguide, while the resonant frequency of the SPD assembly measured by the impedance analyzer will be close to the frequency of the piezoelectric radiator. It has been experimentally established that the deviation of the resonance frequency of the assembled UST by more than 1.4 kHz from the resonance of the piezoelectric emitter leads to a deterioration in the quality of the connection.

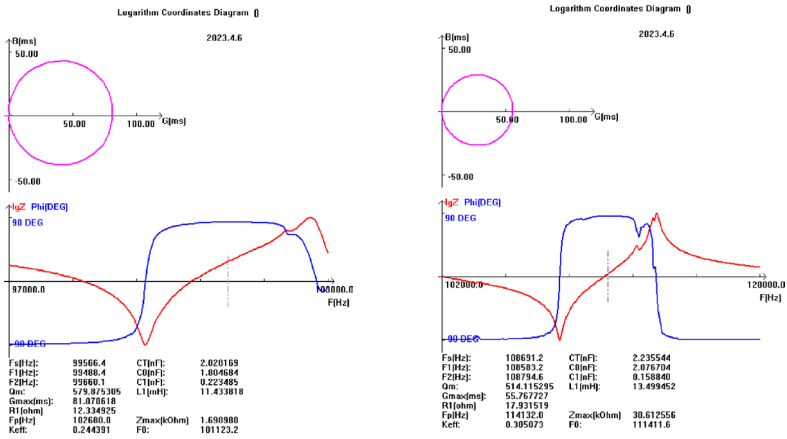

а) *б)*

Figure 2. *Electrical parameters of 2 SPDs obtained using a vector network analyzer at resonance frequencies: 99.6 kHz (a) and 108.7 kHz (b)*

To find out the reason, the modeling of waveguides designed for ultrasonic radiant resonance frequencies in the UST environment was carried out by the finite element method in the ANSYS, FEATool Multiphysics and Comsol Multiphysics packages. The simulation results show that the waveguide can have several natural resonant frequencies with different oscillation modes in the area of the working tool clamp (Fig. 3). The mode shape of the waveguide also depends on the geometry of the waveguide itself. Therefore, it is advisable in the process of designing a waveguide to carry out simulations in the above UST systems to analyze the spectrum of natural vibrations of the waveguide. Figure 3 shows a significant change in the distribution of nodes (dark blue) and antinodes (red, light green) along the waveguide axis from the point of docking with the piezoelectric emitter to the clamping point of the working tool at the end of the waveguide.

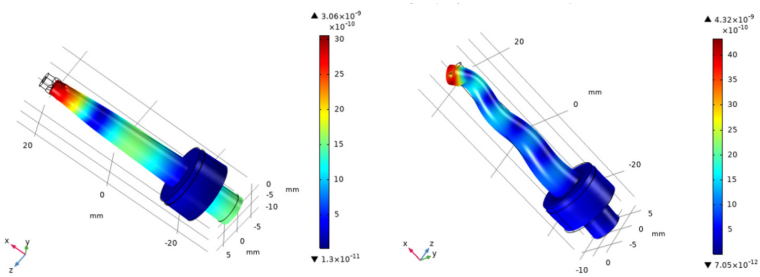

а) *б)*

Figure 3. *Longitudinal vibrations in waveguides at a calculated resonance frequency of 98 kHz (a) and bending-torsional vibrations at a frequency of 106 kHz (b)*

These negative phenomena are usually reflected in the diagram in Fig. 2 as small peaks on the impedance curve, which may signal the need for more thorough diagnostics and tuning of the assembled UST. Technological tests were carried out in the mode of assembly of semiconductor devices with aluminum wire with a diameter of 50 microns. The current strength of the leads was 21-23 g. The appearance of the wire connections is shown in Fig.4.

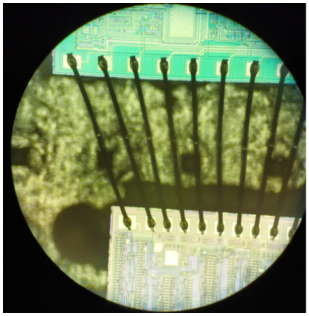

Figure 4. *Appearance of wire interconnects Al wire with a diameter of 50 microns*

In this case, a waveguide with various piezo emitters with resonant frequencies of 99.8 kHz and 104.8 kHz was used. The best results (in terms of product yield) were achieved with 99.8 kHz piezoelectric radiators.

References

1. G.G. Harmann. Wire Bonding in Microelectronics. USA, NY: McGraw Hill, 3-d edition, 2010. P. 446.

2. I.B. Petuchov. Automatic installation of wedge mounting of small-diameter wire interconnects of 2.5D electronic modules // Electronics, Science, Technology, Business, 2022, № 5. P. 66-72.

3. D.A. DeAngelis, D.C.Schalcosky. The effect of PZT8 piezoelectric cristal aging on mechanical and electrical resonances in ultrasonic transducers // IEEE Ultrasonics symposium, 2006, P.1935-1938.

4. C.Volosencu. Frequency control for ultrasonic piezoelectric transducers, based on the movement current // ICINCO, 2008, P.194-199.

DOI 10.34660/INF.2023.97.26.062

IMPOVEMENT OF THE FUEL SUPPLY SYSTEM TO THE INTERNAL COMBUSTION ENGINE BY ELECTRONIC CONTROL OF THE RING VALVE

Gabdrafikov Fanil Zakariewich
Doctor of Technical Sciences,Full Professor
Bashkirian State Agrarian University, Ufa, Russia

Abstract. *The research was carry out in order to develop a method for skipping fuel supplies (turning off individual piston strokes) at low frequencies of crankshaft rotations and at partial engine operating modes with direct-acting fuel supply systems to increase fuel efficiency. The developed method is easily implement using a ring-type discharge valve with electronic control. The fuel supply is controlee by a valve made in the form of a split elastic ring and installed in a high-pressure line above the plunger pair. An electromagnet located in the cavity of the annular valve controls it using an electronic regulator, acting at the right moment according to the signals coming from the sensors of the engine crankshaft speed, the volume of incoming air and the position of the piston. The proposed direct-acting fuel supply system with an electronically controlled ring valve reliably ensures the speed and load characteristics of the engine by affecting the number of cyclic feeds. With a decrease in the load and speed of the engine crankshaft, the number of cyclic fuel supplies decreases due to a decrease in signals to the electromagnet winding and, as a result, the valve does not attract and passes the fuel supply. Reducing the unevenness of the fuel supply by the dynamic component that occurs when the supply is switch off is ensured by reducing the inertia of the regulator due to the electronic control of the ring valve. The developed mathematical model of a direct-acting fuel supply system with an annular discharge valve allows us to reveal the relation-ship of fuel supply parameters with the design dimensions of the split ring. Such a direct-acting fuel supply sys-tem with an electronically controlled discharge valve allows, due to the skipping of working strokes in low-load and idle modes, redistributing the provided amount of fuel to the working cylinders, significantly reduce fuel consumption.*

1 Introduction

Agricultural production is one of the main sectors of the country's economy, which constantly needs to attract mobile energy resources to perform technological processes in crop production and animal husbandry. The most promising way to ensure the efficiency of the use of technical means in the agro-industrial complex is the modernization of the fuel supply system of the internal combustion engine [1].

Fuel supply systems of direct action of diesel engines have proven themselves well throughout the entire period of long-term operation. Their wide distribution became possible thanks to the modified design of all elements of the system, unification, maintainability and unpretentiousness.

They work most effectively in modes close to nominal [2]. A study of tractor and combine diesels in operation has shown that most of the time in the balance is occupy by work that requires only a partial load on the engine [3]. Similar results were show by our earlier observations in conditions of a very high culture of equipment operation in the Berthold farm (Bavaria, Germany).

With a decrease in the load on the engine and the transition to low rotational speeds of its crankshaft and at idle, the efficiency of the fuel supply system deteriorates significantly due to a decrease in the value of the cyclic supply and an increase in its irregularities between sections and between cycles [4].

One of the options for preventing a decrease in the cyclic supply and the efficiency of diesel at partial loads is the method of turning off the cylinders [5]. This method proved itself when idling the engines D-108, D-160 and D-180 of the Chelyabinsk Tractor Plant and A-01M of the Altai Engine Plant.

The positive effect of turning off the cylinders was obtain on the eight-cylinder engine of the Kamaz-740 car [6]. The disconnection of a part of the cylinders was carry out by connecting the high-pressure pump discharge line with the low-pressure line using a controlled electromagnetic valve in the fuel supply system.

Research is underway to turn off the cylinders of tractor and automobile diesels with simultaneous action on the valves of the gas distribution mechanism in partial load modes [7] to reduce losses on the piston pumping strokes in the suction and compression cycles. A reduction in the hourly fuel consumption of diesel up to 38% was find when some of the cylinders were switch off in low-load modes [8].

The company "MTU" (Germany) has modernized diesel engines 12V956TB, introducing the technology of sequential shutdown of cylinders [9].

The method of disconnecting cylinders on an engine operating on a Miller cycle with an adjustable suction stroke through the control of the valve lift of the gas distribution mechanism was developed by Tula Technology [10]. Studies have shown the possibility of reducing engine fuel consumption by 23%.

The cylinder shut-off method is widely used on gasoline engines of passenger cars. Mercedes used the Active Cylinder Control (ACC) system to automatically

turn off half of the cylinders on eight and twelve cylinder engines on its 500- and 600-series cars. The Multi-Displacement System (MDS) is use on Jeep, Dodge and Chrysler vehicles. General Motors has also implemented a Displacement on Demand (DoD) system on its cars. Honda has developed a Variable Cylinder Management (VCM) system. Since 2012, Volkswagen has been using a similar system called Active Cylinder Technology (ACT), but already on four-cylinder TSI engines with a volume of 1.4 litters. Audi also supplied its powerful V8 and V12 engines first, and then four-cylinder 1.4-liter engines with the COD (cylinder on demand) system.

The common disadvantages of the cylinder shutdown method on various engines is an increase in the required starting speed and the uneven rotation of their crankshaft.

The purpose of the scientific work is to study the method of skipping fuel supplies when operating a diesel engine at low loads with an electronically controlled ring valve and a mathematical description of its functioning.

2 Conditions, materials and methods of research

We have conducted research on the development of a method for skipping the fuel supply by alternating in all cylinders when operating a diesel engine with a partial load. This method will reduce the impact of the disadvantages of the cylinder shutdown method on engine operation.

Preliminary calculations carried out for the D-240 four-cylinder tractor diesel engine showed that a consistent increase in the number of disconnected cylinders leads to an increase in the unevenness of rotation of its crankshaft and the conditional values of the starting revolutions of the ns. The calculation data are given in table 1.

From the data in the table, it can be seen that the values of δ are greater than the values of unevenness recommended for tractor diesels - 0.004...0.010, but slightly. To reduce δ to 0.01, it is necessary to start the engine when working on all cylinders or increase the moment of inertia of the flywheel.

Reducing the inertia of its mechanical regulator is essential for improving the quality of fuel supply. Electromechanical regulators with annular discharge valves, which can ensure the passage of fuel supplies, have shown themselves well in improving the quality of fuel supply in any modes [11].

The annular discharge valve is install above the plunger pair of the high-pressure pump as shown in Figure 1.

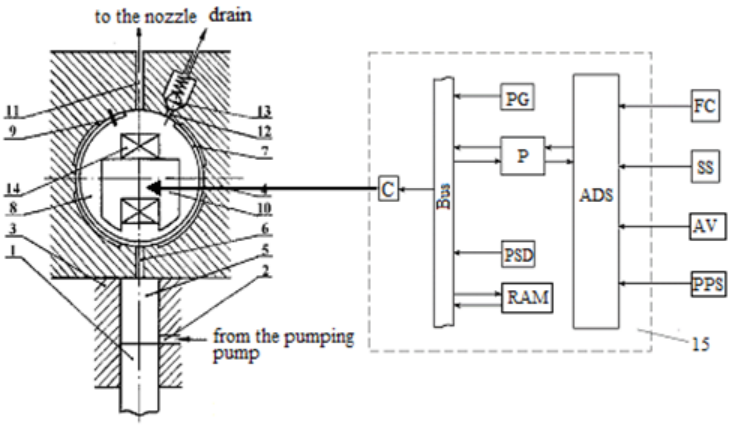

Figure 1. *Diagram of an electromechanical regulator with an annular discharge valve:1- plunger; 2, 6, 11, 12 - channels; 3 - sleeve; 4 - valve body; 5, 8 - cavities; 7 - split ring; 9 - pin; 10 - electromagnet; 13 - drain valve; 14 - electromagnet coil; 15 - electronic regulator; PSD - permanent storage device; PG - pulse generator; ADC - analog to digital converter; P – processor; RAM - random access memory; C- switchboard; PPS- piston position sensor; AV- incoming air volume sensor; SS -engine crankshaft speed sensor; FC - fuel supply control lever.*

A split ring 7 is built into the valve body 1, fixed on one side with a pin 9. An electromagnet 10 with a coil 14 is install in the valve cavity 8. The free side of the ring is capable of blocking the drain channel 12.

To supply fuel to the cylinder through the nozzle, the plunger 1 of the pump pumps fuel through the discharge valve by lifting the split ring 7, while the electromagnet 10 additionally attracts the ring, which covers the drain channel 12 with a free edge.

When the electromagnet is de-energized, the split ring is lower and the drain channel 12 opens. The high-pressure line connects to the drain and fuel injection into the cylinder stops. The residual fuel pressure in the high-pressure line is provide by the drain valve 13.

Thanks to the electronic regulator 15, the annular discharge valve can adjust the fuel injection advance angle and the feed duration (the value of the cyclic feed), determined by the moment and duration of the control pulse to the electromagnet.

The timely supply of a pulse to the electromagnet is provide in accordance with the data received from the sensors of the piston position, the volume of incoming air, the rotational speed of the engine crankshaft and the fuel supply control lever.

To skip the supply, when the plunger is inject with fuel, the control pulse is not apply to the electromagnet and the fuel sent directly to the drain. The elasticity of the ring is calculate so that the height of its lifting and the movement of the free edge from the fuel pressure is not enough to close the drain channel 12.

Thus, an annular discharge valve with an electromagnet can regulate the operating modes of a diesel engine by passing fuel supplies depending on the load. When the load decreases, it is not the amount of cyclic feeds that decreases, but the number of missed feeds increases. In this case, the value of the cyclic feed will be equal to the nominal value. This will have a positive effect on the quality of fuel spraying, mixing and combustion. In this connection, it is expect to increase the efficiency of the engine.

3 Results of the study

A mathematical model of an electrically controlled fuel supply system with an annular discharge valve has been develop, taking into account the peculiarities of its operation, based on the use of the method of hydrodynamic calculation of existing direct-acting fuel supply systems.

The movement of fuel in the high-pressure nozzle was consider taking into account the pressure of waves coming towards at the speed of sound. The fuel flow rates in the injection and control channels were determined based on the continuity equation of the fluid flow.

To describe the ongoing process in a high-pressure pump, the equations of the volume of liquid (fuel) and the dynamic equilibrium of a ring-type discharge valve were use:

$$6 \cdot n_н \cdot \beta_a \cdot V_a \cdot \frac{dp_a}{d\phi} = \left(f_n \cdot s_p - \sigma_{iv} \cdot Q_o - \sigma_{vc} \cdot Q_1 - Q_3 - Q_4\right). \quad (1)$$

$$6 \cdot n_n \cdot \beta_{vc} \cdot V_{vc} \cdot \frac{dp_s}{d\phi} = \left(\sigma_{vc} \cdot Q_1 - \sigma_{cc} \cdot Q_2 - f_{hp} \cdot s_{ci}\right) \cdot \sigma_2 \quad (2)$$

$$\frac{dV_{fv}}{d\phi} = -\left(\sigma_{vc} \cdot Q_1 - \sigma_{cc} \cdot Q_2 - f_{hp} \cdot s_{ci}\right) \cdot \frac{\sigma_3}{6 \cdot n_n}. \quad (3)$$

$$6 \cdot M_k \cdot n_n \frac{ds_{vc}}{d\phi} = ((f_i \cdot (p_a - p_s) + \quad (5)$$

$$+ f_i \cdot \rho_f \cdot s_p \cdot (s_p - s_{ci}) - p_{rp} \cdot b \cdot D - f_i \cdot p_s \cdot \sigma_c)\sigma_{vc};$$

where p_a, p_s - the pressure of the supplied fuel in the cavities above the plunger and in the suction channel, Pa;

f_{cc}, f_i, f_{hp} - the cross–sectional areas of the control channels, injection and high pressure lines, mm^2;

s_p - the speed of the plunger, m/s;

s_{ci}, s_{cc}, s_{vc} - the fuel feed rates in the channels injection, control and in the valve cavity, m/s;

V_a, V_{vc}, V_{fv} – volume in the cavities above the plunger, in the valve cavity and free volume, m^3;

ρ_f – the density of the supplied fuel, kg / m^3;

Q_0, Q_1, Q_2, Q_3, Q_4- fuel consumption in the system of equations in the intake channel, in the discharge channel, in the control channel, through the plunger gaps in the spool part and in the piston part, kg/s;

M_k – weight of the ring with a cut, kg;

n_n and φ - the rotational speed (min^{-1}), and the angle of rotation (degree) of the cam shaft of the pump;

σ_{iw}, σ_{vc}, σ_{cc}, σ_2, σ_3, σ_c- the logical elements;

h_{rr} -the rise of the split ring, mm;

p_{rp} - the radial pressure of the ring, Pa;

b and D - the width and diameter of the ring, mm;

β_a, β_{vc} - the compressibility coefficient of fuel in the cavities above the plunger and in the valve cavity.

Formula (1) is the balance of the fuel volume in the cavity above the plunger. The following (2) and (3) equations are the balance of the fuel volume in the valve cavity. If there is no gap, the expression (2) is use for calculation, if there is a gap – (3).

The amount of fuel entering the cavity per unit of time with the ring valve raised in equation (2) is equal to the flow through the discharge channel, with the excep-tion of fuel in the control channel and in the discharge pipe. When the control voltage is applied to the electro-magnet, the step function $\sigma_{cc} = 0$. Equation (3) (it's left part) describes the volume changes (V_{fv}) per unit of time in the cavity (V_{vc}) of the ring. At the same time, the right part of this equation demonstrates an increase in the volume of fuel in the cavity of the V_{vc}, which leads to a decrease in the free volume of the V_{fv}.

The dynamic equilibrium of the annular discharge valve is describe by formulas (4) and (5). In equation (4) (left part) is the inertia force of the split valve ring, and the sum of the fuel pressure forces and the valve force in the right part.

The following logical elements were take into ac-count: with pa≥ piw was taken σ_{iw}=1; with $p_a \leq p_{iw}$ was taken σ_{iw} = -1; when the intake window was open, σ_{iw} = 0 was taken; when the ring was pressed against the body, σ_c=1 was taken; in other cases, σ_c =0; with $p_a \geq p_s$, σ_{vc} =1 was taken; with $p_a \leq p_s$, σ_{vc} = -1 was taken.

The order of use in the calculation of equations (2) and (3) is determined by the logical elements σ_2 and σ_3: so for $V_{vc} \geq 0$ and p_{vc}=0 was taken σ_2=0 and σ_3=1; for p_{vc}>0 and V_{vc}=0 was taken σ_2=1 and σ_3=0.

Injection pressure and fuel consumption are deter-mine by the following expressions:

$$p_{\Phi}^{1} = \frac{(\mu f)_p^2}{(\mu_s \cdot f_h)^2} \cdot (p_f - p_g) + p_g \,, \qquad (6)$$

$$Q_n = \mu_p \cdot f_h \cdot \sqrt{\frac{2}{\rho_f}} \cdot \sqrt{p_n - p_g}, \qquad (7)$$

where $(\mu f)_p$ - the effective section of the atomizer, mm^2;

μ_p, μ_s - the fuel consumption coefficients in the plunger sections and spray holes;

p_g - the gas pressure in the cylinder, Pa;

p_f - the fuel pressure in front of the needle cone, Pa;

f_h - the cross-sectional area of the spray holes, mm².

For the calculation, the fuel injection process was di-vide into a number of stages, from the beginning of the plunger movement and the lifting of the annular dis-charge valve to the landing of the nozzle needle cone on the locking belt (completion of injection).

Calculations carried out using these equations made it possible to clarify the design dimensions of the devel-oped fuel supply system with an electronically controlled annular discharge valve, in particular, the parameters determining the stiffness of the ring and the volume of the valve cavity - diameter (*D*), width (*b*) and thickness (*t*) of the split ring.

The adequacy of the developed mathematical mod-el was check by comparing the calculated data with the experimental results. Previously, the design dimensions of the annular discharge valve were assumed to be equal to *D*=20 mm, *b*=10 mm, *t*= 0.5 mm. The rotational speed of the camshaft of the fuel injection pump with a dimension of 1TN-9X10 is assumed to be n_n = 600 min^{-1}, the pressure at the nozzle P_0 = 1.0 MPa with full cyclic fuel supply with the FD-22 nozzle.

Table 2 shows the calculated (C) and experimental (E) fuel pressure values at the nozzle and the values of the cyclic fuel supply.

Table 2.

Calculated and experimental pressure values at the nozzle fitting and cyclic fuel supply

Indicate		**Angle of rotation of the crankshaft, degree**								
		4	**6**	**8**	**10**	**12**	**14**	**16**	**18**	**20**
Pressure at the nozzle fitting, MPa	**C**	0	25	45	50	52	53	20	0	0
	E	0	23	46	48	50	54	18	0	0
Cyclic fuel consumption, g/cycle	**C**	0	4.2	6.2	6.3	6.3	6.4	6.5	3	0
	E	0	5.1	6.0	6.2	6.3	6.4	6.5	3.2	0

A comparative analysis of the calculated and experimental data revealed that the deviation is no more than 3%, which confirms the adequacy of the mathematical model.

Fig. 2 shows the results of a study of the main performance indicators of the D-240 diesel engine from the number of cylinders operating simultaneously, i.e. when one, two and three cylinders are switch off, respectively. Experiments have shown that when the cylinders are switch off, the unevenness between the fuel supply sections also changes.

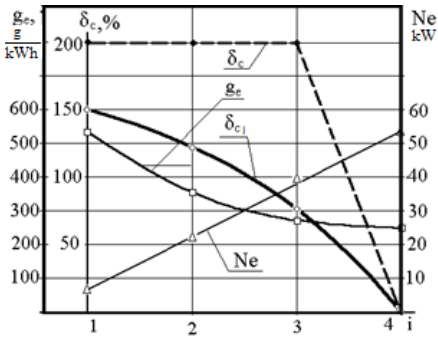

Figure 2. *Dependences of specific effective fuel consumption (g_e), power (N_e) and unevenness between sections (δ_c) of diesel D-240 on the number of working cylinders (i).*

It is prove that the unevenness increases as the number of disconnected cylinders increases. The specific effective fuel consumption increases significantly and the effective power decreases (fig. 2).

Turning off the cylinders significantly affects the minimum-stable engine crankshaft speed. So when working on four cylinders, it was 750 min^{-1}, on one – 700 min^{-1}.

Disconnecting one of the two cylinders of the D-21A engine at an effective power of N_e = 3 kW ensured a reduction in specific fuel consumption from 700 to 420 g/kWh.

The calculated and experimental data obtained allow us to establish the possibility of regulating the engine crankshaft speed by passing fuel supplies depending on the load. For example, reducing the load by 1% makes it possible to skip every hundredth working stroke, by 10% – every tenth, by 20% – every fifth, etc. Such regulation makes it possible to inject the full fuel rate in each operating cycle, and therefore, as the load decreases, the specific fuel consumption will decrease, and the load characteristic itself will change smoothly.

Thus, turning off the cylinders, or even better, skipping the working strokes (fuel supply) as the load decreases is an effective way to increase the fuel efficiency of diesels.

4 Conclusion

• a direct-acting fuel supply system with an electronically controlled annular discharge valve ensures reliable regulation of the engine shaft rotation speed by passing fuel supplies while reducing the load;

• the develop mathematical model of the fuel supply system with an electronically controlled ring valve allows you to establish the relationship and perform calculations of the design parameters of the fuel supply system (switching off the working strokes of the pistons) of the engine;

• the effect of the proposed fuel supply system with an electronically controlled injection ring valve is manifested in an increase in the fuel efficiency of a diesel engine, especially in partial load and idle modes. So the diesel D-21A specific consumption decreased from 700 to 420 g/kW·h in the Ne = 3 kW mode.

References

1. *I.V. Astakhov, L.N. Golubkov, V.I. Trusov et al. Fuel systems and efficiency of diesels (Mashinostroenie, 1990)*
2. *F.Z. Gabdrafikov, S.B. Shamukaev, Mechanization and electrification of agriculture, 9, 22 (2010)*
3. *L.V. Grekhov, N.A. Ivashchenko, V.A. Markov, Fuel equipment and diesel control systems: textbook for students of higher educational institutions (Legion-Avtodata, 2005)*
4. *Dexing Qian, Ridong Liao, Jianhua Xiang, Baigang Sun and Shangyong Wang, ASME, 1256 (2016)*
5. *D.H. Valeev, V.A. Gergenreder, I.Y. Olesov, Engine building, 8, 62 (1991)*
6. *A.N. Gots, V.F. Guskov Lecture Notes in Mechanical Engineering, 787 (2021)*
7. *A.V. Gritsenko, K.V. A.A. Glemba, Engineering Sciences, 33(1), 70 (2021)*
8. *Wenfu Sun, Xiaoqin Mo. IOP Conf. Series, 381, 012065 (2018).*
9. *E. Ortiz-Soto, X. Yang, Ess Van, A. Joshi et al., Technology SAE Technical Papers (2021)*
10. *X. Zhu, S. Limbu, K. Cung, W. De Ojeda et al., SAE Technical Paper , 0855 (2016)*
11. *R.M. Bashirov, R.R. Galiullin, A.A. Ilyin, F.Z. Gabdrafikov, Patent for invention RU 2258823 (2005)*

DOI 10.34660/INF.2023.10.65.063

APPLICATION OF THE LUCKGRIB WEATHER ROUTING SYSTEM FOR WEATHER NAVIGATION

Astreina Lyudmila Borisovna
Candidate of Geographical Sciences, Associate professor
Admiral F.F. Ushakov Maritime State University

Shtyrkhunova Natalya Aleksandrovna
Candidate of Philological Sciences, Associate Professor
Admiral F.F. Ushakov Maritime State University

Pershina Larisa Aleksandrovna
Senior Lecturer
Admiral F.F. Ushakov Maritime State University

Abstract. *The present paper reviews and analyzes the weather routing system in the LuckGrib application. The Weather Routing system is capable of generating optimized paths through weather systems from one point of a ship's route to another. These paths take into account the ship performance and comfort preferences creating actual routes through weather systems. The examples given below, their consideration and all related tools will help explore the possibilities of weather navigation.*

Keywords: *Weather Routing system, LuckGrib, actual routes through weather systems.*

Introduction

Weather systems can be complex. They are constantly changing because the wind changes in strength and direction over time. Based on the general approaches to solving optimization problems presented in [1], it is possible to consider the process of finding optimal routes in various ways as it might be difficult to decide how to navigate in a complex weather system. The decisions having made at the beginning of a voyage can later lead to the worst results due to the incompetence of navigators or ignoring seemingly hidden changes in the weather.

Simply stated, the Weather Routing system is capable of generating the optimized paths through weather systems from one point in a ship's route to another. These paths take into account the ship performance and comfort preferences, creating realistic routes through weather systems [2].

The examples given below, their explanations and all related tools will help you explore the possibilities of weather navigation.

One of the guiding principles to be taken into account in this activity is that captains and navigators don't like to be told what to do. For example, it is not of full use to receive guidance from the system representing a path to be followed without understanding the decisions that are part of that path.

LuckGrib Weather routing systems

The purpose of the LuckGrib weather routing system is to improve the understanding of the capabilities of weather systems. This is not just to indicate the path to be followed but also to use weather routing for better understanding of the evolution of weather systems.

There are tools in the LuckGrib enabling to improve the understanding of the environmental conditions by means of various ways. The LuckGrib is advanced system that allows to explore weather systems – Figure 1[3].

The LuckGrib weather routing system is a modern implementation of a concept existing for decades. It solves the routing problem on your device [3].

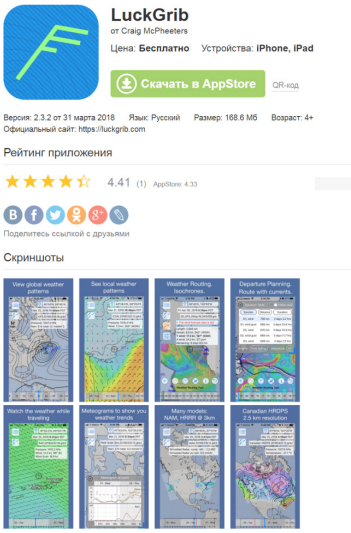

Figure 1. *LuckGrib application (download page) [3]*

Those familiar with the LuckGrib application know that this weather routing system has been designed to be the most intuitive understandable, flexible, accurate, powerful and high-performance system.

It is suggested to consider the passage of a ship in the Pacific Ocean.

The weather forecast loaded shows the following conditions (Figure 2):

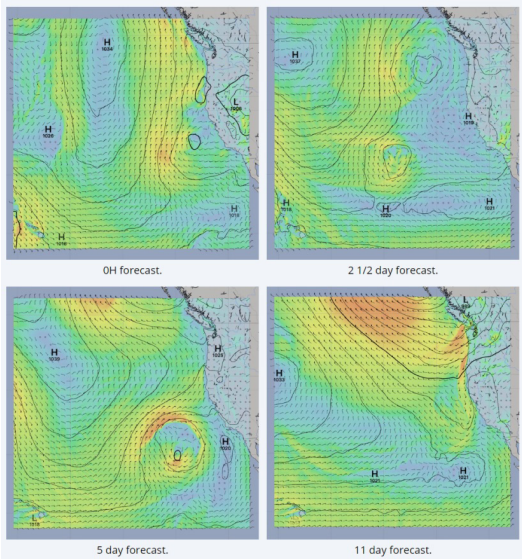

Figure 2. *Weather forecasts [3]*

There are two obvious options available.

The first option: a direct route between Hawaii and Neah Bay. It is the shortest distance but, in this route, the weather conditions prevailing in the forecast are ignored.

Another option is to follow the rule of thumb which means in this case that a ship will head north until it is at the latitude of Neah Bay and afterwards turn to east.

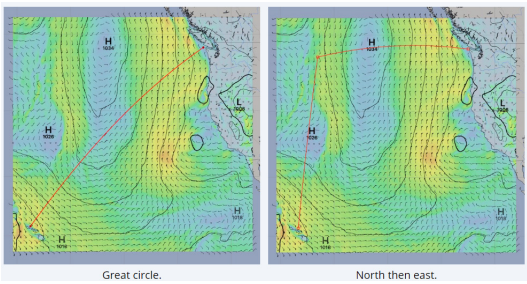

Figure 3. *Route Options [3]*

None of these routes are optimized for the weather forecast at the time of the passage. However, the LuckGrib weather routing system can be used to create an optimized path through this weather system from Hawaii to Neah Bay:

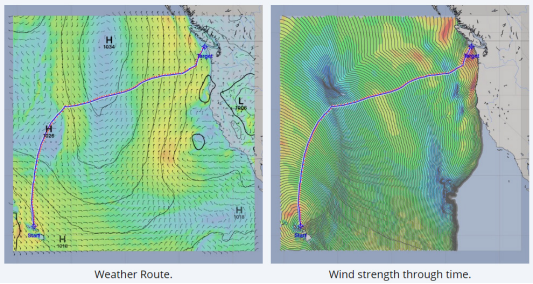

Figure 4. *Optimized route [3]*

It is necessary to note that the generated weather path usually uses a rule of thumb, however, the system has been able to determine that the forecast suggests a favourable approach to Neah Bay from the south-west due to the west-westerly winds prevailing at the time the ship approaches this area. Surely, if we were to follow this route, we would be updating our weather forecasts at least every day, and by the time of approaching the point where it is required to take a decision about the turn to east, we would have up-to-date data for taking such a decision.

Wind vectors are displayed along the generated route, making it easy to see the predicted wind directions.

On the right in Figure 4 there is an analytic image having the full solution space generated by the weather forecasting system, which is used to display the true wind speeds for all possible positions where a ship might be after leaving Hawaii.

The colour at each position on the analytic image is determined by converting the GRIB time to the time when the ship will be on the route, where wind conditions are estimated based on wind strength. The image shows the weather system conditions on your ship when it will be navigating the route.

While considering the wind speed analysis on the right, we can see the favourable wind speeds prevailing when leaving Hawaii, with a short period of high winds (orange, ~27 knots) some time after departure. Then the wind subsides. The blue spot indicates a light wind, about 7 knots in this case. This corresponds to the proximity to the centre of the high-pressure zone. After a short break the winds return and are favourable until the end of the passage.

There is another example where we can see the weather routing with significant surface currents – Figure 5.

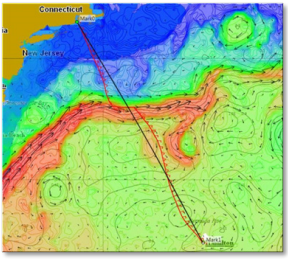

Figure 5. *Route optimization against the background of significant surface currents*

The isochrone method on the basis of which routes are built

Isochrones are lines connecting the points of simultaneity of any phenomenon or event. In our case the question is: if the ship is at the point of departure where can it be, for example, in an hour? In order to solve this initial problem, the system will evaluate the wind forecast at a given point and time, and then plot routes in all directions from the starting point. As the ship has a heading it is possible to calculate the heading wind angle – Figure 5.

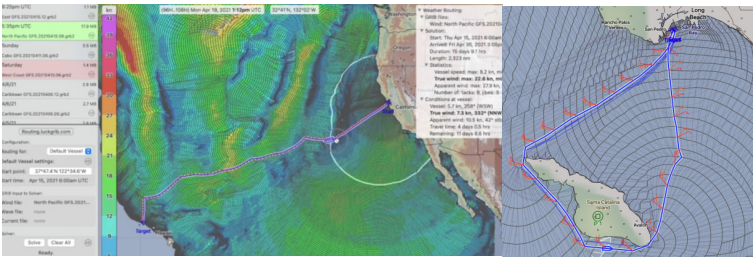

Figure 5. *Isochrones and outer zone [5]*

This is the first isochrone in weather routing solution. The ship from the starting point can be at any of the points on this outer line after an hour. The outer line is an isochrone, connecting the points and showing where you might be after one hour of travel. Thus, isochrones are the optimal solutions (but not the only ones).

It should be noted that although the isochrones represent optimal solutions, they cannot be declared as the only optimal solution. Most likely, there will be alternatives that can appear at about the same time.

The following process has to be taken at least every day:

– load the latest (updated) weather data;
– run the solver without a target point;

– study the space of solutions;
– choose an intermediate target point;
– restart the solver to generate a new path.

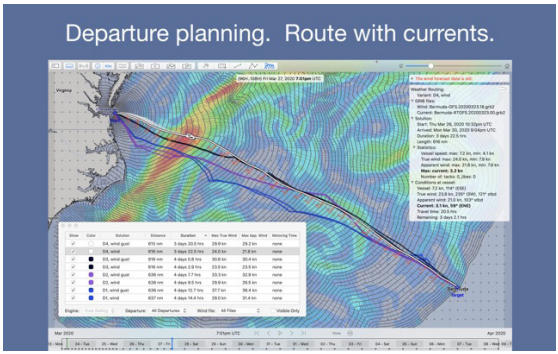

Figure 6. *Route Options [4]*

The weather route and the actual route along which the ship was proceeding, are shown in Figure 6. These routes are very close to each other, almost coincide, for the first 2.5 days. The weather route in this case suggested that it is better to continue proceeding to the east.

It should be noted that the path to the target point and the dynamic path are the same for the first 24-28 hours. This is an ideal situation since before you have to make the decision (either turn and proceed to north of the route or continue proceeding to the south according to the weather route) you will download the latest weather data and be able to analyze the situation again based on the position where your ship really is.

Thus, when choosing intermediate, tactical, target points that will be monitored by the weather router, there is no need to limit yourself to considering only those weather data that you download and analyze.

For example, if a ship is navigating the passage that is against constant winds such as trade winds, you must use this knowledge to place your target point so that it can be possible to take advantage of those winds.

If there is a fairly constant wind in the area you will be passing through, you can explore the area before the departure, and plot a lot of routes through it. It should give you a good representation of how the initial part of your route should join the subsequent part. Of course, you will reevaluate your initial assumptions as you get closer to the point of making decision.

Conclusions

The base of the weather routing system is an advanced isochronous solver which is accurate and very efficient. You can provide the solver with many configuration settings, such as setting sailing upwind angle limits, rolling, etc.

The solver is easy to use, often quickly providing informative results in situations where other solvers encounter difficulties or fail.

It should be noted that this weather routing system is available in LuckGrib on macOS, iOS and iPadOS platforms. The basic solver, visualization and set of configuration options are the same on all these platforms. Each of these platforms can generate the same weather routes. However, the interface used to interact with the system varies depending on the platform.

References

1. *Walther L., Rizvanolli A., Wendebourg M., Jahn C. Modeling and Optimization Algorithms in Ship Weather Routing. International Journal of e-Navigation and Maritime Economy. 2016; 4:31-45. (In Eng.) DOI: https://doi.org/10.1016/j.enavi.2016.06.004.*
2. *What is Weather. Routing? https://routing.luckgrib.com/intro/index.html. LuckGrib для ПК и Mac. https://apps.apple.com/ru/app/luckgrib/id1318450117.*
3. *LuckGrib. https://pcmacstore.com/en/app/992336031/luckgrib.*
4. *LuckGrib weather routing - iOS getting started. https://www.youtube.com/watch?v=PGCkemwWj_U.*

DOI 10.34660/INF.2023.56.36.064

METHOD FOR ASSESSING STABILITY OF SLOPES AND HIGH PIT LEDGES

Normatov Shovkat
Department Assistant
Namangan Engineering Construction Institute

Khusanov Bakhtiyar
Doctor of Physico-mathematical Sciences, head of laboratory
Institute of Mechanics and Seismic Stability of Structures named after M.T. Urazbaev

Abstract. *The paper proposes a method for determining the most probable sliding surfaces and the stability factors of heterogeneous soil slopes. Numerical calculations were used to construct diagrams of shearing and holding forces along the proposed sliding surface.*

Keywords: *stability, stability factor, slopes and ledges, deep quarry edge, stress state, ultimate stress state, sliding surface.*

Introduction. The problem of ensuring the stability and reliable operation of soil massifs and rocks with slopes and ledges arises in the design of many structures for hydraulic, industrial, civil, transport and other purposes. Soil massifs and rocks are earth dams, dams, embankments, sides of deep pits, foundations and natural slopes when they or the adjacent territory are used for economic activity. When designing and building on slopes or when placing buildings and mechanisms (vehicles and structures) on slopes, slopes or sides of quarries, one should also begin with an assessment of the degree of stability of the inclined surface. In order to increase the efficiency, completeness of exploitation and development of deposits, improve technical and economic indicators with safe operation, it is necessary to reliably ensure the stability of rock slopes. At the same time, the main task is to determine the optimal parameters of slopes and ledges, taking into account their long-term stability with a minimum amount of work and various loads. Overestimated slope angles lead to the development of destructive (landslide) phenomena; on the other hand, low slope angles cause a sharp increase in the volume of work and material resources, as well as incomplete development of mineral deposits [1-2]. To justify the slope stability parameters, a detailed study

of all factors influencing the process of soil shear on slopes and ledges is required. In this case, the choice of the method for calculating the stability of slopes and ledges of quarry walls is of decisive importance [1]. One of the main issues related to assessing the degree of stability of mountain slopes, as well as determining the size of possible collapse prisms, is the construction of the most probable fracture surface.

Recently, with the intensive development of computer technology, significant changes have occurred in the methodology for calculating the stability of soil slopes and made the creation of software for calculating the stability of slopes economically feasible and justified, which in turn led to widespread use in engineering practice. It became possible to perform calculations for slopes with complex geometry, take into account additional loads that change over time, structural strengthening elements of slopes, seismic and groundwater effects, etc. in the calculations. Visual control of the data, as well as graphical display of the results, made it possible to understand much more about the process than just calculating the stability coefficient. Now on the market there are a number of software products for calculating the stability of slopes, among them the most famous are: the Geo-Slope and SoilVision programs, the GEO5 program of the Fine company, the GeoStab program of the software package for geotechnical calculations of the "InzhProekStroy" LLC company, the "OTKOS" (slope) program of the KREDO-DIALOGUE, the program "OTKOS". Version 1.5 of the SCAD-Soft software package, the software OAS of the Polotsk University, the software package for analyzing the stability of the slope of the JSC NII VODGEO SSC RF and others. In almost all of the above programs, the iteration method is used to find the center of a round-cylindrical sliding surface, i.e. the most critical sliding surface is sought. Obviously, the soil mass, as well as their collapse compartments, is considered to be an absolutely rigid body. Consequently, these methods cannot take into account the deformed state of the soil mass arising from static and dynamic loads. In addition, using existing methods, finding the most dangerous round-cylindrical sliding surface using a selected area does not guarantee finding the minimum value of the stability coefficient, since several local minima may exist in other areas [3].

Methodology. It is generally accepted that the value of the stability factor K of the slope is defined as the ratio of the sums of the holding and shear factors acting along the most probable failure surface, which, by virtue of the name, should be determined in such a way that the value of K has a minimum value. In the general case, the value of K is defined as the ratio of two curvilinear integrals along the fracture (slip) line. Along the entire sliding surface, the soil destruction criterion is adopted in the form of the Mohr-Coulomb law. At the limit-stressed state of the soil massif, the formula representing the stability coefficient has the form:

$$K = \frac{\Phi_{удер}}{\Phi_{сдв}}$$

where $\Phi_{удер}$,$\Phi_{сдв}$ - holding and shearing factors acting along the most probable fracture surface. These factors can be forces acting along a possible sliding surface or, in the case of a round cylindrical sliding surface, according to the Terzaghi method, the forces of moments relative to the central axis of the cylinder [2]. In engineering calculations, various, very limited classes of possible slip lines are used (straight line, circular arcs or logarithmic spirals). However, it is obvious that for homogeneous slopes one can choose sliding surfaces in the form of an arc of circles, i.e. circular sliding surface.

In the general case, the value of the stability coefficient is defined as the ratio of two curvilinear integrals along the slip (destruction) line and has the form:

$$K = \frac{\int_s [f\sigma_N + c]ds}{\int_s \tau_N ds} \quad (1)$$

where s - the area of the most probable sliding surface. In the case of considering a two-dimensional formulation, the slip surface is replaced by the slip line, and the area, respectively, by the length along the surface line. If s is an arc coordinate, i.e. the shape and position of the slip line are known, then the curvilinear integrals can be replaced by definite integrals, and the value of the stability coefficient is calculated as the ratio of the sum of the holding and shearing factors (forces). In the usual approach, the area (compartment) of the collapse under consideration is divided into vertical fragments (columns) by drawing vertical lines, and the integral for calculating the stability coefficient is replaced by the corresponding sums (the accuracy of the result is affected by the split width of these fragments). Through the weight of each fragment, the normal σ_N and tangential τ_N stresses acting on the sole of this fragment at the moment of limiting equilibrium are determined.

In [4-6], a method was developed for assessing the stability of homogeneous soil slopes, combining two calculation approaches: the assumed sliding surface is considered to be round-cylindrical surfaces, and in calculation (1), the stress state is supposed to be determined from the solution of a two-dimensional problem of continuum mechanics. The proposed method or method for assessing the stability of soil slopes is also based on this assumption. The normal and shear stress acting on the site forming an angle with the horizon (with the x-axis) is calculated by the formula

$$\sigma_N = \sigma_{xx}\sin^2\alpha + \sigma_{yy}\cos^2\alpha - 2\tau_{xy}\sin\alpha\cos\alpha,$$
$$\tau_N = \tau_{xy}(\cos^2\alpha - \sin^2\alpha) - (\sigma_{xx} - \sigma_{yy})\cdot\sin\alpha\cos\alpha, \quad (2)$$

where σ_{xx}, σ_{yy} and τ_{xy} -stress values obtained by solving a two-dimensional problem. In the case of considering a dynamic non-stationary problem, the highest value that occurs during the considered time is taken as the stress values. Thus, using normal and shear stresses along the sliding surface line, it is possible to determine the stability factor. However, the whole difficulty lies in determining the intended sliding surface, which gives the minimum value of the stability coefficient. Therefore, the problem of stability estimation is a statically indeterminate problem.

To find an arbitrary (unknown) sliding surface, we proceed as follows. The local (local) stability coefficient (for a limited slope area or for a small particle), taking into account (2), has the form

$$k = \frac{f(\sigma_{xx}\sin^2\alpha + \sigma_{yy}\cos^2\alpha - 2\tau_{xy}\sin\alpha\cos\alpha) + c}{\tau_{xy}(\cos^2\alpha - \sin^2\alpha) - (\sigma_{xx} - \sigma_{yy})\sin\alpha\cos\alpha} \quad (3)$$

where угол α - is the angle between the tangent of the considered small area (curve) with the horizon (x-axis). The local stability coefficients (3), in addition to the mechanical characteristics, also depend on this angle of inclination of the most probable slip area (curve) at the considered point in the slope zone. Equation (3) can be written as:

$$k = \frac{f\left(\frac{\sigma_{xx}+\sigma_{yy}}{2} - \frac{\sigma_{xx}-\sigma_{yy}}{2}cos2\alpha - \tau_{xy}sin2\alpha\right) + c}{\tau_{xy}cos2\alpha - \frac{\sigma_{xx}-\sigma_{yy}}{2}sin2\alpha} \quad (4)$$

Investigating the ratio for the coefficient of stability to the extremum, we determine the value of the angle at which the condition $k=k_{min}$ is satisfied. To give the minimum value of the stability coefficient $k=k_{min}$ for the point under consideration for different angles of the probable shear surface, we equate $k'_\alpha = 0$, and determine the angle of inclination of the proposed slip surface (line) at this point. Carrying out simple calculations, we find the angle α between the O*x* axis and the platform (line), along which the stability coefficient at the point under consideration has a minimum value:

$$sin2\alpha = \frac{BC \pm A\sqrt{A^2+B^2-C^2}}{A^2+B^2} \quad (5)$$

where $A = \frac{\sigma_{xx}^2 - \sigma_{yy}^2}{2}$, $B = (\sigma_{xx} + \sigma_{yy})\tau_{xy}$, $C = \frac{(\sigma_{xx}+\sigma_{yy})^2}{2} + 2\tau_{xy}^2$

It can be seen from relation (5) that at any point of the slope zone there are two slip areas (lines) with the same minimum value of the stability coefficient.

As noted above, this method for assessing the stability of soil slopes (deep pit sides) consists in finding the most probable (dangerous) sliding surface using design stresses, at which the stability coefficient has a minimum value. To build the most probable expected sliding surface, the following procedures should be performed sequentially.

1) A plane problem is solved and the values of the stress state of all points of the slope area of the soil massif with all acting loads are determined (in the case of considering a non-stationary problem, the maximum stress values are determined during the considered moment of time or the dynamic coefficient should be found for using the engineering method);

2) Using the calculations of the local stability coefficient (4), a point is determined in the vicinity of the slope transition to the base (leftmost point), or in the vicinity of the crest (rightmost point);

3) Through the found point, located near the contour of the slope, where the condition $k=k_{min}$ is fulfilled, a straight line segment is drawn, forming an angle α with the horizontal axis (Ox axis), determined by relation (5) with a positive sign for a point in the vicinity of the transition of the slope to the base , or with a minus sign for the ridge point near the slope. The length of the segments depends on the geometric dimensions of the soil slope (slope height), the shorter the length of the segment, the more accurate the probable sliding surface will be; Thus, a small segment of the supposed most probable sliding surface is determined. Further, for a point located at the other end of the found segment, the angle α is again determined and a new segment is drawn through the middle of this segment at this angle. This procedure continues until the last segment of the proposed sliding surface intersects another slope contour;

4) After determining the most probable sliding surface, the assessment of the stability of the whole soil slope is carried out according to the formula (1) using a numerical calculation.

Thus, we find the most probable slip surface (line). The position and shape of the most probable slip surface (line) depend on the geometric dimensions of the slope (on the height of the slope and the angle of occurrence), the physical and mechanical characteristics of the soil or rock (density, cohesion, angle of internal friction, etc.), as well as the stress states from acting loads.

Calculation results. According to the proposed method for assessing the stability of soil slopes, a program was compiled for finding the intended sliding surface and the stability coefficient. The figure shows the result for a uniform slope with ledges. An array with a height of 20 m and a general laying angle $\alpha = 45°$ with the following soil characteristics was taken as the initial data: density $\rho = 2000\,kg/m^3$; specific cohesion c = 30 kPa. The stability factor for this sliding surface was 1.7457. As can be seen from the figure, for a uniform slope,

the most expected sliding surface practically coincides with the round-cylindrical sliding surface.

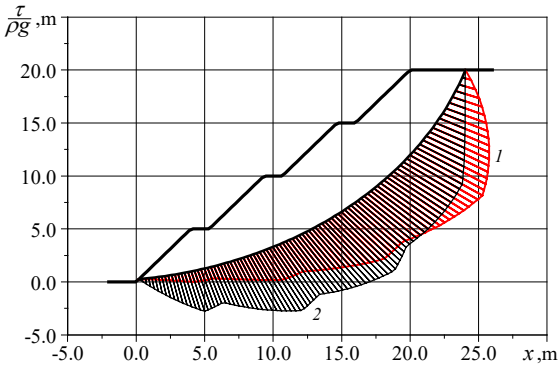

Figure *Estimated sliding surface and diagram of shear (1) and holding (2) stresses along the surface*

Conclusions. A method is proposed for assessing the stability of soil and mountain slopes, which combines two calculation approaches and takes into account the nonlinear properties of deformation. The essence of the method is to use the solution of a plane problem (stress-strain state) taking into account all factors: heterogeneity and geological features of the massif, acting static and dynamic loads and finding the most probable sliding surface by minimizing the values of local stability coefficients

References

1. *Polishchuk S.Z. et al. Forecast of stability and optimization of the parameters of deep quarry boards. Dnipropetrovsk: Polygraphist, 2001*
2. *Popov V.N., Shpakov P.S., Yunakov Yu.L. Managing the stability of open pit slopes. - Moscow: Gornaya kniga, 2008*
3. *Sultanov K.S., Khusanov B.E., Rikhsieva B.B. «Evaluation of the stability of slopes and ledges by the method of round-cylindrical sliding surfaces» in Proceedings of the International Scientific and Technical Conference «Prospects for the innovative development of the mining and metallurgical complex», 12-13, 2018.*
4. *Bakhtiyar K., Shovkat N., Ozodaxon K. On one method for assessing the soil slopes stability // AIP Conf. Proc., Vol.2637, 030012. https://doi.org/10.1063/5.0119155*

5. Sultanov K., Umarkhonov S., Normatov S. Calculation of earth dam strain under seismic impacts // AIP Conf. Proc., Vol.2637, 030008. https://doi.org/10.1063/5.0118430

6. Sultanov, K.S., Khusanov, B.E., Loginov, P.V., Normatov, Sh, Method for Assessing the Reliability of Earth Dams in Irrigation Systems // Construction of Unique Buildings and Structures, 2020; Volume 89 Article No 8901

DOI 10.34660/INF.2023.55.94.065

STUDY OF THE CAPABILITIES OF UNMANNED AERIAL VEHICLES IN SOLVING THE PROBLEMS OF GAS AND OIL LEAKS

Solovev Maxim Olegovich
Postgraduate
MIREA — RUSSIAN TECHNOLOGICAL UNIVERSITY

Abstract. *This article is devoted to the problem of studying the capabilities of unmanned aerial vehicles in solving the problems of gas and oil leaks. It explores the features of the use of unmanned aerial vehicles in monitoring the reliability of the operation of oil and gas transport equipment. In this study, a set of interchangeable payload modules (photo camera, television camera, infrared camera, thermal imager), ground control station and catapult are used as part of the Tachyon UAV complex. In order to study and solve the problem of counting gas and oil leaks using UAVs, a scheme for converting the dimensions of the detection object in TV channels in the form of an UAV unit with a matrix converter is proposed. Integral algorithmic development of the proposed computer application is presented.*

Keywords: *unmanned aerial vehicles, leaks, gas, oil, transport equipment, programming*

Introduction. Russia is one of the few countries in the world that has a powerful aircraft design and aircraft industry potential. The development of the aviation industry makes it possible to overcome the backlog in the construction of unmanned aerial vehicles (UAVs) and take a competitive place in their production and operation [1]. The scientific, technical and technological potential is relevant for state financing of the aircraft industry and is attractive for investment. One of the areas that allow the implementation of new ideas and professional experience in the form of final products is the creation of unmanned aerial vehicles (UAVs) [2].

The development of each of these components when creating a UAV requires a high development of aircraft construction, electronics, information and other technologies. Therefore, few countries in the world have a full cycle of such a unique production - from UAVs to its target equipment in ground control posts.

Simultaneously with the development, production and use of UAVs in the world, a regulatory and legal framework for the joint use of the joint space of UAVs and the space piloted by aircraft is being formed.

A very relevant and popular area of using UAVs is to take into account the problems of gas and oil leaks [3]. In the aspect of taking into account the problems of the reliability of the operation of oil and gas transport equipment, it is very important to implement the UAV technology in the program for counting the number of gas and oil leaks.

The purpose of this article is to study the possibilities of unmanned aerial vehicles in solving the problems of gas and oil leaks.

The discussion of the results. In the structure of the Russian market, the share of civilian UAVs accounts for more than 70% of the market, in which the main share is occupied by consumer drones - fig. 14].

Figure 1. *UAV application area in Russia*

Today, unmanned aircraft are intensively used in the civil sphere to perform the following functions [4-5]:

- protection of borders;
- maintenance of law and order;
- combating the consequences of natural disasters or man-made disasters;
- monitoring of the ecological state of the natural environment.

The problems of unmanned aerial vehicles concern not only UAVs, which are an integral part of the unmanned aerial complex (UAC), which includes:

- air vehicle (AV)
- modern special on-board equipment;
- ground control, launch and landing systems.

The unmanned aircraft complex is a complex aviation technical system, which includes [6]:

- one or more UAVs;
- command centre;
- means of communication;
- means of launch, rescue and maintenance;
- means of transportation.

Modern Raybird 3 UAVs can monitor targets over large areas with a radius of thousands of hectares / km and transmit video in a short time (for a short period of time, as well as broadcast video in real time). The use of unmanned aerial systems is very cheap. UAV like Raybird 3 can cover large places with a radius of thousands of hectares / km and link video in a short time - within a short period of time, and can show the picture live. Gyrostabilizing gimbals with built-in infrared thermal sensors are currently widely used at night [7]. Modern UAVs for diagnosing the reliable operation of oil and gas transportation equipment can easily meet the requirements for monitoring gas and oil leaks in such basic applications:

- assessment of territories and perimeter;
- automated identification of types of leaks;
- monitoring the progress of gas and oil leaks;
- assessment of the size of gas and oil leaks;
- environmental management.

Focusing on the processes of development and implementation of UAV technology in the direction of monitoring the reliability of the operation of oil and gas transport equipment, we highlight the main promising aspects of its use in comparison with other technological methods: the possibility of flying over a large area, its inaccessibility, its closeness in certain periods of time, its closeness in terms of logistics capabilities for ground facilities [8].

In this paper, the features of the use of the small UAV “Takhion” in solving the problems of the reliability of the operation of oil and gas transport equipment are investigated - fig. 2 [9].

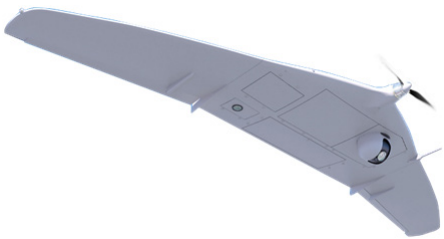

Figure 2. *Appearance of the “Tachyon” UAV*

A scheme is proposed for converting the dimensions of an object for detecting gas and oil leaks in TV channels in the form of an UAV unit with a matrix converter, which is shown in Fig. 3 [10].

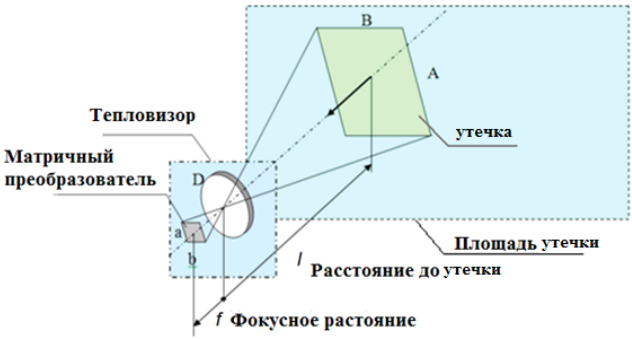

Figure 3. *Scheme for obtaining a video image of gas and oil leaks in a TV with a matrix converter, as an element of the "Tachyon" UAV*

Further, from the point of view of developing a computer application for the Tachyon UAV for monitoring the reliability of the operation of oil and gas transport equipment, it is necessary to combine the following software algorithms, such as MASK R-CNN, Slic superpixels, Treshlding histograms and OpenCV + FFmpeg.

Conclusion. This article is devoted to the problem of studying the capabilities of unmanned aerial vehicles in solving the problems of gas and oil leaks. It explores the features of the use of unmanned aerial vehicles in monitoring the reliability of the operation of oil and gas transport equipment. As part of the study, a set of interchangeable payload modules (a camera, a television camera, an infrared camera, a thermal imager), a ground control station and a catapult are used as part of the Tachyon UAV complex. An integrated algorithmic development of a proposed computer application for the Tachyon UAV for monitoring gas and oil leaks in real time using the MASK R-CNN, Slic superpixels, Treshlding histograms and OpenCV + FFmpeg software algorithms is presented.

References

1. Airoyan Z.A., Korkishko O.A., Sukharev G.V. Monitoring of oil trunk pipelines using unmanned aerial vehicles // Engineering Bulletin of the Don, No. 4. 2016. P.1-8.

2. Anikaeva A.D., Martyushev D.A. Assessment of the potential for the use of unmanned aerial vehicles in the oil and gas industry // Subsurface use. 2020. №4. pp.344-355.

3. Zhuzhgov Yu.V., Kalach E.V. Brief description of UAVs used for aerial monitoring of oil and gas facilities // Fire safety: problems and prospects. 2018. P. 1025-1028.

4. Fedoseeva N.A., Zagvozkin M.V. Perspective areas of application of unmanned aerial vehicles // Scientific journal. 2017. No. 9 (22). URL: https://cyberleninka.ru/article/n/perspektivnye-oblasti-primeneniya-bespilotnyh-letatelnyh-apparatov (Date of access: 06.01.2023).

5. Chashchina E.V. Review of the study of unmanned aerial vehicles for environmental monitoring // Ecological safety in the technosphere space: a collection of materials from the Third International Scientific and Practical Conference of Teachers, Young Scientists and Students. 2018. P.197-200.

6. Chistyakov D.A., Nechaeva O.A. Environmental monitoring of oil and oil product spills using aircraft // New Science: Problems and Prospects. 2016. P.18-22.

7. Sharafutdinov A.A., Imamutdinov S.A., Mukhametyanova A.N., Tabuldina A.T., Mannanov T.A. The use of unmanned aerial vehicles for remote monitoring of the environment // Network publication "Oil and Gas Business". 2018. №2. pp. 99-116.

8. Shikhmagomedova S.M. The use of unmanned aerial vehicles in the oil and gas industry // ICRM. 2017. No. 6-2 (60). pp. 48-50.

9. Drones count wildlife more accurately and precisely than humans / J. C. Hodgson, R. Mott, S. M. Baylis [et al.] // Methods in Ecology and Evolution. 2018. P. 1-8.

10. Liu H., Jiang G. S., Li H. A comparative study on four survey methods used in ungulate population size estimation in winter in north China // Shengtai xuebao. 2015. № 9. C. 3076-3086.

DOI 10.34660/INF.2023.53.71.066

INVESTIGATION OF VARIOUS TYPES OF DESIGNS OF THE SENSING ELEMENT OF A MEMS ACCELEROMETER

Mordvinov Dmitrii Bogdanovich
Master's degree Student
Peter the Great St.Petersburg Polytechnic University

Akhmetov Denis Bulatovich
Candudate of Technical Sciences, Associate Professor
Peter the Great St.Petersburg Polytechnic University

Abstract. *With the growth in the production of equipment for monitoring physical quantities, the need for microelectromechanical systems (MEMS) is also growing.*

Due to the strong demand for these devices, there is a need for more research and development of new materials, improved geometry and the use of new physical principles to meet the needs of consumers.

Currently, micromechanical accelerometers (MMA) of capacitive type are gaining particular popularity, as they are characterized by high sensitivity and accuracy of measurements of physical quantities.

In this paper, approaches to the construction of sensors for one-, two- and three-axis systems are considered. The results for various types of elastic suspension are presented. The designs of perforated inertial masses are considered. The main advantages of these systems are revealed.

Keywords: *micromechanical capacitive accelerometers, natural oscillation frequency, elastic suspension, inertial mass, microelectromechanical systems.*

I Introduction

Currently, there are various types of designs of the sensitive element (SE) of capacitive MMA [1–3]. The main parameters in the production of any device are low cost and ease of manufacture, the availability of technology and the possibility of using it in various fields of science and technology. MEMS products more than meet these requirements, as well as these devices are reliable and have the ability to reach sizes of several micrometers [4].

Industrial devices are often systems with large dimensions, which, in addition to the sensor itself with approximate dimensions of 2x2 cm, also include signal processing boards, fittings and other devices, due to which the weight increases to 150 g, which does not allow using this solution in products that are critical to weight and size indicators. Currently, there are many approaches to the production technologies of capacitive-type SE MMA, ranging from various types of elastic suspension (ES) to the features of the technological process [5].

One of the widely used materials in the manufacture of SE is single-crystal silicon due to its low hysteresis, resistance to overloads and the ability to package it in signal processing boards. Single-crystal silicon has been especially widely used in areas where microminiaturization is important. However, one of the significant drawbacks is the low sensitivity [6,7].

During the operation of the sensors, the readings of the device will be affected by destabilizing factors such as temperature, vibration, humidity, and others. In this regard, it is necessary to pay attention to these phenomena already at the design stage of the device. Especially when operating in extreme conditions, whether it be a wide range or temperature difference, from -55 ° C to 300 ° C, mechanical and hydraulic shocks and other conditions. It is necessary that the device has a mechanical strength higher than the entire system as a whole, since the sensor must have a greater margin of safety than the design as a whole [7,8].

II. Investigation of various types of elastic suspension of the sensitive element

The physical and geometric parameters of the SE directly affect its stiffness, sensitivity and resonant frequencies.

When designing the SE MMA, it should be taken into account that the stiffness factor has a greater effect on the sensitivity and natural oscillation frequency. The frequency characteristics of the MMA also depend on the geometric parameters of the ES. The first mode for a single-axis MEMS accelerometer is working, while others will have a parasitic effect on the device [6,8]. For the stability of the operating parameters, it is necessary that the first mode is further away from the subsequent ones so that the first resonant frequency is not affected by the others.

There are many types of ES: folded springs, torsion bars, comb drives and others.

Springs are mainly used in single-axis sensors, due to the folding structure, thickness and length, it is easy to provide the necessary rigidity, achieve the desired sensitivity for one axis. It is also worth noting that this design provides large movements for the main axis. One of the main types of ES in the form of a folded spring are: folded beams with rectangular and round sections, and straight beams [9]. The considered suspensions are shown in Figure 1.

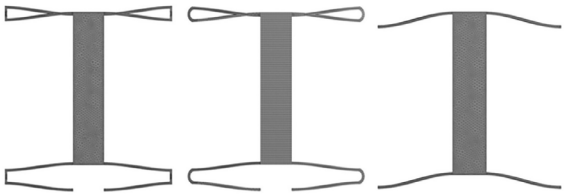

Figure 1. *The design of the elastic suspension: a) folded beams with a rectangular section; b) folded springs with a circular cross section; c) straight beams*

The thickness of the ES, its type, and the orientation of the crystallographic silicon surface significantly affect the design parameters.

The ES of the «straight beams» type has the maximum difference between the first modes and subsequent ones at a width of 120 μm and the orientation of the silicon surface (111) in comparison with other designs. Reducing the width and changing the orientation of silicon from (111) to (100) for any type of construction leads to a decrease in the difference between the first and second modes [1, 9].

The crystallographic orientation of silicon directly affects its residual stresses as the temperature changes. Thus, when silicon is (111) oriented, suspensions have maximum stresses in the model with straight beams, and minimum stresses in a suspension with a rectangular cross section [5]. It should be noted that residual voltages directly affect the sensitivity of the device and its reliability, the lower the voltage, the greater the stability and sensitivity.

The study of impact resistance is one of the defining areas of application of MMA. Mechanical shock can cause various kinds of damage to the MEMS - accelerometer, ranging from cracks to chips and complete incapacity of the device. The impact resistance depends on the width of the UE, a large width entails an increased impact resistance, however, the mass of the SE increases and the sensitivity decreases. It is worth noting that stiffness and mass also affect sensitivity. Sensitivity formula for SE MMA:

$$S = \frac{a}{x} = \frac{k}{m}, \tag{3}$$

where S – accelerometer sensitivity,

a - the SE acceleration,

x - movements of SE,

k is the stiffness coefficient of the elastic suspension,

With an increase in the length of the «folded spring» ES, the displacement along the main axis also increases, while the sensitivity along the cross axes de-

creases. This is due to the fact that the displacements along the main axis differ by more than two times, relative to the transverse ones [8].

Thus, the model with straight beams has the highest values for mode ratios, which can make it possible to use this type of ES for high-precision measurements, while being the least affected by impact, for example, in life support control systems. The rectangular profile pleated spring model has shown the best performance in impact resistance, which can be concluded that the operation of this model is suitable for harsh conditions, for example, in deep hole drilling machines [7,9].

The orientation of silicon also affects the results, for example, with the orientation of silicon (111), the ES, regardless of the width, has large values of resonant frequencies and their ratios, therefore, for accurate measurements, it is necessary to choose the orientation (111) [3].

One of the methods for implementing multiaxial MMA is a torsion suspension [4,8]. MEMS is also an accelerometer, also designed to measure linear accelerations along an axis perpendicular to the plane of the substrate, and its modal analysis was carried out. The material used in the calculation is single-crystal silicon.

Torsion springs are able to go beyond the substrate due to torsional deformations, which has an advantage over folded springs. However, torsion bars often require a large aspect ratio of 1:50 9]. Figure 2 shows a torsion suspension.

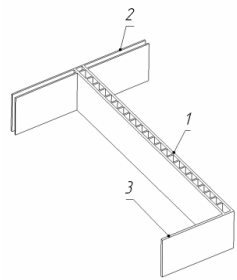

Figure 2. *The design of the torsion suspension*

This ES consists of a pair of vertical torsion beams 2 and 3 and a lightweight rigid beam 1. Beam 2 consists of two parallel plates, which protects this structure from bending deformations while isolating torsion deformations. The design of the considered SE is shown in Figure 3.

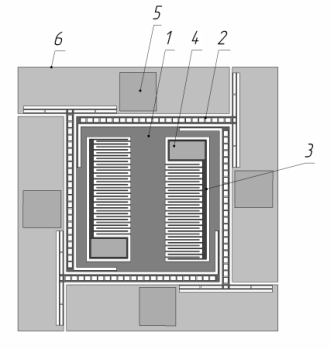

Figure 3. *The design of the SE with torsion bars*

Figure 3 shows IM 1. Metal pads 5 for anchor elements on the substrate. There are also platforms 4 on which capacitive elements 3 are installed, in turn they are used to measure capacitance, which in turn is necessary to determine linear acceleration. The torsion bars themselves 2.

It should be noted that this design has a large area compared to a folded spring and a large mass, since the width of the torsion bars is 100 microns and their mounting design goes beyond the ES and requires additional stationary mass. This design operates on small ranges from 1g to 10g, the first oscillation mode is equal to 8845 Hz, which is more than the designs of uniaxial sensors with the folded spring type ES at 100 Hz. The next two modes are equal to 10459 and 10465 Hz, respectively, their ratios are also equal, however, when considering multiaxial accelerometers, it is worth striving to equalize the values of the first three modes [9].

The development of MMA with torsion bars is a promising area, but it needs to be improved. Increased mass, area and large frequency discrepancy is a disadvantage for SE with torsion bars. In the future, these devices can be used as three-axis accelerometers and used in navigation systems.

For a two-axis accelerometer, comb drives, the so-called «P-beams» [9], are used. The advantage of comb drives for use in two-axis systems is that in addition to the longitudinal compression deformation, due to the design of the drive, there is also a transverse one, which allows the SE to move along two axes X and Y. Figure 4 shows the SE with ES in the form comb drives.

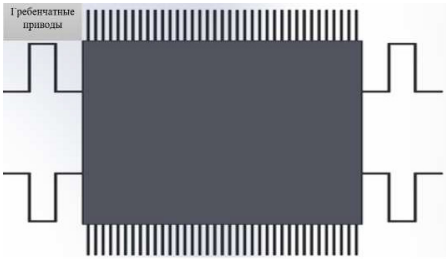

Figure 4. *Movable inertial mass with suspensions*

This SE has the necessary sensitivity along two axes. This development can be applied in many areas. Some of the most popular in capacitive biaxial probing are the automotive and household industries [43].

III. Analysis of Structures with Perforated Masses

To resolve issues with the mass of the structure, perforated IMs are used. Perforation can be performed both as partially removed parts of the moving mass (PM), and in the form of a full-fledged electrode structure (ES), the so-called «sandwich structure» [24,44-46]. Figure 5 shows the design of the SE with a perforated central mass (CM).

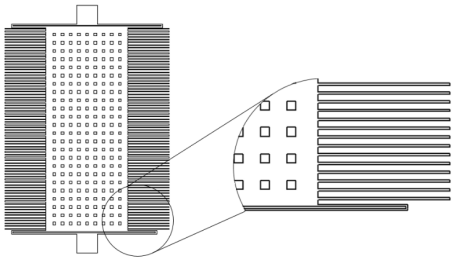

Figure 5. *Sensing element with perforated mass*

It should be borne in mind that in this case, with a decrease in IM, the sensitivity of the sensor and its resonant frequency also change. It must be understood that when designing a SE, everything boils down to the fact that the system had the necessary rigidity, high sensitivity, and load resistance. So the resonant frequency is found by the formula:

$$f_0 = \frac{1}{2\pi}\sqrt{\frac{m}{k}}, \tag{2}$$

where f_0 – natural oscillation frequency,
m is the SE mass.

It can be seen from equations (1) and (2) that these are reciprocal values, therefore mass perforation can be used in the design if it does not significantly affect the sensitivity for the sake of a smaller mass of the structure.

The “sandwich construction” of MMA is shown in Figure 6.

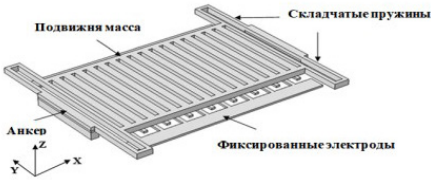

Рисунок 6. *Сэндвич – конструкция ЧЭ*

The IM of this SE consists of movable electrodes. Under the influence of acceleration, there is a change in capacitance between mobile and fixed ES. This design is especially popular in uniaxial MMAs [10]. It is also noted that the sensitivity along the Y axes is about 1% and Z is about 7%, and these characteristics directly depend on the thickness of the ES [45]. Figure 16 shows the dependence of MMA sensitivity on the thickness of the springs.

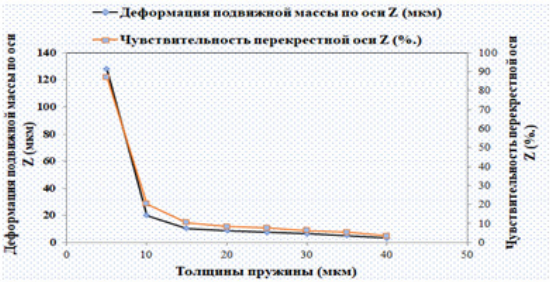

Figure 7. *Dependence of deformations and sensitivity on the thickness of the ES along the Z axis*

From this figure it can be seen that with an increase in the thickness of the springs, the deformation and sensitivity along the parasitic Z axis decrease.

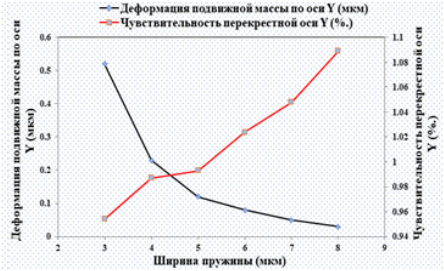

Figure 8. *Dependence of deformations and sensitivity on the thickness of the ES along the Y axis*

With the Y-axis, the situation is different. So with an increase in the width, the deformation decreases, but the sensitivity increases, but it is worth noting that for the Y axis, the sensitivity is not critical.

At the same time, it should also be taken into account that with an increase in the width of the ES, the mass of the SE as a whole also increases. In the considered design of the SE MMA, it is necessary to look for the best variant of the ES, since this MEMS will mainly depend on the parameters of the ES.

Particularly popular is the "sandwich construction", where the moving mass is fixed between two stationary ES, and the elastic suspension has two fixing points instead of one [10]. Figure 9 shows a diagram of this SE.

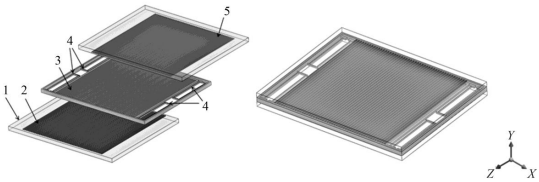

Figure 9. *SE «sandwich - structures»: 1 - substrate of single-crystal silicon; 2 and 5 - stationary ES are shown; 3 - IM; 4 - UP*

For this design, it is advisable to use silicon with (111) orientation, since in this case the displacements along the main X axis exceed Y by 50 times, and the Z axis by 10 times, which will significantly affect the sensitivity. Modal analysis shows that the first resonant frequency differs from the subsequent ones by almost 3 times, which proves that the sensitivity is maximum along the main X axis [45].

In order to lighten the mass, perforated MIs can be used [10]. However, these elements need to be improved. At the same time, the cost of this design increases along with the complexity of the technological process.

IV. Conclusion

In this work, the designs of various ESs were considered. It was found that in the case of single-axis sensors, it is advisable to use UEs of the type of folded springs or straight beams, however, it is necessary to take into account the individual features of each of the structures and find compromise solutions regarding the width, orientation of the lattice and its type.

For two-axis systems, the use of ES of the "comb drives" type is one of the best options, since the deformations for the X and Y axes are less than two times, which indicates that the sensor has the necessary sensitivity for these axes.

One of the promising elastic suspensions for a three-axis sensor is a torsion suspension. Although this design requires improvements, however, for the sake of its simplicity and efficiency, it has further prospects.

Considered possible designs of perforation IM. The designs show good sensitivity, which is provided by the inertial mass suspension elements used, in particular by reducing the width of the pleated springs. However, it should be taken into account that the complexity in manufacturing these SEs increases with the number of holes or electrodes in the IM.

References

1. I. E. Lysenko, D. Y. Sevostyanov and O. A. Ezhova, «Development of a behavioural model of the MEMS accelerometer» in 2020 The 16th International Conference on Electronic Devices and Control Systems, 2021, pp. 1-6, doi; 10.1088/1742-6596/1862/1/012010.

2. I. E. Lysenko, D. Y. Sevostyanov and O. A. Ezhova, «Design and simulation high aspect ratio torsion suspension of MEMS z-axis accelerometer» in 2020 Book of Abstracts of 7th International School and Conference «Saint Petersburg OPEN 2020» on Optoelectronics, Photonics, Engineering and Nanostructures, 2020, pp. 478-479, doi: 10.1088/1742-6596/1695/1/012177.

3. Aung Ye Ko Ko, Simonov B.M. and Timoshenkov S.P. Modeling and research of various types of inertial mass suspensions in sensitive elements of micromechanical devices. Bulletins HEI. Electronics. – 2020. – No. 5 – P. 440-451.

4. Y. Parmar1 and N. Gupta, "Characterization of SOI technology-based MEMS differential capacitive accelerometer and its estimation of resolution by near vertical tilt angle measurements Microsystem Technologies," in IEEE Microsystem Technologies, vol. 26, no. 5, pp. 701 – 706, 2020, doi: 10.1007/s00542-020-04561-6.

5. Adamov A.P., Adamova A.A., Temirov A.T. Methods of system design and technological design of electronic products, taking into account the requirements

of the concept «Industry 4.0» // Proceedings of the international symposium «Reliability and quality» / 2020. V. 2. P. 310-317.

6. A. Thura. 24th All-Russian Interuniversity Scientific and Technical. conf. students and graduate students «Microelectronics and Informatics» - 2017: the influence of thermoelastic damping on the parameters of resonators of frequency microaccelerometers // Bulletins of Higher Educational Institutions. Electronics. – 2017. – No. 3. – P. 105.

7. Vlasov A.I., Mileshin S.A., Tsivinskaya T.A. Analysis of defects in single-crystal silicon sensor crystals and production technologies // Nanoindustry. – 2018, – No. 5 – P. 238-245.

8. Jie Zhang, Yunbo Shi and Huiliang Cao "Design and Implementation of a Novel Membrane-Island Structured MEMS Accelerometer with an Ultra-High Range" in IEEE «Sensors» Journal, vol. 22, no. 21, pp. 20246 - 20256, 2022, doi: 10.1109/JSEN.2022.3195340

9. Naumenko D.V., Lysenko I.E. and Sinyutin S.A., MEMS – Sensors Based on High-Aspect Torsion Suspensions for Process Control. Ser. 1. – 2020. – No. 1. pp. 143-146.

10. Aung Ye Ko Ko, Simonov B.M. Simulation of the sensing element of a sandwich structure of a capacitive micromechanical accelerometer taking into account changes in the dielectric constant. Electronics. – 2020. – No. 2. – P. 40-48.

Proceedings of International Science Conference

SCIENCE. EDUCATION. PRACTICE

Delhi, India

April 8, 2023

Signed in print 08.04.2023 г. 60x84/16.
Ed. No. 1. Circulation of 500 copies. India, 2023.
Infinity publishing, 2023